Mon. Not. R. Astron. Soc. **000**, 1 (2008) Printed 18 May 2009 (MN LaTeX style file v2.2)

Cosmological Radiative Transfer Comparison Project II: The Radiation-Hydrodynamic Tests

Ilian T. Iliev[1,2,3⋆], Daniel Whalen[4], Garrelt Mellema[5], Kyungjin Ahn[6,7], Sunghye Baek[8], Nickolay Y. Gnedin[9], Andrey V. Kravtsov[10], Michael Norman[11], Milan Raicevic[12], Daniel R. Reynolds[13], Daisuke Sato[14], Paul R. Shapiro[6], Benoit Semelin[7], Joseph Smidt[15], Hajime Susa[16], Tom Theuns[12,17], Masayuki Umemura[14]

[1] *Astronomy Centre, Department of Physics & Astronomy, Pevensey II Building, University of Sussex, Falmer, Brighton BN1 9QH, United Kingdom*
[2] *Universität Zürich, Institut für Theoretische Physik, Winterthurerstrasse 190, CH-8057 Zürich, Switzerland*
[3] *Canadian Institute for Theoretical Astrophysics, University of Toronto, 60 St. George Street, Toronto, ON M5S 3H8, Canada*
[4] *T-2 Nuclear and Particle Physics, Astrophysics, and Cosmology, Los Alamos National Laboratory, Los Alamos, NM 87545, U.S.A.*
[5] *Dept. of Astronomy and Oskar Klein Centre, AlbaNova, Stockholm University, SE-10691 Stockholm, Sweden*
[6] *Department of Earth Science Education, Chosun University, Gwangju 501-759, Korea*
[7] *Department of Astronomy, University of Texas, Austin, TX 78712-1083, U.S.A.*
[8] *LERMA, Observatoire de Paris, 77 av Denfert Rochereau, 75014 Paris, France*
[9] *Fermilab, MS209, P.O. 500, Batavia, IL 60510, U.S.A.*
[10] *Dept. of Astronomy and Astrophysics, Center for Cosmological Physics, The University of Chicago, Chicago, IL 60637, U.S.A.*
[11] *Center for Astrophysics and Space Sciences, University of California, San Diego, 9500 Gilman Drive, La Jolla, CA 92093-0424, U.S.A.*
[12] *Institute for Computational Cosmology, Durham University, Durham, United Kingdom*
[13] *Department of Mathematics, 208 Clements Hall, Southern Methodist University, Dallas, TX 75275, USA*
[14] *Center for Computational Sciences, University of Tsukuba, Tsukuba, Ibaraki 305-8577, Japan*
[15] *Department of Physics and Astronomy, 4129 Frederick Reines Hall, UC Irvine, Irvine, CA 84602, U.S.A.*
[16] *Department of Physics, Konan University, Kobe, Japan*
[17] *Department of Physics, University of Antwerp, Campus Groenenborger, Groenenborgerlaan B-171, B2020 Antwerp, Belgium*

arXiv:0905.2920v1 [astro-ph.CO] 18 May 2009

18 May 2009

ABSTRACT

The development of radiation hydrodynamical methods that are able to follow gas dynamics and radiative transfer self-consistently is key to the solution of many problems in numerical astrophysics. Such fluid flows are highly complex, rarely allowing even for approximate analytical solutions against which numerical codes can be tested. An alternative validation procedure is to compare different methods against each other on common problems, in order to assess the robustness of the results and establish a range of validity for the methods. Previously, we presented such a comparison for a set of pure radiative transfer tests (i.e. for fixed, non-evolving density fields). This is the second paper of the Cosmological Radiative Transfer (RT) Comparison Project, in which we compare 9 independent RT codes directly coupled to gasdynamics on 3 relatively simple astrophysical hydrodynamics problems: (5) the expansion of an H II region in a uniform medium; (6) an ionization front (I-front) in a $1/r^2$ density profile with a flat core, and (7), the photoevaporation of a uniform dense clump. Results show a broad agreement between the different methods and no big failures, indicating that the participating codes have reached a certain level of maturity and reliability. However, many details still do differ, and virtually every code has showed some shortcomings and has disagreed, in one respect or another, with the majority of the results. This underscores the fact that no method is universal and all require careful testing of the particular features which are most relevant to the specific problem at hand.

Key words: H II regions—galaxies:high-redshift—intergalactic medium—cosmology: theory—radiative transfer— methods: numerical

1 INTRODUCTION

The transfer of ionizing radiation through optically-thick media is a key process in many astrophysical phenomena. Some examples in-

⋆ e-mail: I.T.Iliev@sussex.ac.uk

clude cosmological reionization (*e.g.* Gnedin 2000; Nakamoto et al. 2001; Razoumov et al. 2002; Sokasian et al. 2003; Ciardi et al. 2003; Iliev et al. 2006b; Kohler et al. 2007), star formation (*e.g.* Hosokawa & Inutsuka 2005; Iliev et al. 2006a; Razoumov et al. 2006; Susa & Umemura 2006; Ahn & Shapiro 2007; Whalen & Norman 2008b), radiative feedback in molecular clouds (Mellema et al. 2006a; Mac Low et al. 2007; Dale et al. 2007a,b; Krumholz et al. 2007; Gritschneder et al. 2009), and planetary nebulae (*e.g.* Mellema et al. 1998; Lim & Mellema 2003). In some of these problems, fast, R-type I-fronts predominate. Those fronts propagate faster than the hydrodynamic response of the gas, so gas motions do not affect the I-front evolution. In these cases the radiative transfer could be done on a fixed density field (or a succession of such fields), and dynamic coupling to the gas is generally not required. However, the majority of astrophysical and cosmological applications involve slow, D-type I-fronts (or a combination of R-type and D-type, as we describe in detail in section 3.1), so the radiative transfer and gasdynamics should be directly coupled and evolved simultaneously. Until recently, self-consistent radiation hydrodynamical codes for radiative transport have been rare, but this unsatisfactory situation is now rapidly changing due to the development of a number of such codes using a variety of numerical approaches.

A number of radiative transfer methods have been developed in recent years, both stand-alone and coupled to hydrodynamics. High computational costs necessitate the usage of various approximations. Thus, it is of prime importance to validate the numerical methods developed and to evaluate their reliability and accuracy. Tests with either exact or good approximate analytical solutions should always be the first choice for code testing. Extensive test suites of radiation hydrodynamical I-front transport in a variety of stratified media with good approximate analytical solutions do exist (Franco et al. 1990; Whalen & Norman 2006) and are stringent tests of coupling schemes between radiation, gas, and chemistry. However, an alternative and complementary approach is to compare a variety of methods on a set of well-defined problems in astrophysical settings. This is the approach we have taken in this project.

Our aim is to determine the type of problems the codes are (un)able to solve, to understand the origin of any differences inevitably found in the results, to stimulate improvements and further developments of the existing codes and, finally, to serve as a benchmark for testing future algorithms. All test descriptions, parameters, and results can be found at the project website:
$http://www.cita.utoronto.ca/\sim iliev/rtwiki/doku.php$.

The first paper of this comparison project discussed the results from fixed density field tests (Iliev & et al. 2006, hereafter Paper I), i.e. without any gas evolution. We found that all participating codes are able to track I-fronts quite well, within $\sim$10% of each other. Some important differences also emerged, especially in the derived temperatures and spectral hardening. We found that some of these differences were due to variations in microphysics (chemical reaction rates, heating/cooling rates and photoionization cross-sections), while others were due to the method itself, *e.g.* how the energy equation is solved, how many frequency bins are used for the spectral evolution, etc. We concluded that the tested radiative transfer methods are producing reliable results overall, but that not all methods are equally appropriate for any given problem, especially in cases when obtaining precise temperatures and spectral features is important.

We now extend our previous work by considering a set of radiation hydrodynamical tests. In the spirit of Paper I, we have chosen a set of test problems which are relatively simple, so as to be most inclusive given the current limitations of the available codes (*e.g.* 1-D or 2-D vs. 3-D codes). At the same time, our tests consider problems of astrophysical importance, and cover a wide variety of situations that test the attributes of each method, including its radiative and hydrodynamic components and their coupling.

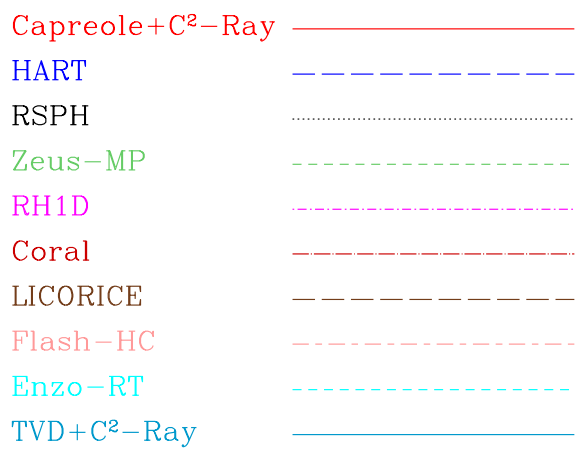

Figure 1. Legend for the line plots.

The efficiency, optimization and performance of the codes are very important, especially for the most complex and computationally-intensive problems. However, there are a number of complications, which we discussed in Paper I, preventing us from doing such testing in a meaningful way at present. We therefore leave it for future work.

All test results for this study had to be supplied on a regular Cartesian grid of 128^3 computational cells. This relatively modest resolution was chosen in the interests of inclusivity, so that even codes which are not yet fully optimized in terms of either computations or memory can participate in the comparison. We note that production runs at present are typically run at 256^3 or better resolution. Codes which utilize Adaptive Mesh Refinement (AMR) grids or particles have been requested to run the problem at the resolution which approximates as closely as possible the fixed-grid one for fair comparison. Their results have then been interpolated onto a regular grid for submission.

2 THE CODES

In this section we briefly describe the nine radiative transfer codes participating in this stage of the comparison project, with references to more detailed method papers if available. Details of the codes and their basic features and methods are summarized in Table 1. Figure 1 provides a legend allowing the reader to identify which line corresponds to which code in the figures throughout the paper. The images we present are identified in the corresponding figure caption.

2.1 Capreole+C^2-Ray and TVD+C^2-Ray (G. Mellema, I. Iliev, P. Shapiro, M. Alvarez)

C^2-Ray (Mellema et al. 2006b) is a grid-based short characteristics (*e.g.* Raga et al. 1999) ray-tracing code which is photon-conserving and causally traces the rays away from the ionizing sources up to

Table 1. Participating codes and their current features.

Code	Grid	Parallelization	hydro method	rad. transfer method
Capreole+C^2-Ray	fixed	shared/distributed	Eulerian, Riemann solver	short-characteristics ray-tracing
TVD+C^2-Ray	fixed	shared/distributed	Eulerian, TVD solver	short-characteristics ray-tracing
HART	AMR	shared/distributed	Eulerian, Riemann solver	Eddington tensor moment
RSPH	particle-based	distributed	SPH	long-characteristics ray-tracing
ZEUS-MP	fixed	distributed	Eulerian	3-D ray-tracing
RH1D	sph. Lagrangian	no	Lagrangian	1-D ray-tracing
Coral	AMR	no	Eulerian, flux-vector splitting	short-characteristics ray tracing
LICORICE	AMR	shared	SPH	Monte-Carlo ray-tracing
Flash-HC	AMR	distributed	Eulerian, PPM	Hybrid characteristics ray-tracing
Enzo-RT	fixed	distributed	Eulerian, PPM	Flux-limited diffusion

each cell. Explicit photon-conservation is assured by taking a finite-volume approach when calculating the photoionization rates, and by using time-averaged optical depths. The latter property allows for integration time steps that are much larger than the ionization time scale, which results in a considerable speed-up of the calculation and facilitates the coupling of the code to gasdynamic evolution. The code and the various tests performed during its development are described in detail in Mellema et al. (2006b).

The frequency dependence of the photoionization rates and photoionization heating rates are dealt with by using frequency-integrated rates, stored as functions of the optical depth at the ionization threshold. In its current version the code includes only hydrogen and no helium, although it could be added in a relatively straightforward way.

The transfer calculation is done using short characteristics, where the optical depth is calculated by interpolating values of grid cells lying along the line-of-sight towards the source. Because of the causal nature of the ray-tracing, the calculation cannot easily be parallelized through domain decomposition. However, using OpenMP and MPI the code is efficiently parallelized over the sources and grid octants (Iliev et al. 2008b). The code has been applied for large-scale simulations of cosmic reionization and its observability (Iliev et al. 2006b; Mellema et al. 2006c; Iliev et al. 2007a,b; Holder et al. 2007; Doré et al. 2007; Iliev et al. 2008a) on grid sizes up to 406^3 and up to $\sim 10^6$ ionizing sources, running on up to 10,240 computing cores.

There are 1D, 2D and 3D versions of the code that are available. It was developed to be directly coupled with hydrodynamics calculations. The large time steps allowed for the radiative transfer enable the use of the hydrodynamic time step for evolving the combined system. The C^2-Ray radiative transfer and nonequilibrium chemistry code has been coupled to several different gasdynamics codes, utilizing both fixed and adaptive grids. The tests in this project were mostly performed with the version coupled to the hydrodynamics code Capreole developed by Garrelt Mellema and based on Roe's approximate Riemann solver. The first gasdynamic application of our code is presented in Mellema et al. (2006a). Additionally, one of the tests has also been run with C^2-Ray coupled to a different hydro solver, namely the TVD method of Trac & Pen (2004) (see Test 6 below).

2.2 Hydrodynamic Adaptive Refinement Tree (HART) (N. Gnedin, A. Kravtsov)

The Hydrodynamic Adaptive Refinement Tree (HART) code is an implementation of the AMR technique and uses a combination of multi-level particle-mesh and shock-capturing Eulerian methods for simulating the evolution of the dark matter particles and gas, respectively. High dynamic range is achieved by applying adaptive mesh refinement to both gas dynamics and gravity calculations.

The code performs refinements locally on individual cells, and cells are organized in refinement trees (Khokhlov 1998). The data structure is designed both to reduce the memory overhead for maintaining a tree and to fully eliminate the neighbor search required for finite-difference operations. All operations, including tree modifications and adaptive mesh refinement, can be performed in parallel. The advantage of the tree-based AMR is its ability to control the computational mesh on the level of individual cells. This results in a very efficient and flexible (and thus highly adaptive) refinement mesh which can be easily built and modified and, therefore, effectively match the complex geometry of cosmologically interesting regions: filaments, sheets, and clumps. Several refinement criteria can be combined with different weights allowing for a flexible refinement strategy that can be tuned to the needs of each particular simulation. The adaptive refinement in space is accompanied by a temporal refinement (smaller time steps on meshes of higher resolutions).

The ART code was initially developed by A. Kravtsov in collaboration with A. A. Klypin and A. M. Khokhlov (Kravtsov et al. 1997; Kravtsov 1999; Kravtsov et al. 2002). N. Gnedin joined the HART code development team in the spring of 2003 and has adopted the OTVET algorithm for modeling 3D radiative transfer for the ART mesh structure and implemented a non-equilibrium chemical network and cooling (e.g. Gnedin et al. 2008).

2.3 RSPH (H. Susa, M. Umemura, D. Sato)

The Radiation-SPH (RSPH) scheme is specifically designed to investigate the formation and evolution of first-generation objects at $z \gtrsim 10$, where the radiative feedback from various sources plays important roles. The code can compute the fraction of chemical species e^-, H^+, H, H^-, H_2, and H_2^+ by fully implicit time integration. It also can deal with multiple sources of ionizing radiation, as well as with Lyman-Werner band photons.

Hydrodynamics is calculated by the smoothed particle hydrodynamics (SPH) method. It uses the version of SPH by Umemura

(1993) with the modification according to Steinmetz & Mueller (1993), and adopts the particle resizing formalism by Thacker et al. (2000). The present version does not use the so-called entropy formalism (Springel & Hernquist 2002). The non-equilibrium chemistry and radiative cooling for primordial gas are calculated using the code developed by Susa & Kitayama (2000), where H_2 cooling and reaction rates are taken from Galli & Palla (1998a).

As for the photoionization process, the on-the-spot approximation is employed (Spitzer 1978), meaning that the transfer of ionizing photons directly from the source is solved, but diffuse photons are not transported. Instead, it is assumed that recombination photons are absorbed in the same zone from which they are emitted. Due to the absence of the source term in this approximation, the radiation transfer equation becomes very simple. Solving the transfer equation reduces to the easier problem of assessing the optical depth from the source to every SPH particle.

The optical depth is integrated utilizing the neighbour lists of SPH particles. It is similar to the code described in Susa & Umemura (2004), but can now also deal with multiple point sources. In the new scheme fewer grid points are created on the light ray than in its predecessor. Instead, just one grid point per SPH particle is created in the particle's neighborhood. The 'upstream' particle for each SPH particle on its line of sight to the source is then found. Then the optical depth from the source to the SPH particle is obtained by summing up the optical depth at the 'upstream' particle and the differential optical depth between the two particles.

The code is parallelized with the MPI library. The computational domain is divided by the Orthogonal Recursive Bisection method. The parallelization method for radiation transfer is similar to the Multiple Wave Front method developed by Nakamoto et al. (2001) and Heinemann et al. (2006), but it is adapted to fit the SPH code as described in (Susa 2006).

The code computes self-gravity using a Barnes-Hut tree, which is parallelized as well. A Tree-GRAPE version of the code has also been developed. This code has been applied to radiative feedback in primordial star formation (Susa & Umemura 2006; Susa 2007; Hasegawa et al. 2009), as well as the regulation of star formation in forming galaxies by ultraviolet background (Susa 2008).

2.4 ZEUS-MP (D. Whalen, J. Smidt, M. Norman)

ZEUS-MP solves explicit finite-difference approximations to Euler's equations of fluid dynamics self-consistently with a 9-species primordial gas reaction network (H, H^+, He, He^+, He^{++}, H^-, H_2, H_2^+ and e) and ray-tracing radiative transfer, which is used to compute the radiative rate coefficients required by the network and the gas energy equation. Our method is described in detail elsewhere (Whalen & Norman 2006, 2008b); here, we review multifrequency upgrades to the radiative transfer and improvements to the subcycling scheme (Whalen & Norman 2008a).

The ZEUS-MP RT module evaluates radiative rate coefficients by solving the static equation of transfer in flux form. To obtain the total rate coefficient k for a zone we sum the k_ν computed for a given binned photon emission rate over all energies by looping the solution to the transfer equation over them. In tests spanning 40 to 2000 energy bins, good convergence is found with 120 bins, 40 bins spaced evenly in energy from 0.755 eV to 13.6 eV and 80 bins that are logarithmically-spaced from 13.6 eV to 90 eV.

Successive updates to the reaction network and gas energy are performed over the minimum of the chemical time

$$t_{chem} = 0.1\,\frac{n_e + 0.001 n_H}{\dot{n}_e}. \tag{1}$$

and the photoheating/cooling time

$$t_{hc} = 0.1 \frac{e_{gas}}{\dot{e}_{ht/cool}} \tag{2}$$

until the larger of these two times has been crossed, at which point full hydrodynamical updates of gas densities, energies, and velocities are performed. These times are global minima for the entire grid. Chemical times are defined in terms of electron flow to accommodate all chemical processes rather than just ionizations or recombinations. Adopting the minimum of the two times for chemistry and gas energy updates enforces accuracy in the reaction network when t_{chem} becomes greater than t_{hc} (in relic H II regions, for example).

ZEUS-MP is now fully parallelized for three-dimensional applications. We have updated the H and He recombination and cooling rates responsible for some minor departures between ZEUS-MP and the other codes in Paper I in the temperature structure of H II regions, and now use the most recent data from Hummer (1994) and Hummer & Storey (1998). Our code has been validated with stringent tests of R-type and D-type I-fronts in a variety of stratified media (Franco et al. 1990; Whalen & Norman 2006) and applied to both cosmological and astrophysical problems, such as the breakout of UV radiation from primordial star-forming clouds (Whalen et al. 2004), the formation of dynamical instabilities in galactic H II regions (Whalen & Norman 2008b), the circumstellar environments of gamma-ray bursts (Whalen et al. 2008b), the photoevaporation of cosmological minihalos by nearby primordial stars (Whalen et al. 2008a), and Pop III supernovae explosions in cosmological H II regions (Whalen et al. 2008c).

2.5 RH1D (K. Ahn, P. Shapiro)

RH1D is a 1D, Lagrangian, spherically-symmetric, radiation-hydrodynamics code for a two-component gas of baryons and collisionless dark matter coupled by gravity (Ahn & Shapiro 2007). For the baryonic component, the Euler equations and the equation of state are solved, together with multi-frequency, multi-species radiative transfer equations and a reaction network with nine primordial species (H, H^+, He, He^+, He^{++}, H^-, H_2, H_2^+ and e). Dark matter dynamics, governed by the collisionless Boltzmann equations, takes a simplified form in spherical symmetry. The code solves an effective set of Euler equations for a dark matter fluid, based upon the "fluid approximation" of dark matter dynamics for a spherically symmetric system with an isotropic velocity dispersion, derived and justified elsewhere (Ahn & Shapiro 2005). These effective Euler equations are identical to those for an inviscid, ideal gas with a ratio of specific heats $\gamma = 5/3$.

The Euler equations are solved using the so-called "leap-frog" method, where the Lagrangian position (radius) and velocity (radial velocity) are staggered in time to achieve a second-order accuracy in time steps, both for baryonic and dark matter fluid. The usual artificial viscosity scheme is used to capture shocks. We typically adopt a few thousand uniformly spaced bins in radius. Non-equilibrium rate equations for the nine primordial species are solved using the backward differencing scheme of Anninos et al. (1997). For H^- and H_2^+, due to their relatively fast reaction rates, the equilibrium values may be used.

Radiative transfer is performed by ray-tracing, taking account of the optical depth to bound-free opacity of H I, He I, He II, H^-, and H_2, as well as bound-free and dissociation opacity of H_2^+. The

optical depth to the Lyman-Werner band photons of H_2, which are capable of dissociating H_2, is treated using a pre-calculated self-shielding function by Draine & Bertoldi (1996), which is determined by the H_2 column density and gas temperature. Diffuse flux is not explicitly calculated, but is accounted for implicitly by adopting case B recombination rates. The radiative reaction rates are calculated using a photon-conserving scheme, which enables the code to treat optically-thick shells (*e.g.* Razoumov & Scott 1999; Abel et al. 1999a). A wide range of radiation frequency (energy), $h\nu \sim [0.7 - 7000]\,\mathrm{eV}$, is covered by a few hundred, logarithmically spaced bins, together with additive, linearly spaced bins where radiative cross sections change rapidly as frequency changes. For each frequency and species, the corresponding radiative reaction rate is calculated, then summed over frequency to obtain the net radiative reaction rate.

The radiative transfer scheme is able to treat 1) an internal point source, 2) an external, radially-directed source, and 3) an external, isotropic background. The transfer for (1) and (2) is 1D, performed along the radial direction only. For (3), the transfer is 2D in nature, and at each point the mean intensity is required to calculate the radiative rates, which involves an angle integration. The radiative transfer calculation is performed for each pre-selected angle (θ, measured from the radial direction), and then the angle integral is calculated using the Gaussian quadrature method.

The code adopts a very stringent time step criterion for accuracy. The minimum of dynamical, sound-crossing, cooling/heating, and species change time scales, which is multiplied by a coefficient smaller than unity (~ 0.1), is chosen as the time step. All the Euler equations and rate equations are solved with this time step, which makes the whole calculation self-consistent. This code has been tested extensively and used to study the radiative feedback effects by the first stars on their nearby minihalos (Ahn & Shapiro 2007).

2.6 Coral (I. Iliev, A. Raga, G. Mellema, P. Shapiro)

CORAL is a 2-D, axisymmetric Eulerian fluid dynamics AMR code (see Mellema et al. 1998; Shapiro et al. 2004, and references therein for detailed description). It solves the Euler equations in their conservative finite-volume form using the second-order method of van Leer flux-splitting, which allows for correct and precise treatment of shocks. The grid refinement and de-refinement criteria are based on the gradients of all code variables. When the gradient of any variable is larger than a pre-defined value the cell is refined, and when the criterion for refinement is not met the cell is de-refined.

The code follows, by a semi-implicit method, the non-equilibrium chemistry of multiple species (H, He, C II-VI, N I-VI, O I-VI, Ne I-VI, and S II-VI) and the corresponding cooling (Raga et al. 1997; Mellema et al. 1998), as well as Compton cooling. The photoheating rate is the sum of the photoionization heating rates for H I, He I and He II. For computational efficiency all heating and cooling rates are pre-computed and stored in tables. The microphysical processes – chemical reactions, radiative processes, transfer of radiation, heating and cooling – are implemented though the standard approach of operator-splitting (i.e. solved at each time-step, side-by-side with the hydrodynamics and coupled to it through the energy equation). The latest versions of the code also include the effects of an external gravity force.

Currently the code uses a black-body or power-law ionizing source spectrum, although any other spectrum can be accommodated. Radiative transfer of the ionizing photons is treated explicitly by taking into account the bound-free opacity of H and He in the photoionization and photoheating rates. The photoionization and photoheating rates of H I, He I and He II are pre-computed for the given spectrum and stored in tables vs. the optical depths at the ionizing thresholds of these species, which are then used to obtain the total optical depths. The code correctly tracks both fast (by evolving on an ionization timestep, $\Delta t \sim \dot{n_{\mathrm{H}}}/n_{\mathrm{H}}$) and slow I-fronts.

The code has been tested extensively and has been applied to many astrophysical problems, *e.g.* photoevaporation of clumps in planetary nebulae (Mellema et al. 1998), cosmological minihalo photoevaporation during reionization (Shapiro et al. 2004; Iliev et al. 2005), and studies of the radiative feedback from propagating ionization fronts on dense clumps in damped Lyman-α systems (Iliev et al. 2006a).

2.7 LICORICE: LIne COntinuum Radiative tranfer Integrated Computing Engine (S. Baek, B. Semelin, F. Combes)

The LICORICE code has three main components: TreeSPH to compute gravity and hydrodynamics, continuum radiative transfer with hydrogen and helium ionization physics, and Lyman-alpha line transfer. The latter is not relevant to this comparison and has been described elsewhere. The ionizing continuum transfer has been described in details in Baek et al. (2009).

The current version of LICORICE does not include H_2 formation, or diffuse radiation from recombinations, but they will be incorporated in the future. LICORICE uses SPH particles for the gas dynamics and an adaptive grid for the radiative transfer. Physical quantities are interpolated from one to the other as required.

The fluid dynamics are followed using a TreeSPH method. The implementation is described in detail in Semelin & Combes (2002) and Semelin & Combes (2005). Since there are many varieties of SPH, we summarize the main features of our algorithm here. We use a spherically-symmetric spline-smoothing kernel and 50 neighbours to compute the SPH quantities using an arithmetic average between the neighbours of the smoothing length h and the simple viscosity scheme by Monaghan (1992).

For the tests in this paper we implemented transmissive boundary conditions. This was achieved as follows: for each SPH particle within a distance of the simulation box boundary smaller than its smoothing length h, we create a symmetrical 'ghost' particle on the other side of the boundary. All physical quantities for this ghost particle are equal to those of the initial particle, including the velocity. The ghost particles are used as neighbours to compute the SPH quantities of real particles. The ghost particles are erased and recreated at each time step.

The continuum radiative transfer is solved using a Monte Carlo approach similar to the one employed in the CRASH code (Maselli et al. 2003). Here we summarize only the differences between LICORICE and CRASH. We compute the gas density at each particle's position with the SPH smoothing kernel, and physical quantities such as ionization fraction and temperature are updated according to these particle densities. The density field is generally smooth, but may sometimes show spurious fluctuations if the particle number density changes sharply. This is a well known but unavoidable problem with SPH.

The radiation field is discretized into photon packets and propagated through cells along directions chosen at random. The cells form an adaptive grid which is derived from the tree structure of the particle distribution. Our adaptive grid is built to keep the number of particles in each cell within a given range (1 to 8 and 1 to 1 ranges have been used). This yields greater resolution in the denser

regions. The adaptive grid also requires fewer cells than a fixed grid to best sample a given inhomogeneous particle distribution, thus saving both memory and CPU time.

The time step for updating physical quantities within a cell is also adaptive. We update the physical quantities for all cells and particles after the propagation of the number of photon packets corresponding to an integration time dt. However, if the number of accumulated photons in a cell during this integration time is greater than a pre-set limit (*e.g.* 10% of the total number of neutral hydrogen atoms in the cell), we update the physical quantities in this cell with a time step $dt' < dt$ corresponding to the time elapsed since the last update.

The test results are interpolated from the particle distribution onto the 128^3 uniform Cartesian grids required in this study. Currently, the dynamical part of the code is parallelized for both shared and distributed memory architectures using OpenMP and MPI, while the radiative transfer is parallelized with OpenMP only. The code can now handle 256^3 particles, to be increased to 512^3 in the near future. We note that compared to a uniform grid with the same number of cells, the SPH Lagrangian approach results in higher resolution in the dense regions, but lower resolution in more diffuse regions.

2.8 Flash-HC: Hybrid Characteristics (T. Theuns, M. Raicevic, E.-J. Rijkhorst)

The Hybrid Characteristics (HC) method (Rijkhorst 2005; Rijkhorst et al. 2006) is a three-dimensional ray-tracing scheme for parallel AMR codes. It combines elements of long and short characteristics, using the precision and parallelizability of the former with efficient execution through interpolation of the latter. It has been implemented into the Flash-HC AMR code (Fryxell et al. 2000), enabling simulations of radiation hydrodynamics problems with point sources of radiation. The public version of the Flash code (which does not currently include this radiative transfer module) can be downloaded from

$http://flash.uchicago.edu/website/home/$.

The block-structured AMR grid used in Flash-HC is distributed over processors using a space-filling curve. Parallel ray tracing requires each ray to be split in the independent sections where the ray traverses the blocks held by a given processor. First, every processor traces rays on its local blocks in directions which start from the source, and end in the corners of each cell on the faces of the (cubic) block. Since rays cross several blocks, interpolation is used to assemble a ray from local block contributions. However, because some of these blocks will be held by other processors, local column densities need to be exchanged in one global communication. Note that only face values are exchanged. Finally, local and imported column densities are combined using interpolation to assemble the complete ray. At the end of this parallel operation, each cell has the total column density to the source along a ray that traverses all intervening cells at the full resolution of the AMR grid. Interpolation coefficients are chosen such that the exact solution for the column density is obtained for a uniform density distribution. Even in a non-uniform density distribution, for example $1/r^2$, the differences between the value of the correct column density and that obtained using HC is typically less than half a percent.

Recent improvements introduced since Paper I include the implementation of a fully photon conserving chemistry solver, taking into account the effects of both spatial and temporal discretization (Abel et al. 1999b; Mellema et al. 2006b). This implementation employs the Livermore Solver for Ordinary Differential Equations (LSODE Hindmarsh 1980), which, although more computationally intensive than the original solver used in DORIC (Frank & Mellema 1994), eliminates the need for an independent radiative transfer time step irrespective of the ionization front type and guarantees correct front positions and ionization heating. Details of the scheme will be presented elsewhere. Additional functionality allows for a radiation source outside of the computational volume, a feature used in Test 7 to approximate a parallel ionization front.

The parallel scaling of HC was examined in Rijkhorst (2005) and Paper I; the algorithm scales well for ~ 100 processors on a SGI Altix, and ~ 1000 processors on a IBM Blue Gene/L systems. The algorithm scales linearly with the number of sources. The photon-conserving RT and chemistry upgrades should not affect HC's scaling.

2.9 Enzo-RT (D.R. Reynolds, M.L. Norman, J.C. Hayes, P. Paschos)

The Enzo-RT code is an extension to the freely-available Enzo code[1] that self-consistently incorporates coupled radiation transport and chemical ionization kinetics within Enzo's formulation for cosmological hydrodynamics on AMR meshes (Norman et al. 2007). In Enzo-RT we approximate the radiation transport processes using a single integrated radiation energy density in each spatial cell that is propagated with flux-limited diffusion on a finite-volume mesh. The radiation field is implicitly coupled in time to a multi-species chemical reaction network. This implicit radiation chemistry system is then coupled in an operator-split fashion with Enzo's cosmological hydrodynamics solver, which utilizes the Piecewise Parabolic Method for the advection of matter and gas energy (Colella & Woodward 1984). The coupled algorithm, along with a suite of verification tests, is fully described in Reynolds et al. (2009).

The frequency dependence of the photoionization rates is treated by integrating a prescribed radiation frequency spectrum, typically chosen to be either monochromatic, blackbody, or a $\left(\frac{\nu}{\nu_0}\right)^{-\beta}$ power law. This integration is performed upon initialization of the solver and the integrated rates are re-used throughout the simulation. In the current version of the code, only a single radiation profile is allowed, although this formulation may be easily extended to allow for multifrequency calculations.

The solver for propagating radiation throughout the domain follows a standard flux-limited diffusion model, in which the radiation flux $\mathbf{F}$ is approximated by

$$\mathbf{F} = -\frac{1}{a} D \nabla E. \tag{3}$$

Here E is the radiation energy density, and the flux-limiter D smoothly connects the limiting cases of (nearly) isotropic and free-streaming radiation:

$$D(E) = diag(D_1(E), D_2(E), D_3(E)), \tag{4}$$

where

$$D_i(E) = \frac{c(2\kappa_T + R_i)}{6\kappa_T^2 + 3\kappa_T R_i + R_i^2}, \quad i = 1, \ldots, 3, \tag{5}$$

and $R_i = |\partial_i E|/E$, c is the speed of light, and κ_T is the opacity.

The coupled implicit radiation-chemistry system further includes a gas energy feedback field, which allows us to self-consistently heat and cool the gas in an operator-split manner,

[1] http://lca.ucsd.edu/portal/software/enzo

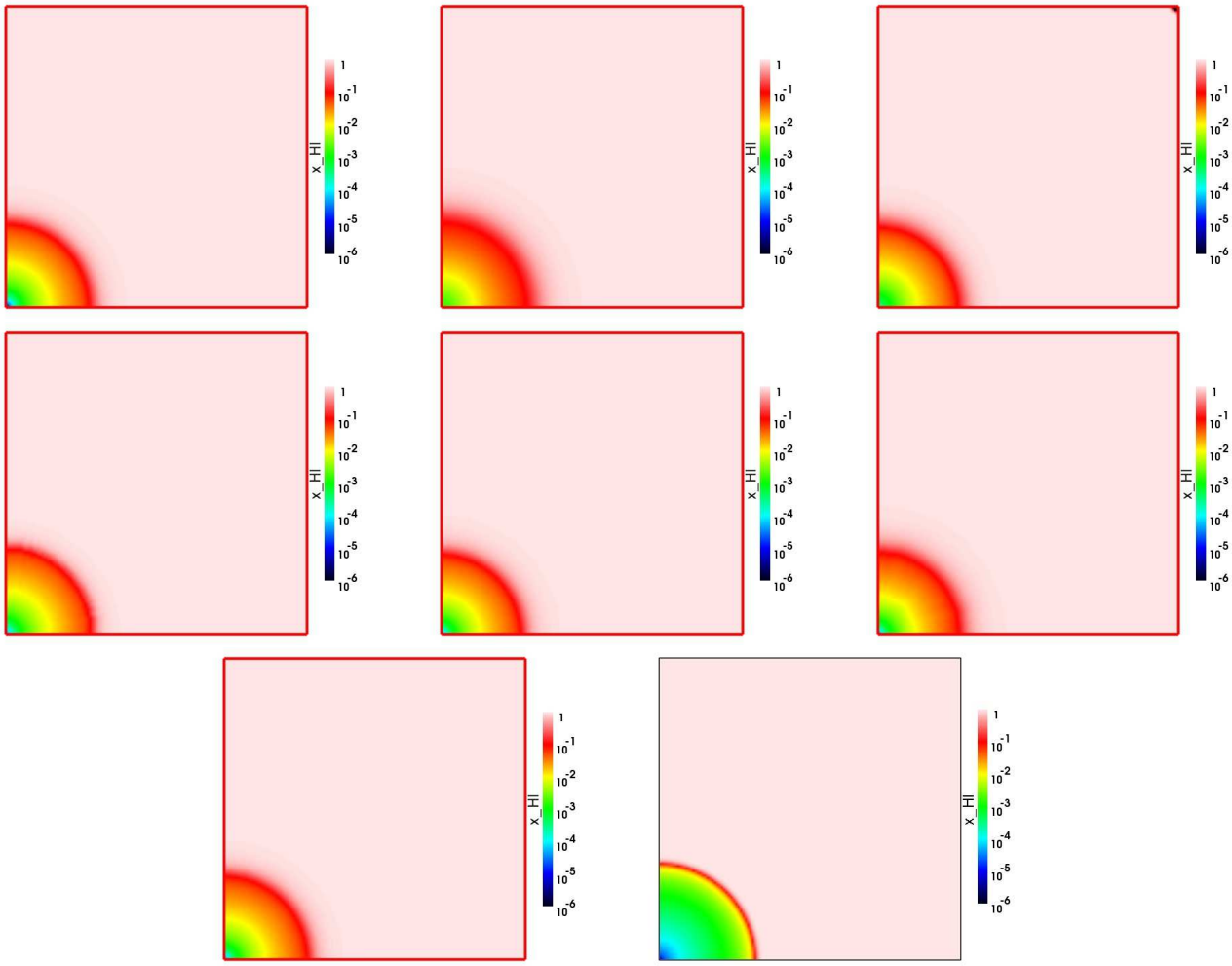

Figure 2. Test 5 (H II region expansion in an initially-uniform gas): Images of the H I fraction, cut through the simulation volume at coordinate $z = 0$ at time $t = 100$ Myr for (left to right and top to bottom) Capreole+C^2-Ray, HART, RSPH, ZEUS-MP, RH1D, LICORICE, Flash-HC and Enzo-RT.

capturing all of the stiff components involved in radiation transport, primordial chemistry and thermal heating/cooling in a tightly-coupled implicit system. Enzo's explicit Eulerian hydrodynamics solver and its parallel implementation have been exhaustively described elsewhere (Norman et al. 2007). Parallelism of the coupled implicit system follows a standard domain-decomposition approach and is solved using state-of-the-art Newton-Krylov-Multigrid solvers (Knoll & Keyes 2004), potentially allowing scalability of the algorithm to up to tens of thousands of processors.

While Enzo allows for spatial adaptivity through structured adaptive mesh refinement (SAMR), our initial implementation of Enzo-RT is currently limited to uniform grids in 1-, 2- or 3-dimensions, although their upgrade to AMR is under development. Extensions of this approach to variable Eddington tensors, multi-group flux-limited diffusion, or multigroup variable Eddington tensors are easily accommodated within our implicit formulation and are planned as future extensions. One benefit is that the timestep is independent of grid resolution, at least for the radiation solve. Another advantage of our approach is that by defining radiation as a field variable, scalability with respect to the number of point sources ceases to be an issue. Instead, scalability is dictated by the underlying linear system solver, which for the case of multigrid is optimal.

3 RADIATION HYDRODYNAMICS TESTS: DESCRIPTION

For simplicity and inclusivity (since currently not all codes have implemented helium or metals chemistry and cooling) all tests assume the gas to be composed of pure hydrogen.

3.1 Test 5: Classical H II Region Expansion

Test 5 is the classical problem of the expansion of an I-front due to a point source in an initially uniform-density medium. In general, I-fronts are classified according to their speed with respect to the gas and the change in gas density through the I-front (c.f. Kahn & Dyson 1965; Spitzer 1978). There are two critical speeds: R-critical, defined as $v_R = 2c_{s,I,2}$, and D-critical, given by $v_D = c_{s,I,2} - (c_{s,I,2}^2 - c_{s,I,1}^2)^{1/2} \approx c_{s,I,1}^2/(2c_{s,I,2})$, where $c_{s,I,1} = (p_1/\rho_1)^{1/2}$ and $c_{s,I,2} = (p_2/\rho_2)^{1/2}$ are the *isothermal* sound speeds in the gas ahead of and behind the I-front, respectively. Note that in the test the gas is *not* assumed to be isothermal. The velocity of the I-front is given by the jump condition $v_I = F/n$ (which guarantees photon conservation), where n is the number density of the neutral gas entering the front and F is the flux of ionizing photons at the I-front transition (which is attenuated due

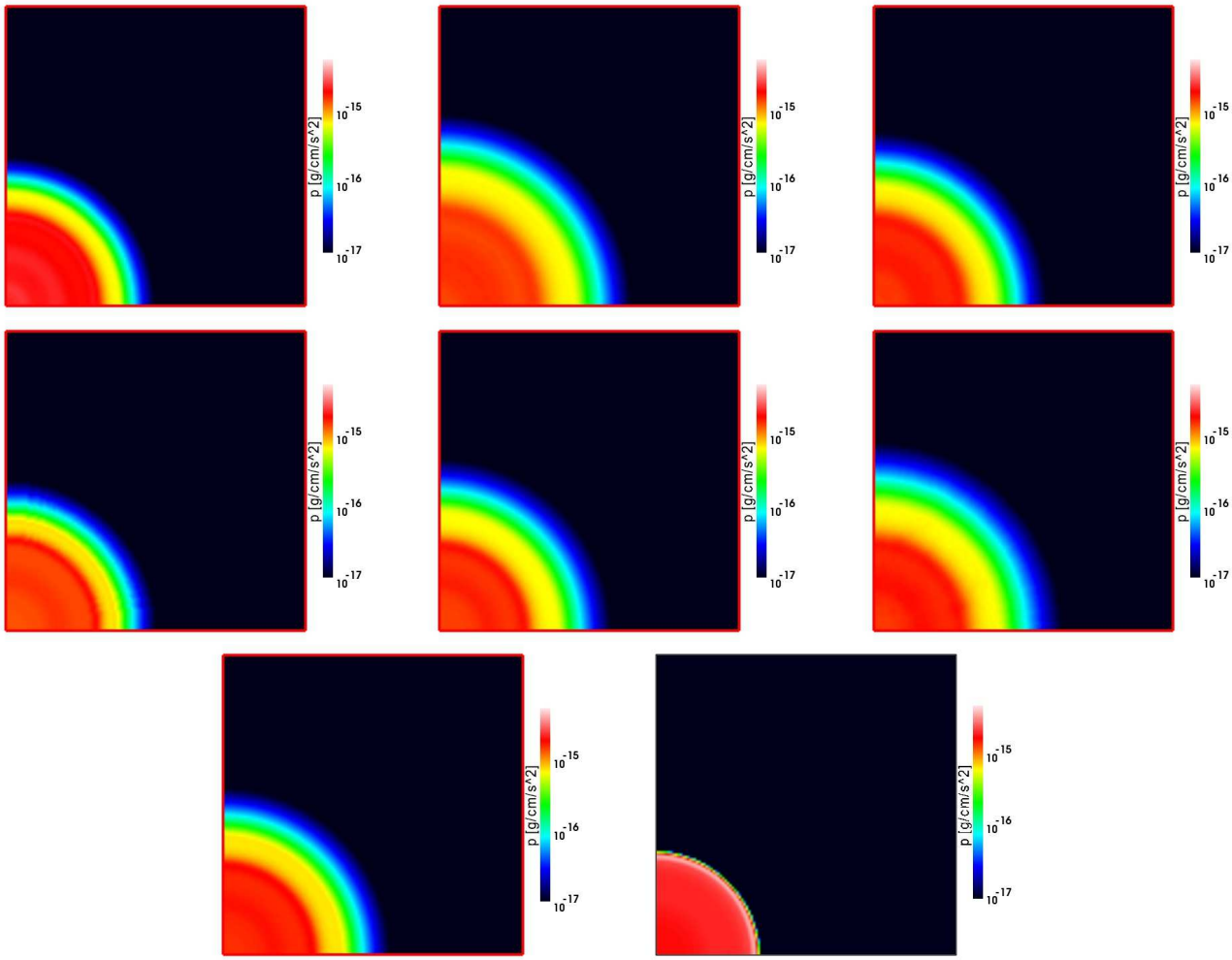

Figure 3. Test 5 (H II region expansion in an initially-uniform gas): Images of the pressure, cut through the simulation volume at coordinate $z = 0$ at time $t = 100$ Myr for (left to right and top to bottom) Capreole+C^2-Ray, HART, RSPH, ZEUS-MP, RH1D, LICORICE, Flash-HC and Enzo-RT.

to absorptions in the gas on the source side). We note that this jump condition is modified significantly for I-fronts moving with relativistic speeds with respect to the gas (Shapiro et al. 2006). This can occur in a number of astrophysical and cosmological environments. However, we do not consider such cases here since currently few radiative transfer codes (and no radiation hydrodynamics codes, to our knowledge) are able to handle such relativistic I-fronts.

When $v_{\rm I} \geqslant v_R$ (*e.g.* close to the source, where the flux F is large) the I-front is R-type (R-critical when $v_{\rm I} = v_R$). R-type I-fronts always move supersonically with respect to the neutral gas ahead, while with respect to the ionized gas the front can move either subsonically (strong R-type, highly compressive, but generally irrelevant to H II regions since it means that the isothermal sound speed behind the front is lower than the one ahead of it), or supersonically (weak R-type, resulting in only slight compression of the gas moving through the front). When $v_{\rm I} \leqslant v_D$, the I-front is D-type (D-critical in the case that $v_{\rm I} = v_D$). The gas passing through this type of I-front always expands, and the front is subsonic with respect to the gas beyond. With respect to the ionized gas, the I-front can again be either supersonic (strong D-type), or subsonic (weak D-type). When $v_D < v_{\rm I} < v_R$ (sometimes referred to as an M-type I-front) the I-front is necessarily led by a shock which compresses the gas entering the I-front sufficiently to slow it down and guarantee that $v_{\rm I} \leqslant v_D$.

In a static medium with number density $n_{\rm H}$ and constant ionized gas temperature T, the evolution of the I-front radius $r_{\rm I}$ and velocity $v_{\rm I}$ for a point source emitting $\dot{N}_\gamma$ ionizing photons per second are given by

$$r_{\rm I} = r_{\rm S}^0 \left[1 - \exp(-t/t_{\rm rec})\right]^{1/3} \quad (6)$$

$$v_{\rm I} = \frac{r_{\rm S}}{3t_{\rm rec}} \frac{\exp\left(-t/t_{\rm rec}\right)}{\left[1 - \exp(-t/t_{\rm rec})\right]^{2/3}} , \quad (7)$$

where

$$r_{\rm S}^0 = \left[\frac{3\dot{N}_\gamma}{4\pi\alpha_B(T) n_{\rm H}^2}\right]^{1/3} , \quad (8)$$

the Strömgren radius (assuming full ionization), which is reached when the number of recombinations in the ionized volume per unit time exactly balances the number of ionizing photons emitted by the source per unit time. This final static stage is commonly referred to as Strömgren sphere. The recombination time is given by

$$t_{\rm rec} = \left[\alpha_B(T) n_{\rm H}\right]^{-1} . \quad (9)$$

Here $\alpha_B(T)$ is the case B recombination coefficient of hydrogen at temperature T in the ionized region.

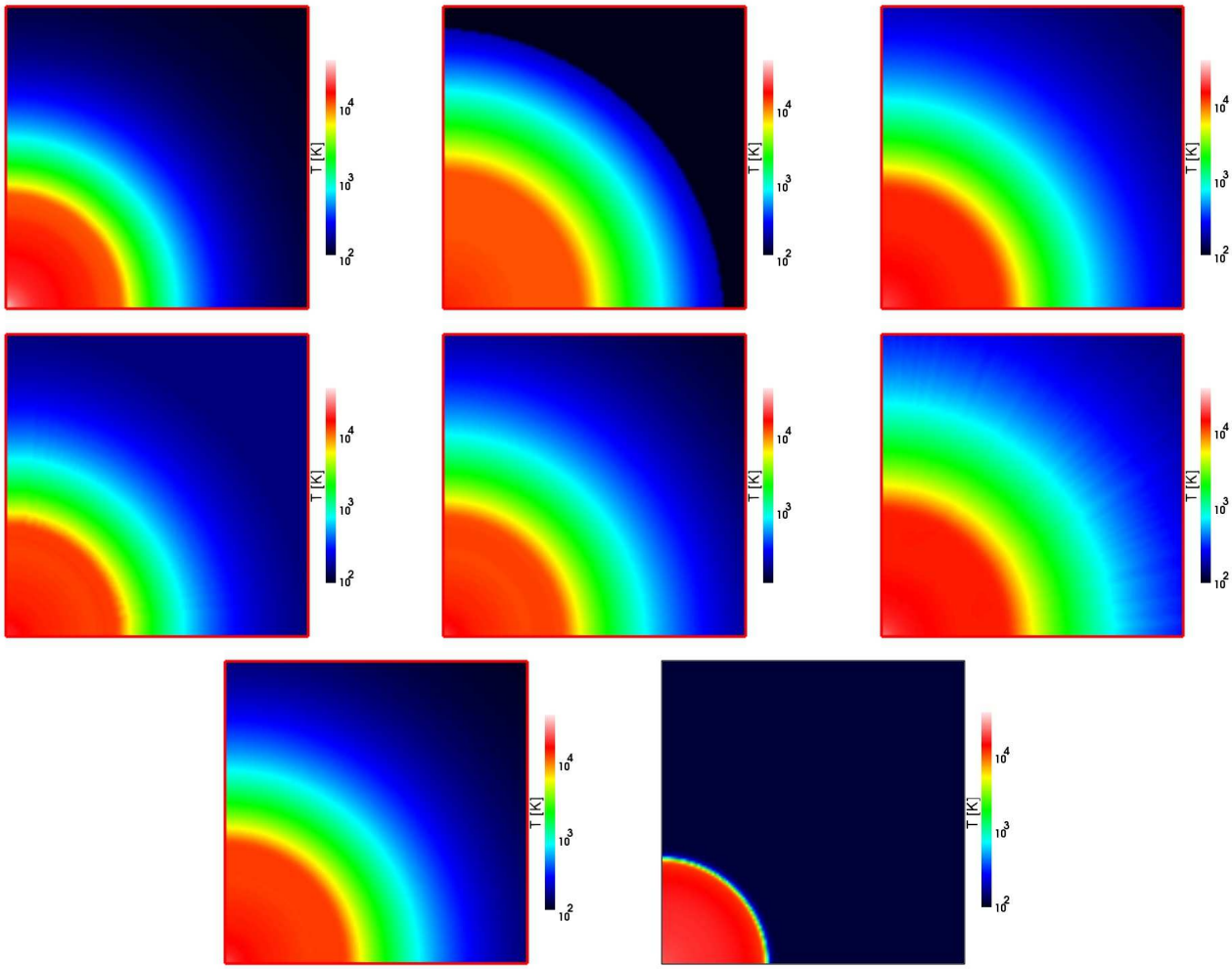

Figure 4. Test 5 (H II region expansion in an initially-uniform gas): Images of the temperature, cut through the simulation volume at coordinate $z = 0$ at time $t = 100$ Myr for (left to right and top to bottom) Capreole+C^2-Ray, HART, RSPH, ZEUS-MP, RH1D, LICORICE, Flash-HC and Enzo-RT.

In reality, the ionized gas is not static and its much higher pressure than that of the ambient medium causes it to expand outward beyond the Stromgren radius. Analytical models predict that in this phase the I-front radius evolves approximately according to (c.f. Spitzer 1978)

$$r_I = r_{\rm S}^0 \left(1 + \frac{7 c_s t}{4 r_{\rm S}^0}\right)^{4/7}, \tag{10}$$

where r_S^0 is the Strömgren radius and c_s is the sound speed in the ionized gas. The expansion finally stalls when a pressure equilibrium is reached. The predicted final H II region radius is

$$r_f = \left(\frac{2T}{T_e}\right)^{2/3} r_S^0, \tag{11}$$

where T is the temperature inside the H II region and T_e is the external temperature. In reality, the evolution is more complicated, with non-uniform temperatures inside the H II region, broadened I-fronts due to pre-heating by energetic photons, etc. Furthermore, equation 10 describes correctly only in the purely pressure-driven, late-time evolution, but not the transition from fast, R-type to D-type I-front. These analytical solutions should therefore only be considered to be guidelines for the expected behaviour, not as exact solutions for this problem.

The numerical parameters for Test 5 are as follows: computational box size $L = 15$ kpc, initial gas number density $n_H = 10^{-3}$ cm^{-3}, initial ionization fraction $x = 0$, constant ionizing photon emission rate $\dot{N}_\gamma = 5 \times 10^{48}\,{\rm s}^{-1}$, initial gas velocity zero and initial gas temperature $T_e = 100$ K. The radiation source is at the $(x_s, y_s, z_s) = (0, 0, 0)$ corner of the computational box. For reference, if we assume that the temperature of the ionized gas is $T = 10^4$ K, and that the recombination rate is given by $\alpha_B(T) = 2.59 \times 10^{-13}\,{\rm cm}^3{\rm s}^{-1}$, we find $t_{\rm rec} = 3.86 \times 10^{15}$ s $=$ 122.4 Myr, $r_S = 5.4$ kpc, and $r_f \approx 185$ kpc. This rough final pressure-equilibrium radius is thus well outside of our computational volume, which was instead chosen to resolve the more physically-interesting transition from R-type to D-type, which occurs around r_S^0. Boundary conditions are reflective for the boundaries which contain the origin (where the ionizing source is positioned) and transmissive for the other boundaries. The ionizing spectrum is that of a 10^5 K black body, as expected for a massive, metal-free Pop III star. Hydrogen line cooling, recombinational cooling, and bremsstrahlung cooling are all included, but not Compton cooling. The simulation running time is $t_{\rm sim} = 500$ Myr $\approx 4\,t_{\rm rec}$. The required outputs are the neutral fraction of hydrogen, gas pressure, temperature and Mach number on the entire grid at $t = 10, 30, 100, 200,$ and 500 Myr, and the I-front position (de-

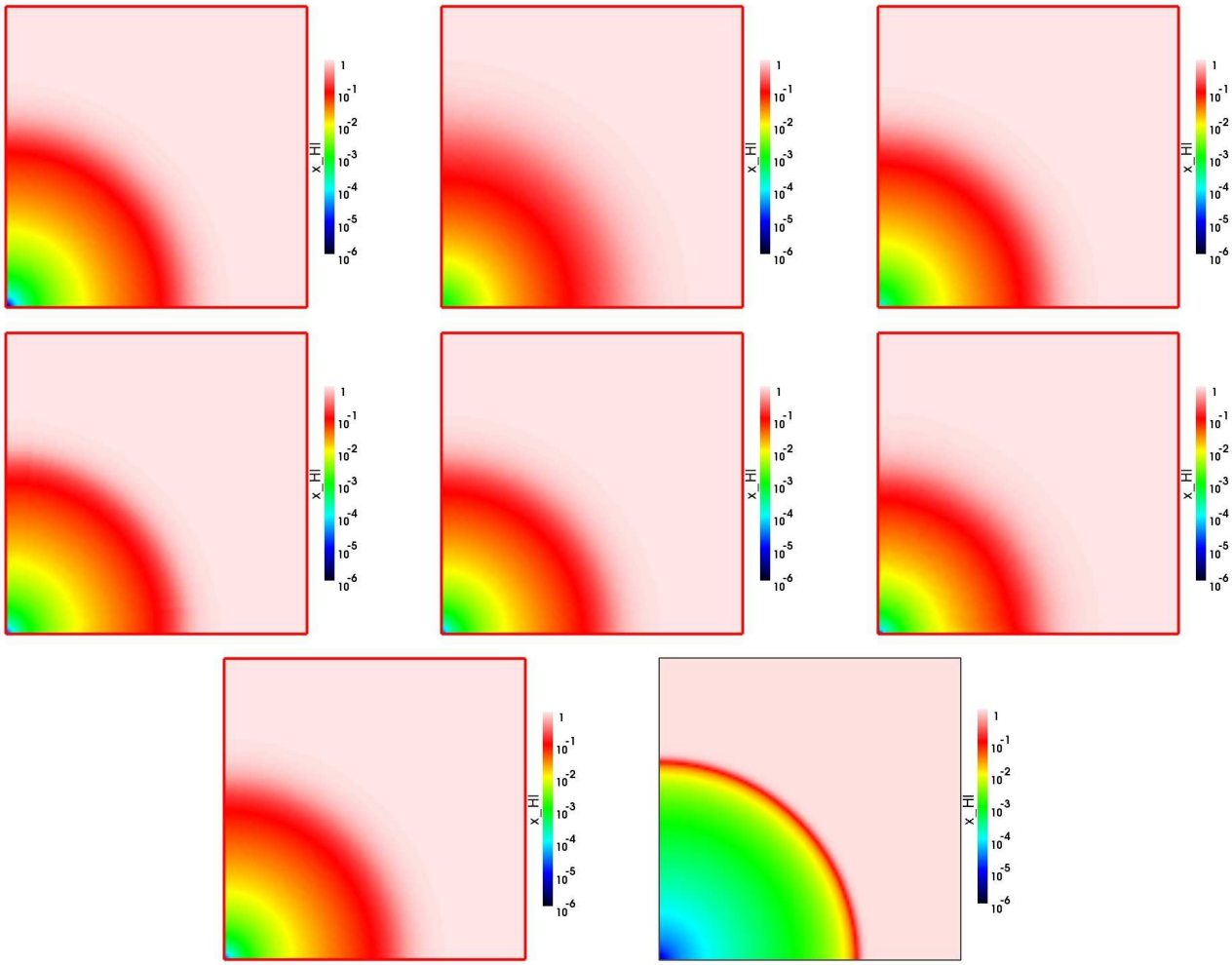

Figure 5. Test 5 (H II region expansion in an initially-uniform gas): Images of the H I fraction, cut through the simulation volume at coordinate $z = 0$ at time $t = 500$ Myr for (left to right and top to bottom) Capreole+C^2-Ray, HART, RSPH, ZEUS-MP, RH1D, LICORICE, Flash-HC and Enzo-RT.

fined as the position where the neutral fraction is 50%) and I-front velocity vs. time along the x-axis.

3.2 Test 6: H II region expansion in $1/r^2$ density profile

Test 6 is the propagation of an I-front created by a point source at the center of a spherically-symmetric, steeply-decreasing power-law density profile with a small flat central core of gas number density n_0 and radius r_0:

$$n_H(r) = \begin{cases} n_0 & \text{if } r \leqslant r_0 \\ n_0(r/r_0)^{-2} & \text{if } r \geqslant r_0 \end{cases}$$

For a static-density medium the evolution of the I-front within the flat-density core is described by equations 6 and 7. In this case, if the Strömgren radius associated with the core density n_0, $r_{S,0} = [3\dot{N}_\gamma/(4\pi\alpha_B(T)n_0^2)]^{1/3}$, is smaller than r_0, the front will come to a halt within the core. If, instead, $r_{S,0} > r_0$, the front escapes the core and propagates into the stratified envelope. Thereafter, the I-front position and velocity as a function of time have complex analytical forms for an arbitrary source fluxes and densities (Mellema et al. 2006b). A simple solution exists for the special case of the central ionizing source rate of photon emission $\dot{N}_\gamma = 16\pi r_0^3 n_0^2 \alpha_B/3$, in which case the I-front radius upon leaving the core is

$$r_I = r_0(1 + 2t/t_{\rm rec,core})^{1/2}, \tag{12}$$

where $t_{\rm rec,core}$ is the recombination time in the core (Mellema et al. 2006b). Similar solutions exist also when the I-front is moving relativistically (Shapiro et al. 2006).

The propagation of an I-front in r^{-2} density profiles with full gas dynamics does not have an exact analytical solution, but has been well studied with both semianalytical and numerical methods (Franco et al. 1990). If $r_{S,0} < r_0$ then the I-front converts to D-type within the core, but starts to re-accelerate upon entering the steep density gradient. Numerical simulations indicate that in density profiles approximating those of galactic molecular cloud cores or cosmological minihalos at high redshift, the I-front remains D-type for the lifetime of typical UV sources (Whalen & Norman 2008a). If $r_{S,0}$ is instead equal to or greater than r_0, the I-front may briefly convert to D-type, but then rapidly reverts to R-type and flash-ionizes the cloud on timescales shorter than the dynamical time of the gas. Now completely ionized and nearly isothermal, strong pressure gradients form wherever there are steep density gradients, the sharpest of which are found at the edge of what was once the edge of the core. These pressure gradients drive the gas outward

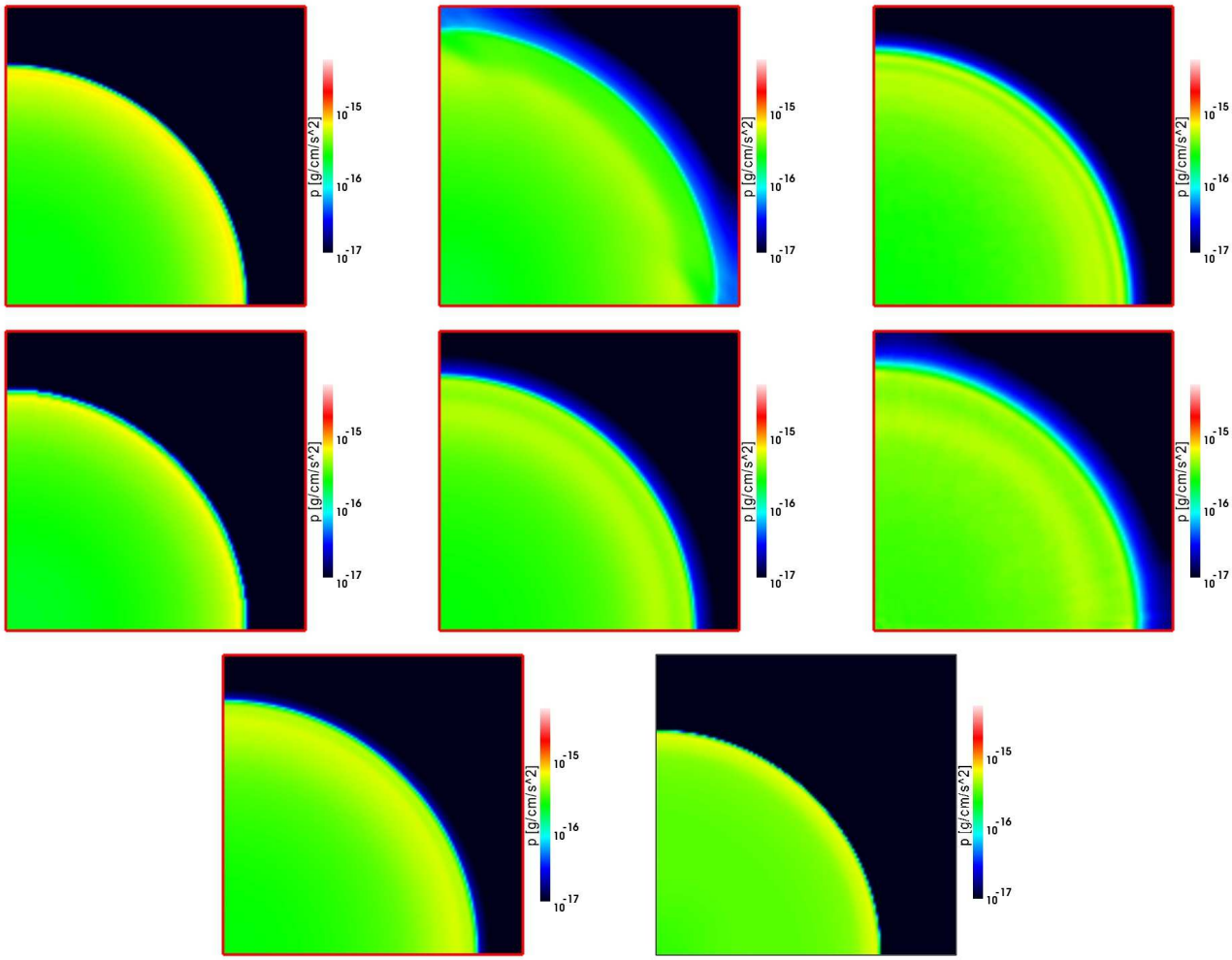

Figure 6. Test 5 (H II region expansion in an initially-uniform gas): Images of the pressure, cut through the simulation volume at coordinate $z = 0$ at time $t = 500$ Myr for (left to right and top to bottom) Capreole+C^2-Ray, HART, RSPH, ZEUS-MP, RH1D, LICORICE, Flash-HC and Enzo-RT.

into the ionized cloud forming a shock that moves with a roughly constant velocity in r^{-2} density profiles (Franco et al. 1990).

In Test 6 we examine the former case, in which the initial Strömgren radius is smaller than the core radius. The aim of this test is to study the initial transition of the I-front from R-type to D-type and back to R-type over a fairly restricted range of radii, rather than its long-term behavior thereafter. Accordingly, we adopt the following numerical parameters: computational box length $L = 0.8$ kpc, $n_0 = 3.2$ cm^{-3}, $r_0 = 91.5$ pc, zero initial ionization fraction, ionizing photon emission rate $\dot{N}_\gamma = 10^{50}$ photons s^{-1} and initial temperature $T = 100$ K. The source position is at the corner of the computational volume $(x_s, y_s, z_s) = (0, 0, 0)$. Boundary conditions are reflective for the boundaries which contain the origin and transmissive for the other boundaries. For these parameters the I-front changes from R-type to D-type inside the core. Once the front reaches the core edge it will accelerate as it propagates down the steep density slope. The initial recombination time inside the core (assuming ionized gas temperature $T = 10^4$ K) is $t_{\rm rec,core} = 0.04$ Myr. The ionizing spectrum is again that of a 10^5 K black body, as expected for a massive, metal-free Pop III star. Hydrogen line cooling, recombinational cooling, and bremsstrahlung cooling are all included, but again not Compton cooling. For simplicity, gravitational forces are ignored and no hydrostatic equilibrium is imposed on the cloud. Unlike in Test 5, left on their own the pressure forces will accelerate gas outward in this density-stratified cloud, albeit those forces are much inferior than the stronger ones due to pressure from the photoheated gas. The running time is $t_{\rm sim} = 75$ Myr. The required outputs are neutral fraction of hydrogen, gas number density, temperature and Mach number on the grid at times $t = 1, 3, 10, 25$ and 75 Myr, and the I-front position (as defined in Test 5) and velocity vs. time along the x-axis.

3.3 Test 7: Photoevaporation of a dense clump

In Test 7, a plane-parallel I-front encounters a uniform spherical clump in a constant background density field. This problem has been studied in many contexts, *e.g.* in relation to the photoevaporation of dense clumps in planetary nebulae (Mellema et al. 1998). Depending on the assumed parameters the clump may either initially trap the I-front, or be flash-ionized without ever trapping the I-front, the so-called 'cloud-zapping' regime (c.f. Bertoldi 1989). The condition for an I-front to be trapped by a dense clump with number density n_H can be derived by defining a "Strömgren length", $\ell_S(r)$, at a given impact parameter r using equations (6) and (7), and solving them for each impact parameter (Shapiro et al.

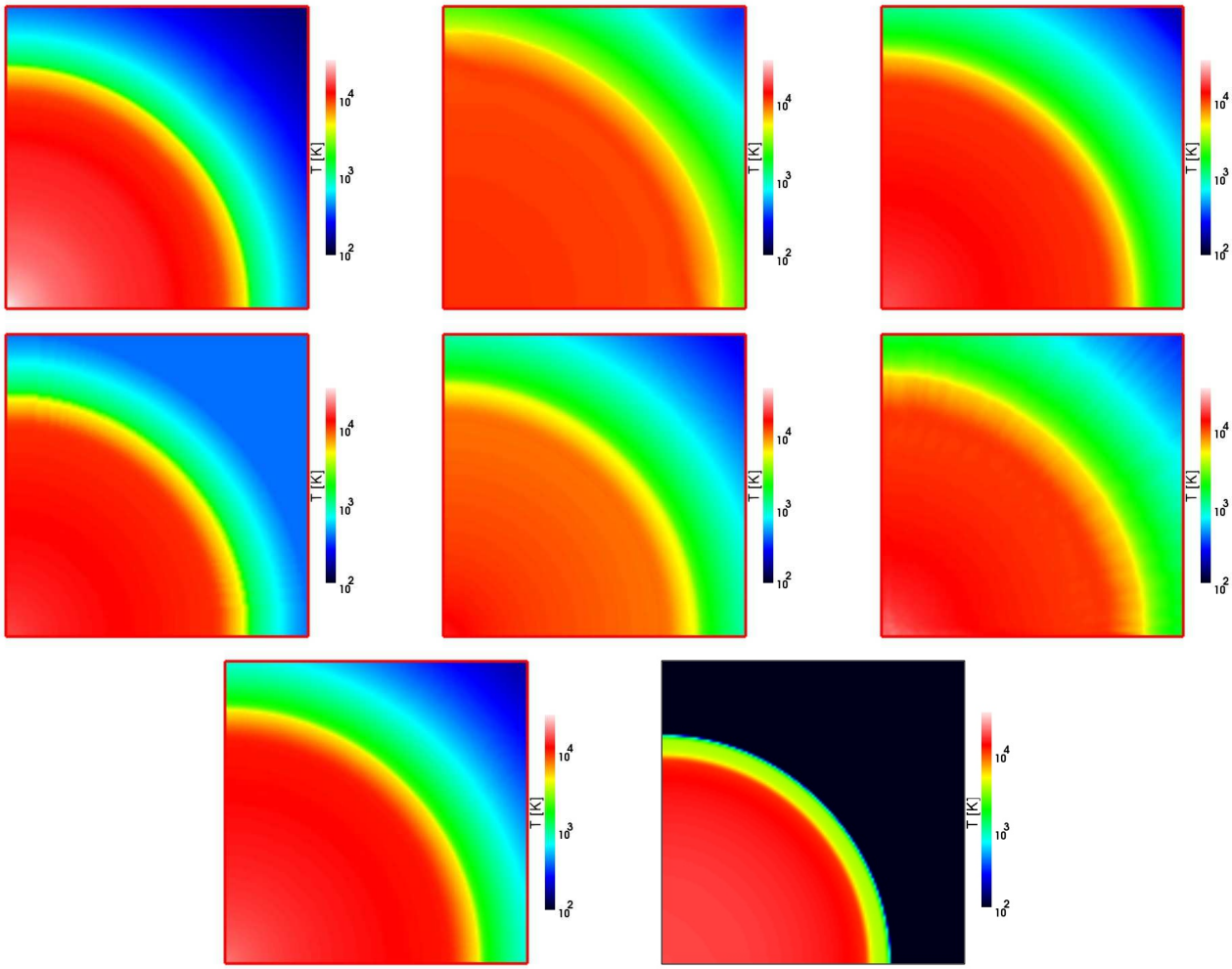

Figure 7. Test 5 (H II region expansion in an initially-uniform gas): Images of the temperature, cut through the simulation volume at coordinate $z = 0$ at time $t = 500$ Myr for (left to right and top to bottom) Capreole+C^2-Ray, HART, RSPH, ZEUS-MP, RH1D, LICORICE, Flash-HC and Enzo-RT.

2004). We can then define the "Strömgren number" for the clump as $L_S \equiv 2r_{\rm clump}/\ell_S(0)$, where $r_{\rm clump}$ is the clump radius and $\ell_S(0)$ is the Strömgren length for zero impact parameter. If $L_S > 1$, then the clump is able to trap the I-front, while if $L_S < 1$, the I-front quickly ionizes the clump and is never trapped. For a uniform clump equation (8) reduces to

$$\ell_S = \frac{F}{\alpha_H^{(2)} n_H^2}, \tag{13}$$

and L_S becomes

$$L_S = \frac{2r_{\rm clump}\alpha_H^{(2)} n_H^2}{F}. \tag{14}$$

The numerical parameters for Test 7 are the same as for Test 3 in Paper I: a constant ionizing photon flux of $F = 10^6\,{\rm s}^{-1}{\rm cm}^{-2}$ is incident at $y = 0$, the ambient hydrogen gas number density and temperature are $n_{\rm out} = 2 \times 10^{-4}\,{\rm cm}^{-3}$ and $T_{\rm out} = 8,000$ K, respectively, while the initial clump density and temperature are $n_{\rm clump} = 200\,n_{\rm out} = 0.04\,{\rm cm}^{-3}$ and $T_{\rm clump} = 40$ K. These parameters ensure that outward pressures in the clump balance those from the hot gas so that the clump is initially in pressure equilibrium with the surrounding medium. The column density of the clump is sufficient to trap the I-front and compel its transition to D-type, in contrast to the less interesting for us "cloud-zapping" regime in which the front flash-ionizes the cloud and remains R-type throughout. The computational box size is $x_{\rm box} = 6.6$ kpc, the radius of the clump is $r_{\rm clump} = 0.8$ kpc, and its center is at $(x_c, y_c, z_c) = (5, 3.3, 3.3)$ kpc = $(97, 64, 64)$ cells. Hydrogen line cooling, recombinational cooling, and bremsstrahlung cooling are included, but not Compton cooling. Boundary conditions are transmissive for all grid boundaries.

With hydrodynamics the evolution beyond the trapping phase proceeds very differently from the static Test 3 in Paper I. As the heated and ionized gas is evaporated and expands towards the source, its recombination rate falls and it attenuates the ionizing flux less. As a consequence, the I-front slowly consumes the clump until it photoevaporates completely. The required outputs are H I fraction, gas pressure, temperature, and Mach number at times $t = 1, 5, 10, 25$ and 50 Myr and the position and velocity of the I-front along the axis of symmetry.

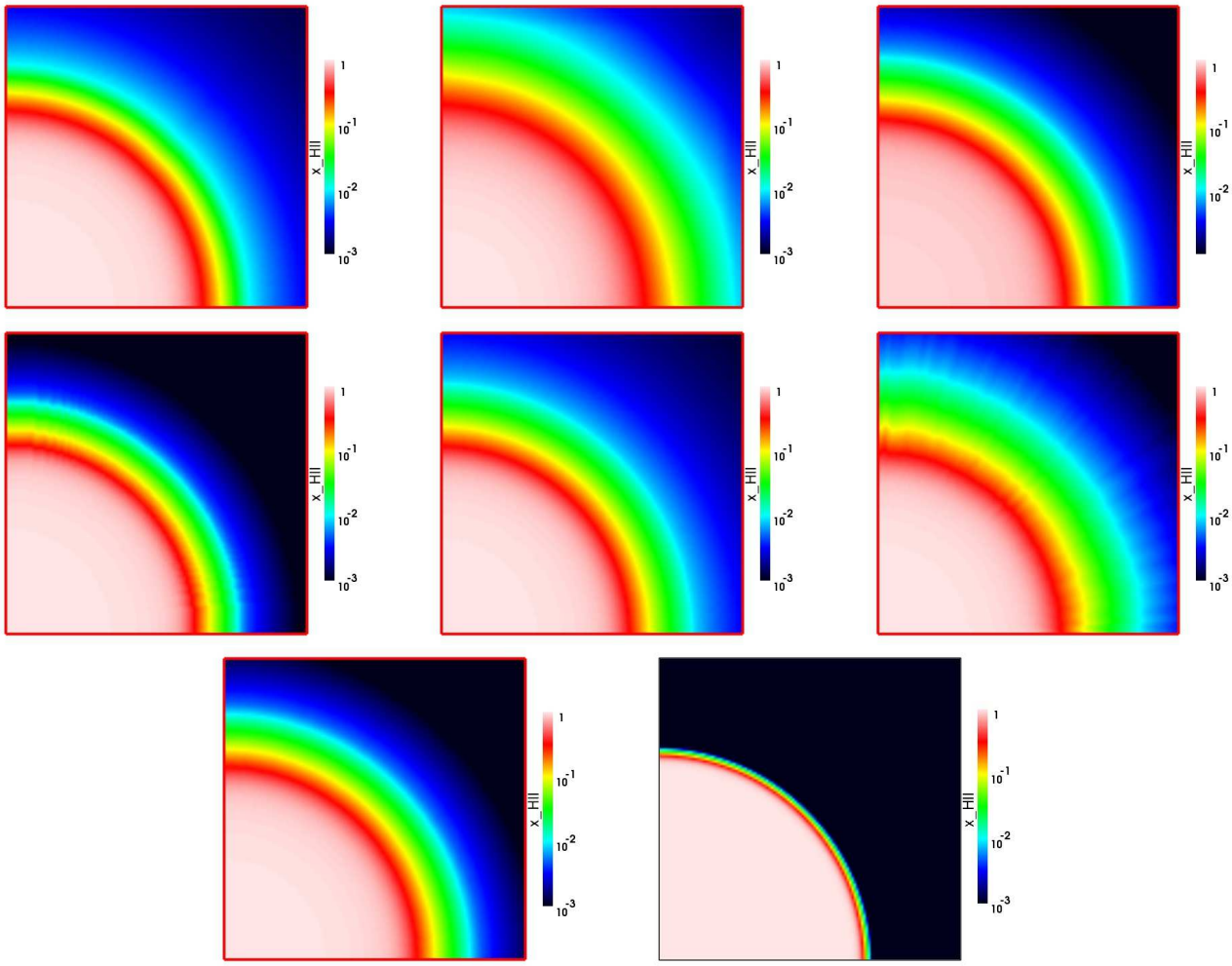

Figure 8. Test 5 (H II region expansion in an initially-uniform gas): Images of the H II fraction, cut through the simulation volume at coordinate $z = 0$ at time $t = 500$ Myr for (left to right and top to bottom) Capreole+C^2-Ray, HART, RSPH, ZEUS-MP, RH1D, LICORICE, Flash-HC and Enzo-RT.

4 RESULTS

4.1 Test 5

We start by comparing the fluid flow and ionization structure at two characteristic stages of the evolution, at $t = 100$ Myr, of order of one recombination time, which is the start of the I-front conversion from R- to D-type, shortly before the initial Strömgren radius is reached, and at $t = 500$ Myr, corresponding to a few recombination times, when the I-front is D-type preceded by a shock. In Figures 2 - 4 and 5 - 7 we show image cuts at coordinate $z = 0$ of the neutral hydrogen fraction, pressure, and temperature at 100 Myr and at 500 Myr, respectively, while in Figures 8 and 9 we show the ionized fraction and number density at 500 Myr. We note here that unlike the other simulations which are fully 3-D in both the hydrodynamic and the radiative transfer treatment, the RH1D results are 1-D spherically-symmetric Lagrangian profiles mapped onto the 3-D Cartesian grid required in this study.

With a few exceptions, discussed below, all results exhibit reasonably good agreement throughout the flow evolution. As we found also for the static tests in Paper I, the majority of the differences are a consequence of the different handling of the energy equation and the hard photons with long mean free paths. These variations yield different spatial structures in the temperatures (Figures 4, 7 and 13) and ionized fractions in the gas just ahead of the I-front (which are dictated by the hard photons and non-equilibrium chemistry, Figures 8 and 11), but very similar ionization profiles inside the H II region (which sees the whole spectrum of photons and is mostly chemically equilibrated, Figures 2, 5 and 11).

Regardless of the variations in the temperature and ionization profiles among the codes, the overall differences in I-front position and velocity are very modest, of order only a few percent, with the exception of Enzo-RT and, to a lesser extent, HART. The hydrodynamical profiles also cluster fairly closely together. The codes basically agree on the temperature structure of the evolving H II region over time except for HART, which predicts flat, lower temperatures at later times, and C^2-Ray, which yields higher ionized gas temperatures close to the ionizing source due to its simplified method for handling the energy, and again Enzo-RT because of its monochromatic spectrum. The reason for the sharp drop in pressure at 0.6 L_{box} at 10 Myr in the HART results is unclear.

Apart from the differences discussed above, there are several features of the HART, LICORICE and Enzo-RT methods worth noting. The OTVET moment radiative transfer method used in HART is somewhat diffusive, as was already noted in Paper I, which results in thicker I-front and less sharp flow features overall. There are some radial striations visible in the LICORICE re-

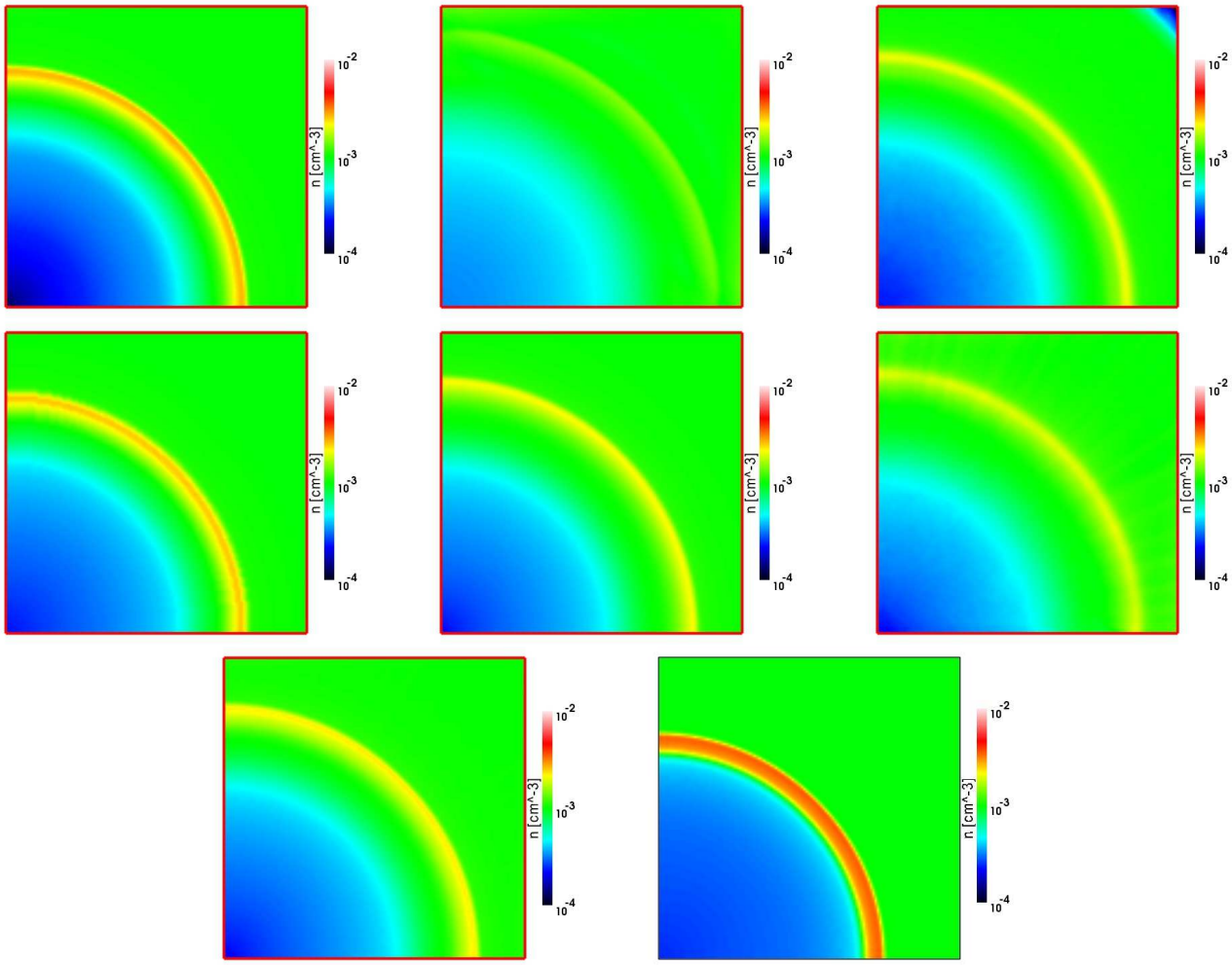

Figure 9. Test 5 (H II region expansion in an initially-uniform gas): Images of the gas number density, cut through the simulation volume at coordinate $z = 0$ at time $t = 500$ Myr for (left to right and top to bottom) Capreole+C^2-Ray, HART, RSPH, ZEUS-MP, RH1D, LICORICE, Flash-HC and Enzo-RT.

sults, especially in the temperature images that are reminiscent of those observed in the CRASH code results in Test 2 of Paper I. Since LICORICE adopts the Monte Carlo radiative transfer found in the original version of CRASH, the radial artifacts in its temperatures are similarly due to the noise in that version's energy sampling scheme, which has been corrected in the latest release of the CRASH code (Maselli et al. 2009). The wall effects in the upper left and lower right corners of the box in the HART pressure and Mach number images reflect the fact that mirror rather that transmissive boundary conditions were utilized. This is due to the natively-periodic nature of the OTVET method, which demands special handling in order to run the non-periodic test problems in this comparison. The LICORICE, and to a lesser extent the RSPH Mach numbers exhibit a somewhat grainy structure deep inside the H II region not visible in the other quantities. The origin of these features is likely due to the low SPH resolution in the evacuated interior of the H II region, which is nearly an order of magnitude lower in density than its surroundings. The difference in the degree of graininess between the two SPH codes may in part be due to how each code's particle data was mapped onto the Cartesian grid. The origin of the third outermost band in the RSPH Mach numbers, which is not present in those of the other codes, is likely due to the utilization of a larger box in that calculation compared to the other cases, which changes the flow boundary conditions.

Several important questions arise in this Test. First, does the broadening of the front by high-energy photons from a hard UV source alter its radius as a function of time in comparison to a monochromatic front with the same average ionized gas temperatures? This issue is key because it determines if the extensive approximate analytical solutions to hydrodynamical I-front transport that exist in the literature apply to ionization fronts in which there is spectral hardening due to hard UV sources. Second, how does the penetration of hard photons into the dense shocked neutral gas ahead of the I-front alter its structure and flow? Third, how do these changes to the shocked flow alter its own rate of advance and that of the front? Finally, what are the origin of the distinctive double peaks in density, velocity and Mach number in the full spectrum I-fronts at intermediate times, and why are they absent in the Enzo profiles?

We cannot resort to comparison of the present code results alone to resolve these questions because they are all are multifrequency in nature except for Enzo, and even Enzo integrates over the blackbody spectrum to implement the grey approximation to radiation transport. These issues can only be settled by comparing the multifrequency I-front in Test 5 to a monochromatic one whose

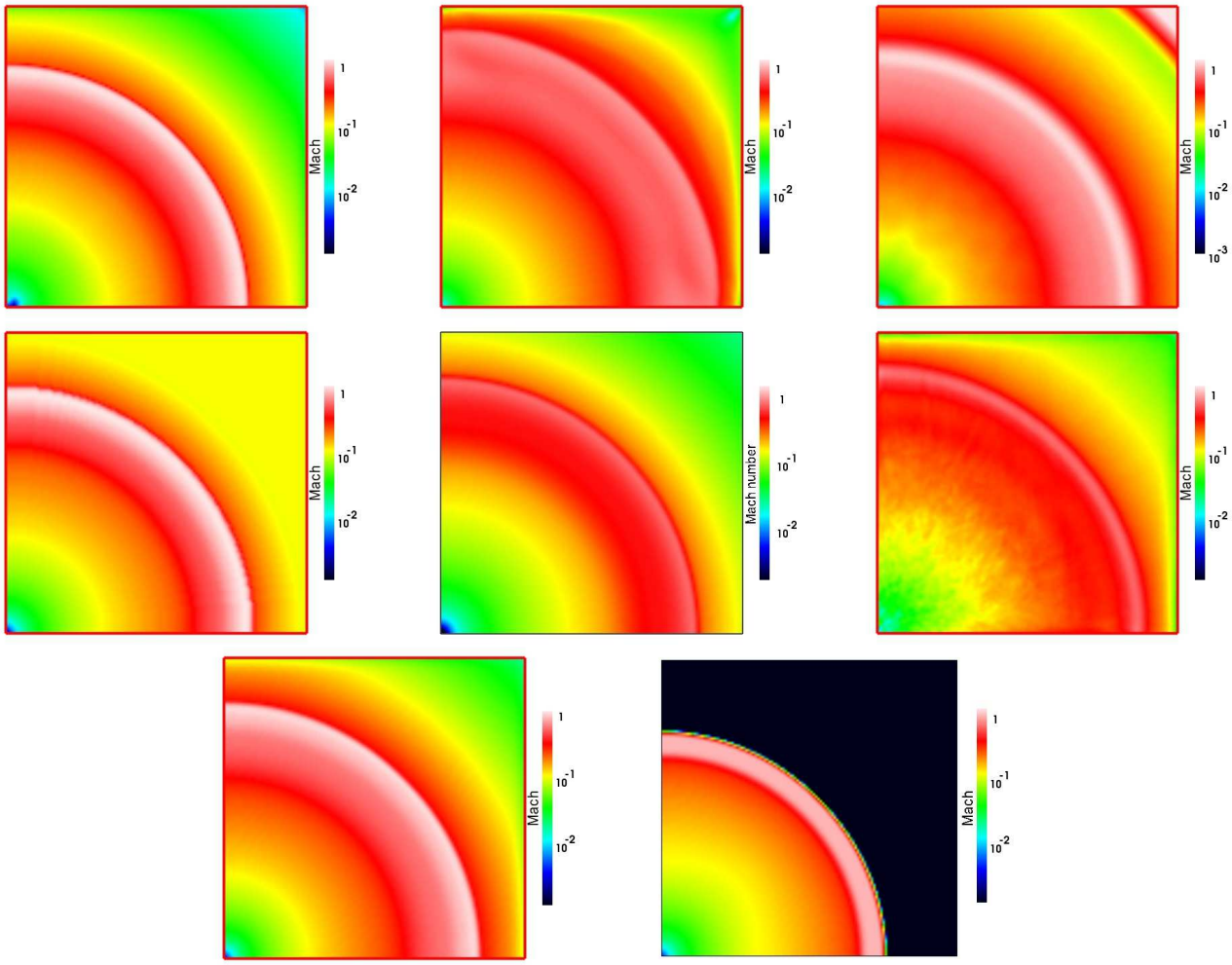

Figure 10. Test 5 (H II region expansion in an initially-uniform gas): Images of the Mach number, cut through the simulation volume at coordinate $z = 0$ at time $t = 500$ Myr for (left to right and top to bottom) Capreole+C^2-Ray, HART, RSPH, ZEUS-MP, RH1D, LICORICE, Flash-HC and Enzo-RT.

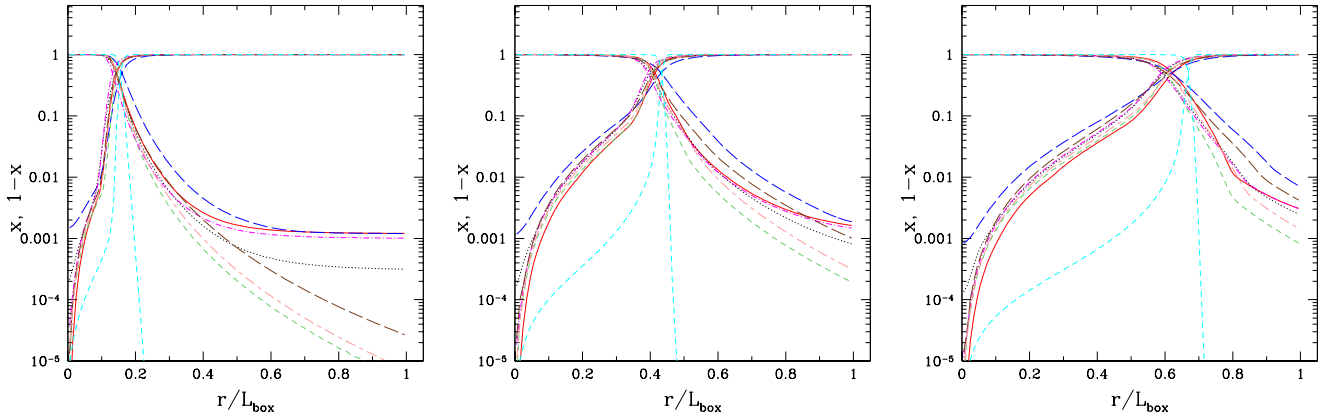

Figure 11. Test 5 (H II region expansion in an initially-uniform gas): Spherically-averaged profiles for ionized fractions x and neutral fractions $x_{\rm HI} = 1 - x$ at times $t = 10$ Myr, 200 Myr and 500 Myr vs. dimensionless radius (in units of the box size).

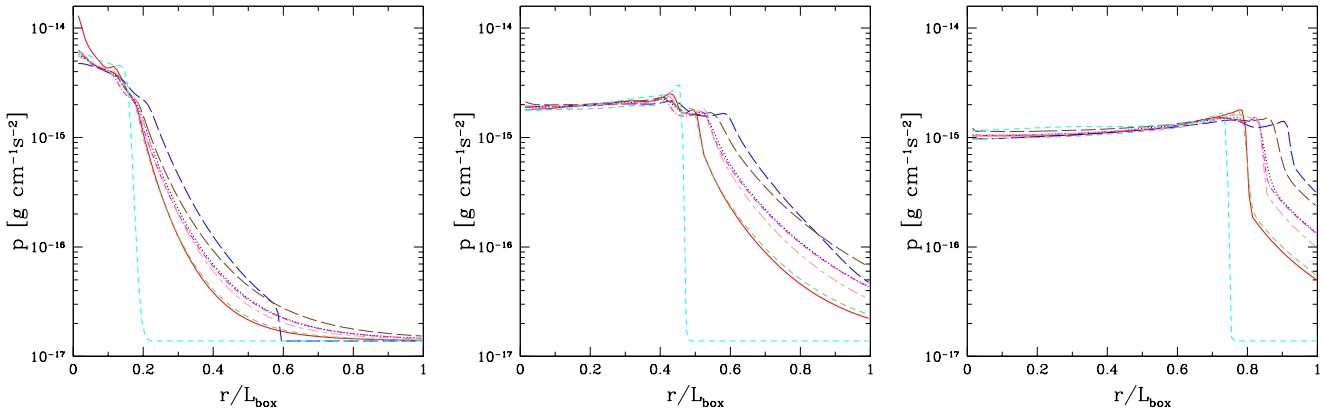

Figure 12. Test 5 (H II region expansion in an initially-uniform gas): Spherically-averaged profiles for pressure, p, at times $t = 10$ Myr, 200 Myr and 500 Myr vs. dimensionless radius (in units of the box size).

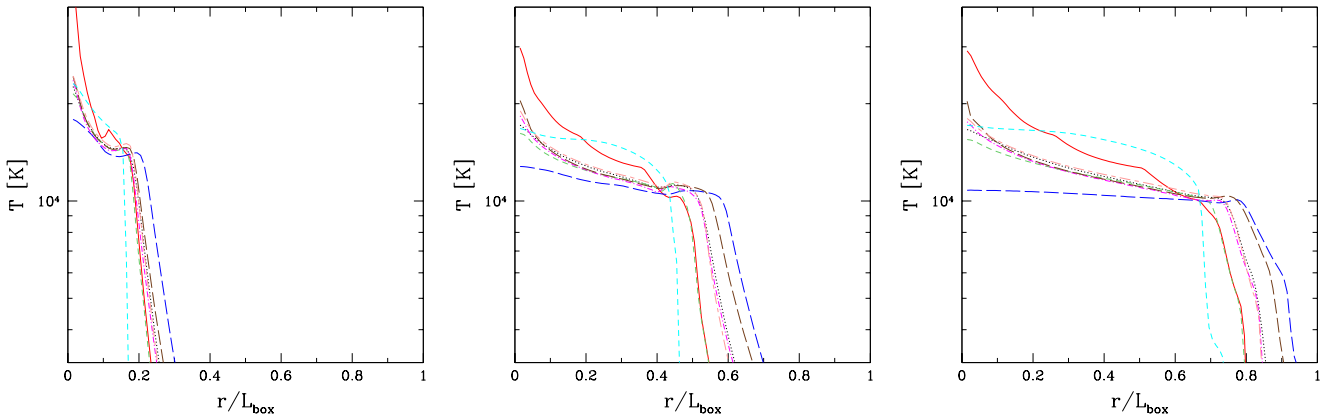

Figure 13. Test 5 (H II region expansion in an initially-uniform gas): Spherically-averaged profiles for temperature at times $t = 10$ Myr, 200 Myr and 500 Myr vs. dimensionless radius (in units of the box size).

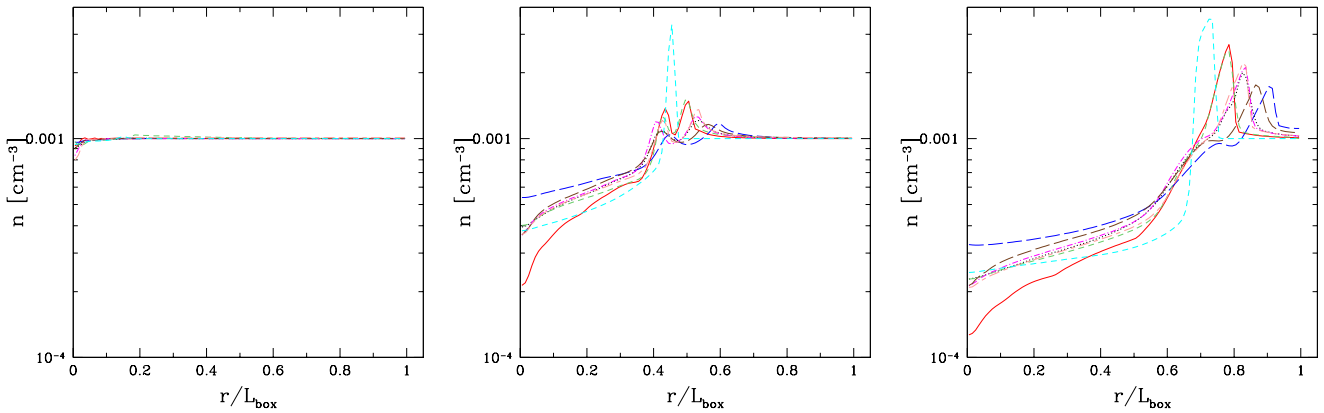

Figure 14. Test 5 (H II region expansion in an initially-uniform gas): Spherically-averaged profiles for the hydrogen number density, n, at times $t = 10$ Myr, 200 Myr and 500 Myr vs. dimensionless radius (in units of the box size).

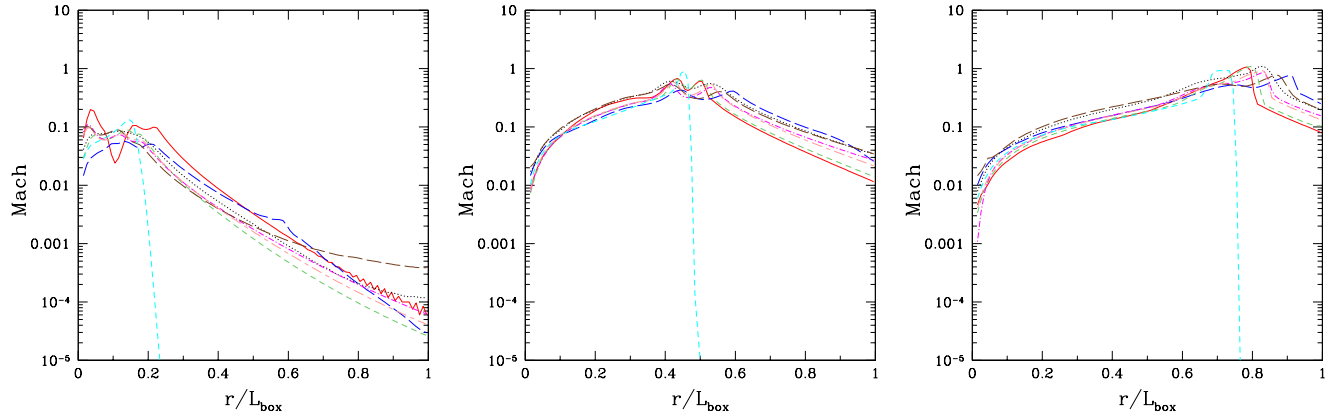

Figure 15. Test 5 (H II region expansion in an initially-uniform gas): Spherically-averaged profiles for the flow Mach number, M, at times $t = 10$ Myr, 200 Myr and 500 Myr vs. dimensionless radius (in units of the box size).

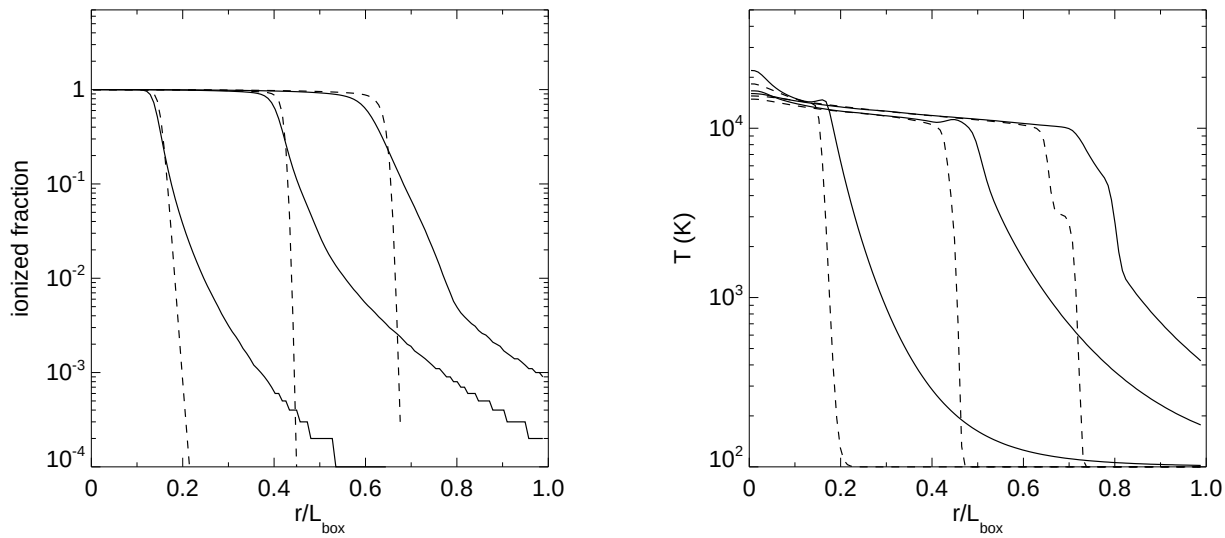

Figure 16. ZEUS-MP Test 5 ionized fraction (left) and temperature (right) profiles with monoenergetic photons (dashed) and a 10^5 K blackbody spectrum (solid) at times $t = 10$ Myr (left pairs), 200 Myr (central pairs) and 500 Myr (right pairs) vs. dimensionless radius (in units of the box size).

photon energy has been adjusted to yield the same average ionized gas temperature as for the 10^5 K blackbody spectrum. This guarantees that any discrepancy in position between the two fronts will be due only to the broadening of the front and its modifications to the shocked flow just beyond it, not to differences in the average sound speed within the H II regions, which is primarily what determines the rate of advance of the I-front when it is D-type. This approach also ensures that any variations in the structure of the shocked flow between the two I-fronts are due to spectral hardening only, since both are being driven by the same ionized gas pressure.

To investigate these points and determine the origin of some of the features in the hydrodynamic profiles in Figures 11 -15, we performed two fiducial runs of Test 5 with ZEUS-MP. The first was with the original 10^5 K blackbody spectrum and the second was with monoenergetic photons at 17.0 eV. Both had the same ionizing photon rate $\dot{N}_\gamma = 5 \times 10^{48}\ \mathrm{s}^{-1}$. The 17.0 eV monochromatic photons establish the same average ionized gas temperature as in the multifrequency H II region in ZEUS-MP. We show ionized fractions, temperatures, velocities, and densities for the two runs at t =10, 200, and 500 Myr in Figures 16 and 17. The broadening of the I-front in the multifrequency calculation is apparent at all three times in the ionized fractions, becoming greater as the front expands. In contrast, the monoenergetic I-front remains sharp, intersecting the multifrequency front at very nearly the same ionized fraction at all three radii. Except for small differences in the elevated values near the source, the two H II regions exhibit nearly identical temperatures out to where the full-spectrum I-front broadens. Out to this same radius the density and velocity profiles are also nearly identical.

The ionization profiles demonstrate that the position of the I-front as a function of time is not signficantly altered by either the broadening of the front or the partial ionization and heating of the

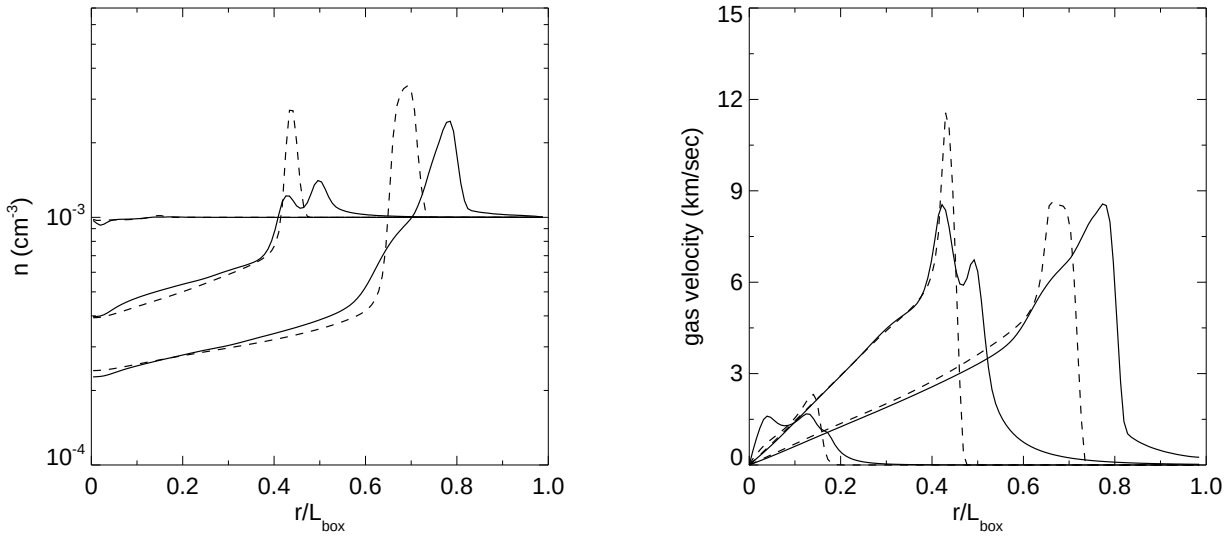

Figure 17. ZEUS-MP Test 5 density (left) and gas velocity (right) profiles with monoenergetic photons (dashed) and a 10^5 K blackbody spectrum (solid) at times $t = 10$ Myr (left pairs), 200 Myr (central pairs) and 500 Myr (right pairs) vs. dimensionless radius (in units of the box size).

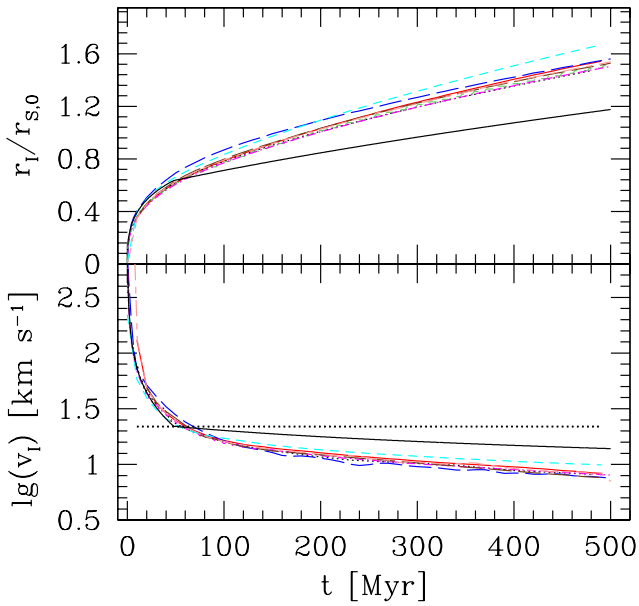

Figure 18. Test 5 (H II region gasdynamic expansion in an initially-uniform gas): The evolution of the position and velocity of the I-front. Solid lines show the approximate analytical solution as described in the text. Dotted horizontal line indicates the approximate value of v_R.

dense shocked gas in front of it by high-energy photons, at least for the radii considered in this problem. This affirms that the global dynamics of the D-type I-front depend primarily on the temperature (and hence sound speed) of the ionized gas. Past tests by one of us of D-type I-fronts in r^{-2} density gradients confirm that this holds well beyond the R to D transition surveyed in this Test. Likewise, these two models demonstrate that the ionized flow within the H II region is also mostly unchanged by spectral hardening over the radii enclosed by the computational box. However, here it is important to distinguish between the motion of the I-front and that of the shocked flow it drives. The latter is dramatically altered by spectral hardening as we discuss below.

The simple-structured 3000 K layer of shocked gas driven by the monochromatic I-front is split into the double-peaked structure in the full-spectrum front at $t = 200$ Myr and is present in the profiles of all the codes except Enzo, as shown in Figures 14 and 15. This feature is transient and disappears by $t = 500$ Myr. Its origin is the heating of the dense shell by the high-frequency photons. At 200 Myr, they partially ionize the base of the shocked shell: ionized fractions of 10% or more extend out to 0.5 L_{box}. The high frequency tail of the spectrum cannot maintain large ionized fractions in this layer but does effectively deposit heat there, as evidenced by the rise in temperature at 0.45 L_{box}, which is positioned approximately in the valley between the two peaks in the density and velocity profiles. This energy ablates the lower layer of the dense shocked shell, driving both inward and outward photoevaporative flows in the frame of the shock that split the density and velocity peaks into two smaller ones. The forward flow accelerates the gas in the outer peak to 7 km s^{-1} by 200 Myr. However, pressure gradients from the ionized interior of the H II region drive the inner peak to higher velocities that cause it to later overtake the forward peak (500 Myr). At this distance from the central source, high energy photons do heat the base of the shocked shell but not to sufficient temperatures to create backflow, as seen in the disappearance of the temperature bump that was present at 200 Myr. However, they do smear out the sharp interface between the ionized and shocked gas temperatures that is present in the monoenergetic front at 500 Myr. In contrast, monoenergetic photons result in much simpler structure in both the front and the dense shell at 200 and 500 Myr. At 500 Myr, ∼15,000 K ionized gas drives a clearly defined shocked shell and there are no ablation flows. The absence of backflows allow

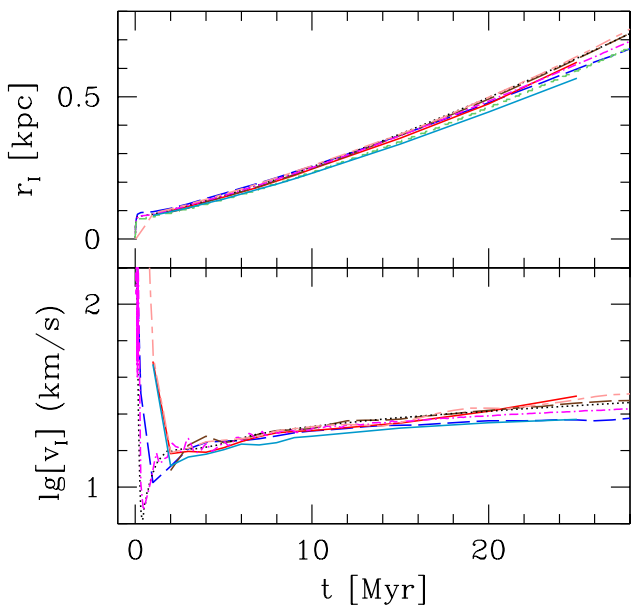

Figure 19. Test 6 (H II region gasdynamic expansion down a power-law initial density profile): The evolution of the position and velocity of the I-front.

peak gas velocities to reach higher values in the shell at intermediate times than in the hard spectrum case.

What effect does pre-heating by hard photons leaking ahead of the I-front have on the propagation of the shocked flow? It weakens the shock, as evidenced by the smaller density jump, lowering the density compression there and thus enlarging its detachment from the I-front. This can be clearly seen by comparing the position of the shock for the two I-fronts in Figure 17. Thus, while the positions of the two fronts are nearly identical, the shocked flow of the multifrequency front is well ahead of that of the monochromatic one. It is clear from this comparison that multifrequency photon transport, or the use of lookup tables of ionizing rates as a function of optical depth as a proxy, is necessary to capture the correct structure of I-fronts and shocks driven by high-temperature UV sources.

Having isolated the effect of spectral hardening on both the dynamics of the I-front and on the shocked neutral flows it drives, we can now disentangle the sometimes competing effects that account for the differences that do exist among the hydrodynamic profiles in Test 5, both among the codes with multifrequency physics and between those codes and Enzo. Setting aside the Enzo results for the moment, the minor spread in I-front position in the other codes can now be traced to the variations of their H II region temperatures. This is primarily due to how each code handles the energy equation. Furthermore, it is now clear that (1) the origin of the temperature bumps in the shocked gas at intermediate times; (2) the double peaks in the densities, velocities, and Mach numbers; and (3) shocks that are more fully detached from the I-front are all a consequence of spectral hardening.

The profiles that are most distinct from the rest are those of Enzo-RT. This can now be understood to be due to the lack of spectral hardening in this code. Although it carries out an integration over the 10^5 K spectrum to compute the photoionization cross sections, Enzo-RT it employs a grey approximation for the photoionization cross-section, i.e. a cross-section independent of the frequency and is therefore essentially monochromatic in its current form. No hard photons means no pre-heating ahead of the front and also a much sharper I-front. This lack of pre-heating in turn means that, as in the ZEUS-MP monochromatic results above, the Enzo-RT shock is stronger than the others, as evidenced by its higher Mach number, density compression and pressure jump. Because the Enzo I-front remains sharp, its shocked flow also exhibits the single peak associated with monoenergetic I-fronts. Because it is stronger, the shock in the Enzo profiles propagates somewhat more slowly, lagging behind those of the other codes. On the other hand, the Enzo-RT I-front actually leads the others, almost coinciding with the shock. This is a consequence of the greater average ionized gas temperatures in its H II region in comparison to the others, a result of its integration over the blackbody spectrum. The Enzo-RT temperature profile is similar to the flat profile found by HART, but at a higher value. Its origin is unknown but could be associated with its flux-limited diffusion radiative transfer, which shares some similarities with the OTVET method in HART.

Except for the variations noted above, the codes agree well on I-front position and velocity but are at variance with the analytical solution, leading it by roughly 30%. This is in part because the solution plotted in Figure 17 is for fixed temperatures of 15,000 K behind and 1000 K ahead of the I-front (allowing for some pre-heating by hard photons, which alters the values of v_R and v_D), while in reality the profiles exhibit a complex temperature structure. Furthermore, as we discussed above, the analytical solution describes well the early and late evolution, but not the intermediate one. The H II region radial evolution at late times does not exactly match the asymptotic $t^{4/7}$ slope predicted for self-similar flows but approaches it at larger radii. This is to be expected since the box size was chosen to enclose only the transition of the I-front from R-type to D-type, during which the assumption of self-similarity is not satisfied. The codes asymptotically approach the expected solution as the fronts grow in radius.

Finally, we note that the I-fronts in this test are dynamically stable. If H_2 cooling, LW photodissociation, and self-shielding to LW photons had been included, violent hydrodynamical instabilities mediated by H_2 cooling might have erupted in the fronts after becoming D-type, as explained in greater detail in Test 6 below. Line cooling in H alone appears to be unable to incite such instabilities (Whalen & Norman 2008b).

4.2 Test 6

We start our analysis with a head-to-head comparison of the evolution of the position and velocity of the I-front, plotted in Figure 19. In the velocity plot we clearly see the evolution stages outlined in the discussion of Test 6 above. Initially, while it is still within the density core the I-front moves very fast (is of R-type), but precipitously slows down as it approaches its Strömgren radius (whose precise value is temperature-dependent, but is slightly smaller than the core radius chosen here). The fast R-type phase is over within a fraction of a Myr, after which the expansion becomes pressure-driven, and the front itself converts to a D-type led by a shock. The I-front speed reaches a minimum of just a few kilometers per second, well below v_R - the critical velocity defined in § 3.1. We note that although some of the results appear to never show I-front velocities below $\sim$ 10 km/s, this is in fact due to insufficient number of early-time snapshots being saved in the I-front evolution data. For this reason the short transition stage does not appear in some of the plotted results, and this does not imply any problem with the codes. The later-time evolution is not affected, as long as the ac-

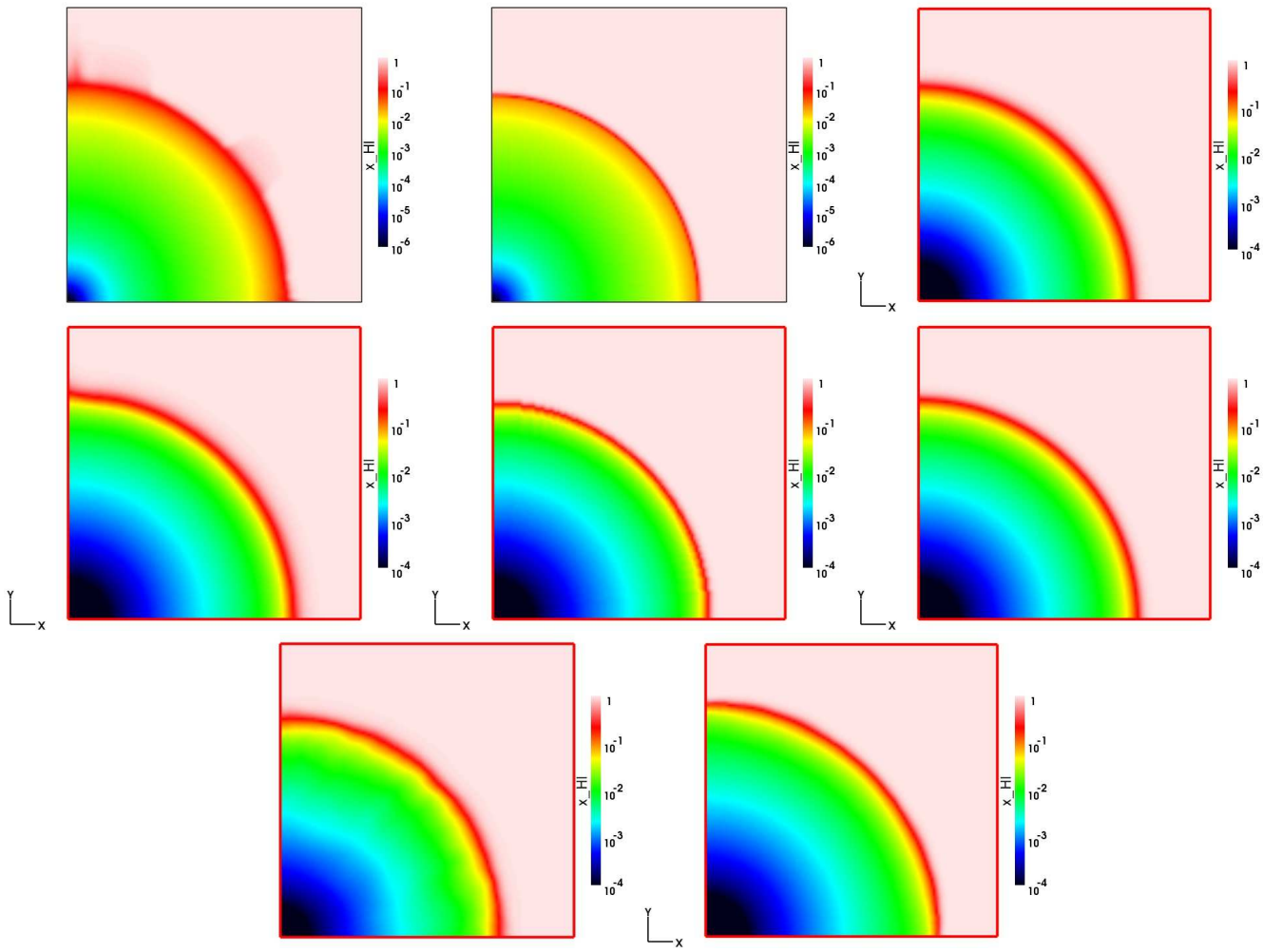

Figure 20. Test 6 (H II region gasdynamic expansion down a power-law initial density profile): Images of the H I fraction, cut through the simulation volume at coordinate $z = 0$ at time $t = 25$ Myr for (left to right and top to bottom) Capreole+C^2-Ray, TVD+C^2-Ray, HART, RSPH, ZEUS-MP, RH1D, LICORICE, and Flash-HC.

tual time-stepping in the code is sufficiently fine to properly follow the early evolution. Once out of the core, the I-front re-accelerates as it descends the steep r^{-2} density gradient, eventually reaching speeds of $25 - 28$ km/s. These speeds never surpass v_R and therefore the front remains D-type until leaving the computational volume at $t \sim 30$ Myr

All codes agree on the later-time, pressure-driven expansion, both qualitatively (a slow, D-type I-front, preceded by a relatively weak shock, as we shall see below), and quantitatively. There are some modest differences in the I-front speed, $\sim$ 10% or less between cases, which results in I-front positions whose spread grows with time, but never exceeds $\sim 5 - 7\%$.

Next we turn our attention to the overall structure of the fluid flow and ionization, shown in 2-D cuts along the x-y plane of the H I and H II fractions, density, temperature and Mach number at time $t = 25$ Myr in Figures 20 - 24. We again remind the reader that unlike the other simulations which are fully 3-D in both the hydrodynamic and the radiative transfer treatment, the RH1D results are 1-D spherically-symmetric Lagrangian profiles mapped onto the 3-D Cartesian grid required in this study. There is good agreement between the results, in terms of the positions of the I-front and the shock, the size of the growing H II region and its ionization, density and temperature structures. There are some differences in the level of hard photon penetration ahead of the I-front and the temperature distribution, similar to the ones we observed in Test 5 and Paper I.

However, in this test also a new kind of difference shows up, namely the appearance of instabilities near the I-front. Such instabilities occur for several of the codes, and their nature varies between codes. In the cases of C^2-Ray+Capreole and LICORICE, the instabilities are clearly visible in the ionized fractions, temperatures, densities, and Mach numbers, while in Flash-HC they are mostly visible in the temperatures and ionized fractions. RSPH exhibits a minor anomaly in only the temperature at 25 Myr. The RH1D data cannot exhibit such instabilities because they are 1D spherical polar coordinate profiles mapped onto the 3D Cartesian grid mandated for this test. The ZEUS-MP profiles, which were computed on a 3D spherical polar coordinate grid and then mapped onto 3D Cartesian coordinates, manifest no instabilities in any of the profiles, and the HART results do not show them either. Are these instabilities physical or numerical?

Three types of dynamical instabilities in ionization fronts have been discovered in the past thirty years. The first type occurs in D-type ionization fronts whose shocked neutral gas shells can cool efficiently by radiation (Giuliani 1979; Garcia-Segura & Franco

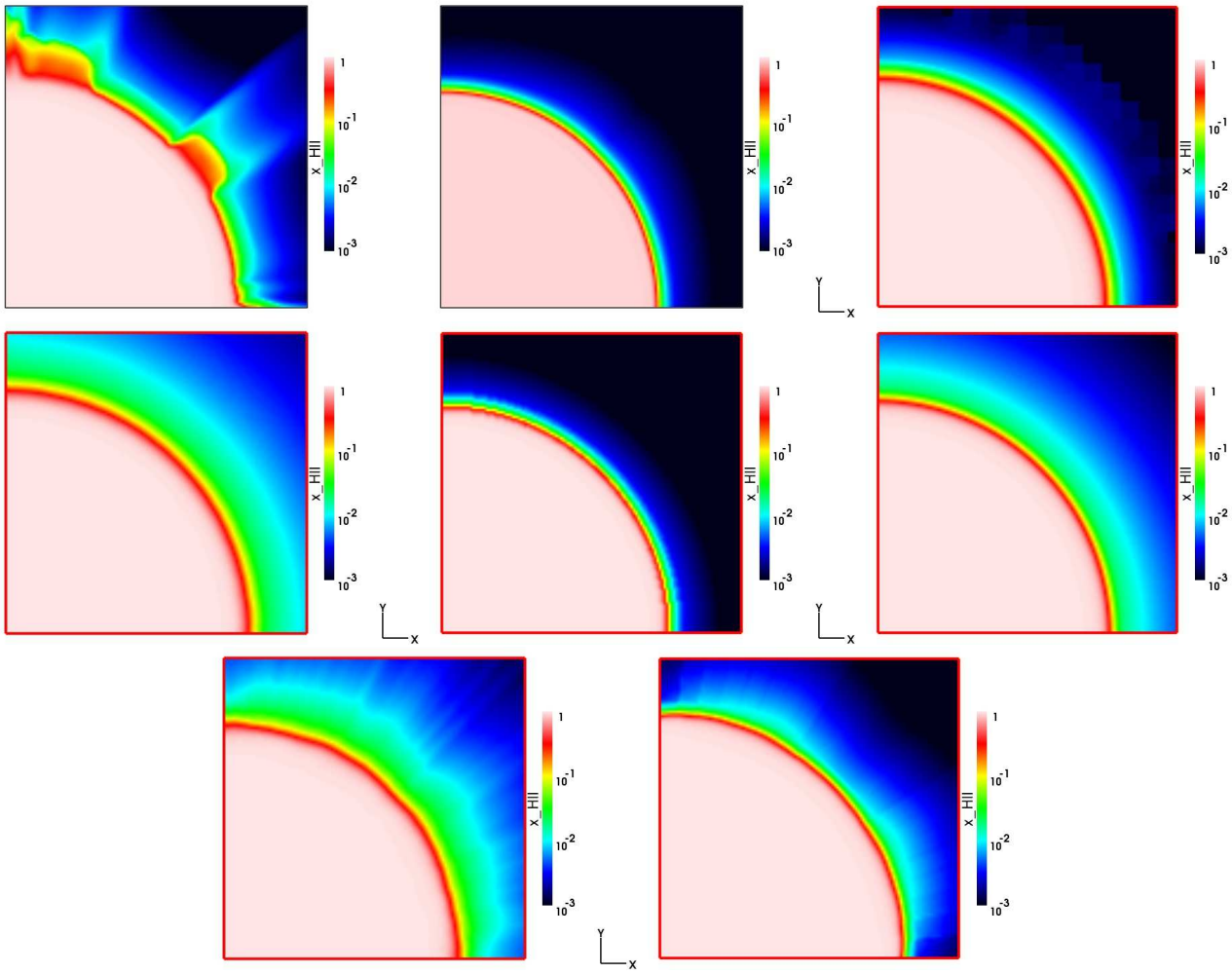

Figure 21. Test 6 (H II region gasdynamic expansion down a power-law initial density profile): Images of the H II fraction, cut through the simulation volume at coordinate $z = 0$ at time $t = 25$ Myr for (left to right) and top to bottom) Capreole+C^2-Ray, TVD+C^2-Ray, HART, RSPH, ZEUS-MP, RH1D, LICORICE, and Flash-HC.

1996). Cooling collapses the gas into a cold thin dense layer that is prone to oscillations and fragmentation (Vishniac 1983). Ionizing UV radiation then opportunistically escapes through the cracks in the shell and flares outward in violent instabilities. However, in the current Test only H lines can cool the shell, and recent numerical experiments prove that such cooling is too inefficient to initiate dynamical instabilities of this type (Whalen & Norman 2008a). The fact that thin-shell instabilities do not arise in the Test 5 profiles further attests to the fact that H line cooling is not responsible for the corrugations in the Test 6 profiles. In general, shocks that accelerate down power law density gradients steeper than r^{-2} are also prone to Rayleigh-Taylor instabilities that do not require radiative cooling. They too are also capable of inciting violent instabilities in I-fronts, but are not relevant to the r^{-2} gradients in the current test. Another type of instability can appear in D-type fronts when photons are incident to the front at oblique angles (Williams 2002), but they cannot develop in I-fronts given the imposed initial spherical symmetry of this test.

The third type, shadow instabilities, can appear when a density perturbation is advected through an R-type front, forming dimples that erupt into violent instabilities when the I-front becomes D-type (Williams 1999). Although the density profile in this test is radially symmetric, prescriptions for imposing spherically-symmetric profiles on a Cartesian mesh as a function of radius that are too simple can lead to minor departures from radial symmetry in densities between neighbor grid points. As the front crosses these mesh points it can become dimpled just as if real physical perturbations had traversed it. These corrugations would then grow into the much more prominent features visible in the 25 Myr images upon transformation of the front to D-type. If this were the case, they would be dampened by employing higher grid resolution or by a better prescription for smoothing densities between neighbor mesh points. We tested the latter possibility by applying an algorithm in C^2-Ray that sub-sampled volumes enclosed between adjacent points in radius with thirty more finely subdivided shells and then interpolated densities accordingly between the points. This measure failed to alleviate the instabilities in the I-front in C^2-Ray, suggesting that they are not shadow instabilities.

Instead, their shape and position at early times reveal that they are the infamous 'carbuncle' phenomenon or 'odd-even decoupling' (Quirk 1994). Low-diffusion solvers, such as the Roe's approximate Riemann solver employed in Capreole+C^2-Ray and the PPM Riemann solvers in Flash-HC and Enzo-RT, sometimes suffer from these numerical instabilities. They occur when shocks

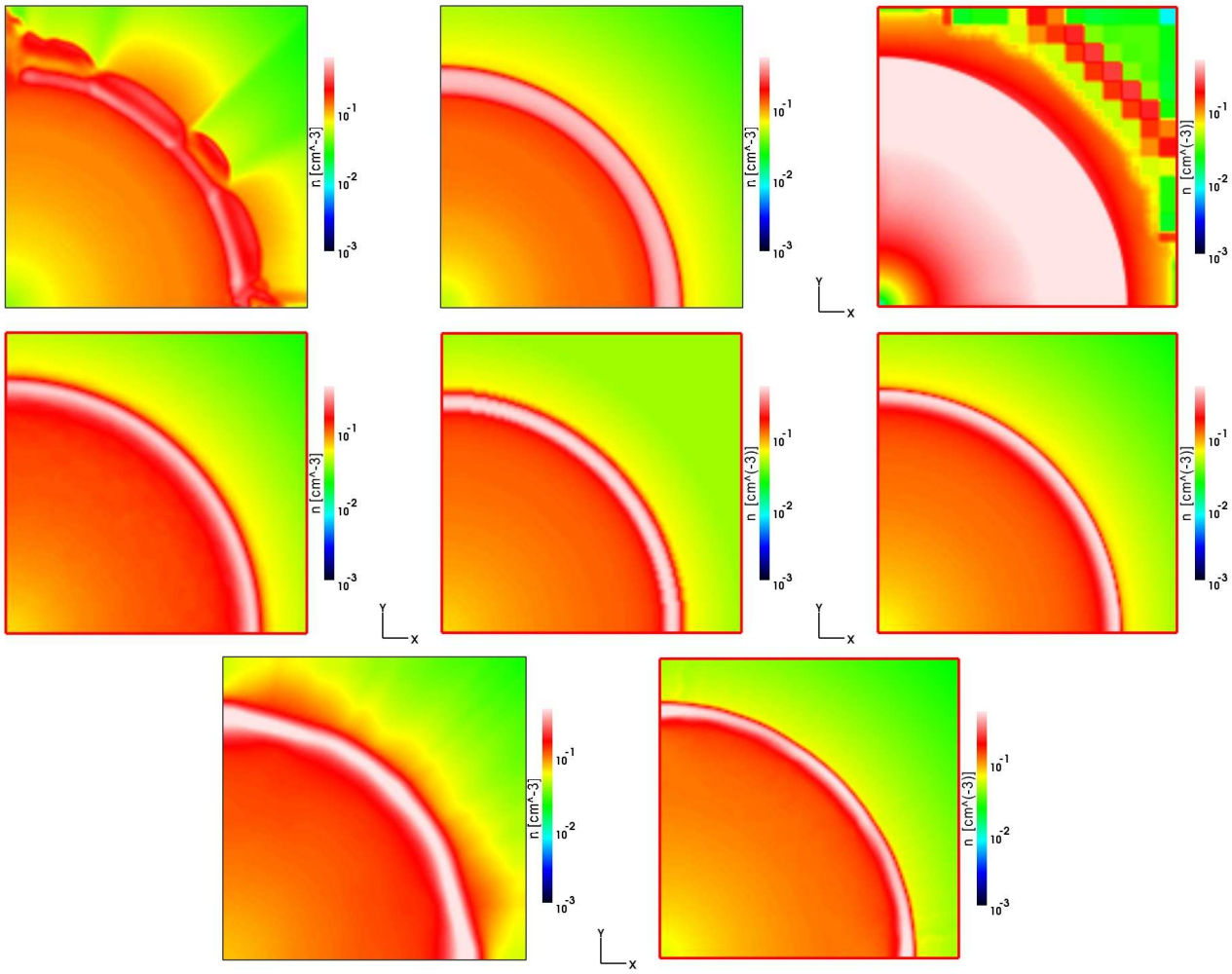

Figure 22. Test 6 (H II region gasdynamic expansion down a power-law initial density profile): Images of the density, cut through the simulation volume at coordinate $z = 0$ at time $t = 25$ Myr for (left to right and top to bottom) Capreole+C^2-Ray, TVD+C^2-Ray, HART, RSPH, ZEUS-MP, RH1D, LICORICE, and Flash-HC.

travel parallel to one of the coordinate axes, in this case beginning near the symmetry axes of the expanding shell. These instabilities are well-known and mostly understood, although their occurrence is not always predictable. Although by 25 Myr most of the shell has been disrupted, we find that the perturbations begin near the axis and exhibit the characteristic morphology of the carbuncle instability. While the usual solution is to artificially introduce more diffusion only where it is needed, this approach did not suppress the phenomenon in C^2-Ray. If the test is instead run with C^2-Ray coupled to the TVD solver of Trac and Pen (Trac & Pen 2004), which is more diffusive and not known to suffer from the carbuncle instability, the shell indeed remains well behaved. We also note that this carbuncle instability, while fairly violent, does not in fact affect the fluid flow or I-front propagation significantly and the I-front position and velocity evolution discussed above and the spherically-averaged profiles discussed below are still in good agreement with the other results. Therefore, effect of this is fairly modest at the early times studied here, but as the previously cited work demonstrates, they could become important at later times.

Another possibility is that there is a hitherto unknown breakout instability associated with the transition of the D-type I-front back to R-type as it descends the density gradient. However, such an instability would not have the opportunity to propagate throughout and disrupt the entire shell during breakout as in the C^2-Ray results because the transition from D-type to R-type is too abrupt, and, as discussed above, the I-front remains D-type within the computational volume. Such an instability would instead be manifest as a premature supersonic runaway of radiation from the surface of the shell along certain lines of sight with little disruption of the shell itself, as observed in the Flash-HC results. However, this does not happen in the ZEUS-MP profiles, which are computed on a 3D spherical coordinate grid that is naturally suited to spherically-symmetric density fields and on which the 'corner' effects inherent in Cartesian grids are absent. Furthermore, as the spherically averaged profiles show, the I-front in this test is not on the verge of breaking past the shock and becoming R-type at late times. We therefore conclude that the instability in the Flash-HC results is not physical and that the early breakout of radiation there is at least partly the result of gridding a spherical density on a Cartesian grid. The effect of this is fairly modest, however, and does not disturb the overall dynamics significantly.

The irregular morphology of the shell in the LICORICE results and to a small extent in the RSPH profile at 25 Myr is likely due to spurious fluctuations in the density field where the local

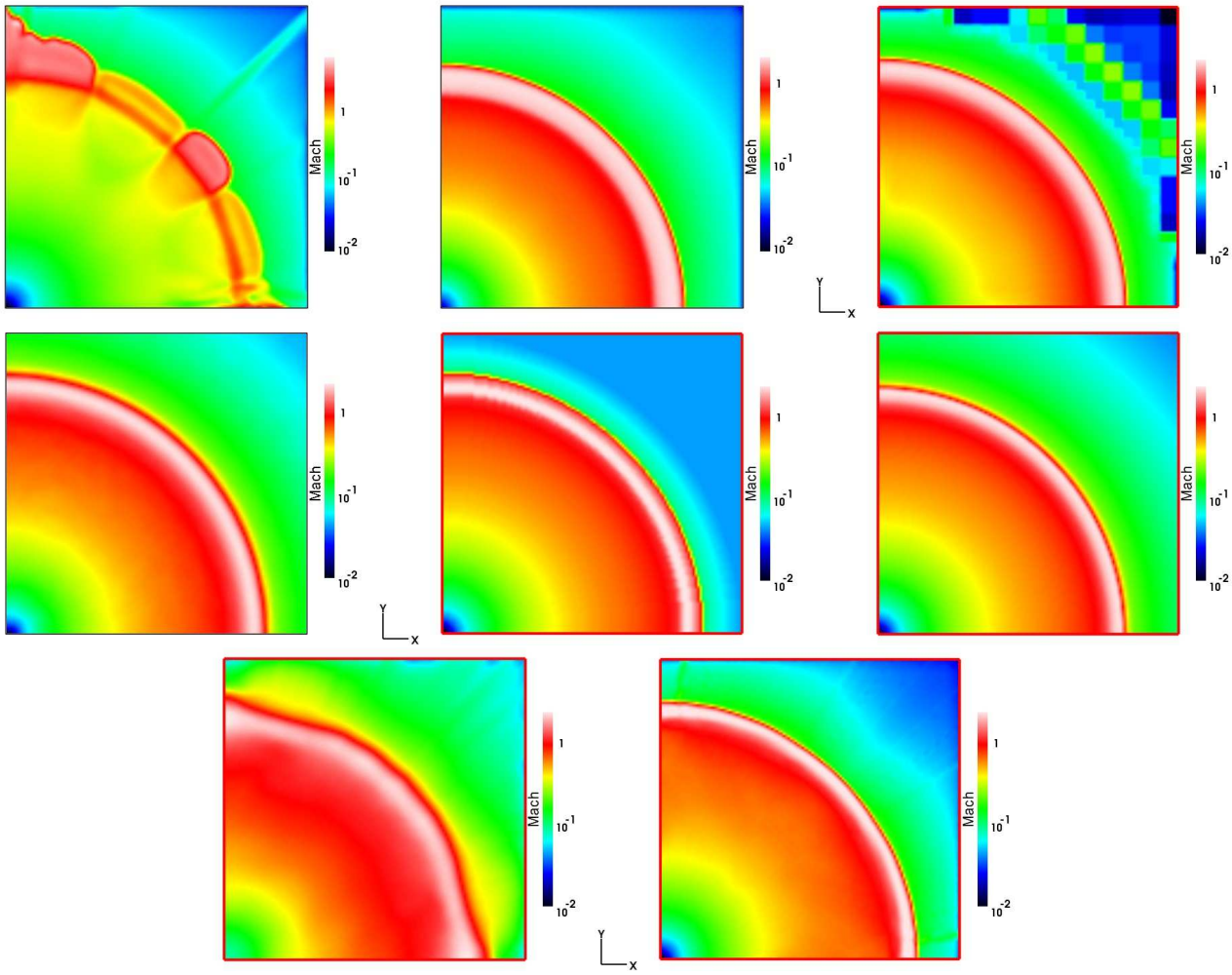

Figure 23. Test 6 (H II region gasdynamic expansion down a power-law initial density profile): Images of the Mach number, cut through the simulation volume at coordinate $z = 0$ at time $t = 25$ Myr for (left to right) and top to bottom) Capreole+C^2-Ray, TVD+C^2-Ray, HART, RSPH, ZEUS-MP, RH1D, LICORICE, and Flash-HC.

particle number changes sharply, in this case in the vicinity of the dense shell. This well-known feature of SPH, as discussed in section 2.7, is what probably allows radiation to preferentially advance along lines of sight through low-density fluctuations in the two profiles. The larger effects for LICORICE compared to RSPH are probably due to the usage of a grid to perform the radiative transfer in the former. Once again, none of these effects appears to affect the overall evolution significantly, but they might matter in certain astrophysical situations.

The HART results exhibit banding in all the profiles except for HI fraction at 25 Myr. The origin of these features is unclear, but is possibly related to the much coarser AMR griding used around the outer edges. They may also be related to the greater diffusivity of the OTVET algorithm, although no such features were observed in the other tests performed with OTVET. However, the density profile found by HART is much flatter, with no clear dense shell swept by the shock, in clear contrast to all other results. It is possible that the time step applied to the gas energy updates in HART is too coarse for I-fronts in r^{-2} density gradients, which has been found to lead to banding in temperatures and densities in H II regions in stratified media (Tenorio-Tagle et al. 1986; Whalen & Norman 2006).

We finally note that had H_2 cooling been included in either this test or in Test 5, violent physical instabilities might have arisen in the I-front when it became D-type (Whalen & Norman 2008a). Hard UV spectra significantly broaden ionization fronts, forming regions of a few thousand K and ionized fractions of 10% in their outer layers. These are prime conditions for the catalysis of H_2 via the H^- channel, which forms between the I-front and the dense shocked shell when the front becomes D-type (Ricotti et al. 2002). H_2 - H, H_2 - e^-, and H_2 - H^+ collision channels emit ro-vibrational lines (Lepp & Shull 1983; Galli & Palla 1998b; Glover & Abel 2008) that can radiatively cool the base of the shocked layer and incite dynamical instabilities there just as metal ions do in galactic I-fronts. These instabilities may have been common in the early universe, such as in UV breakout from the first star-forming clouds. They appear if there is enough H_2 in the cloud to self-shield from the Lyman-Werner (LW) flux (11.18-13.6 eV) also being emitted by the source, which photodissociates molecular hydrogen (Draine & Bertoldi 1996). Thus, while the instabilities manifested by some of the codes in Test 6 are numerical, physical ones are possible when H_2 cooling, LW photons, and self-shielding to LW radiation are properly included. Since not all the codes contain these physical processes, it was not included in any of the current tests, but will be a target for future stages of this comparison project.

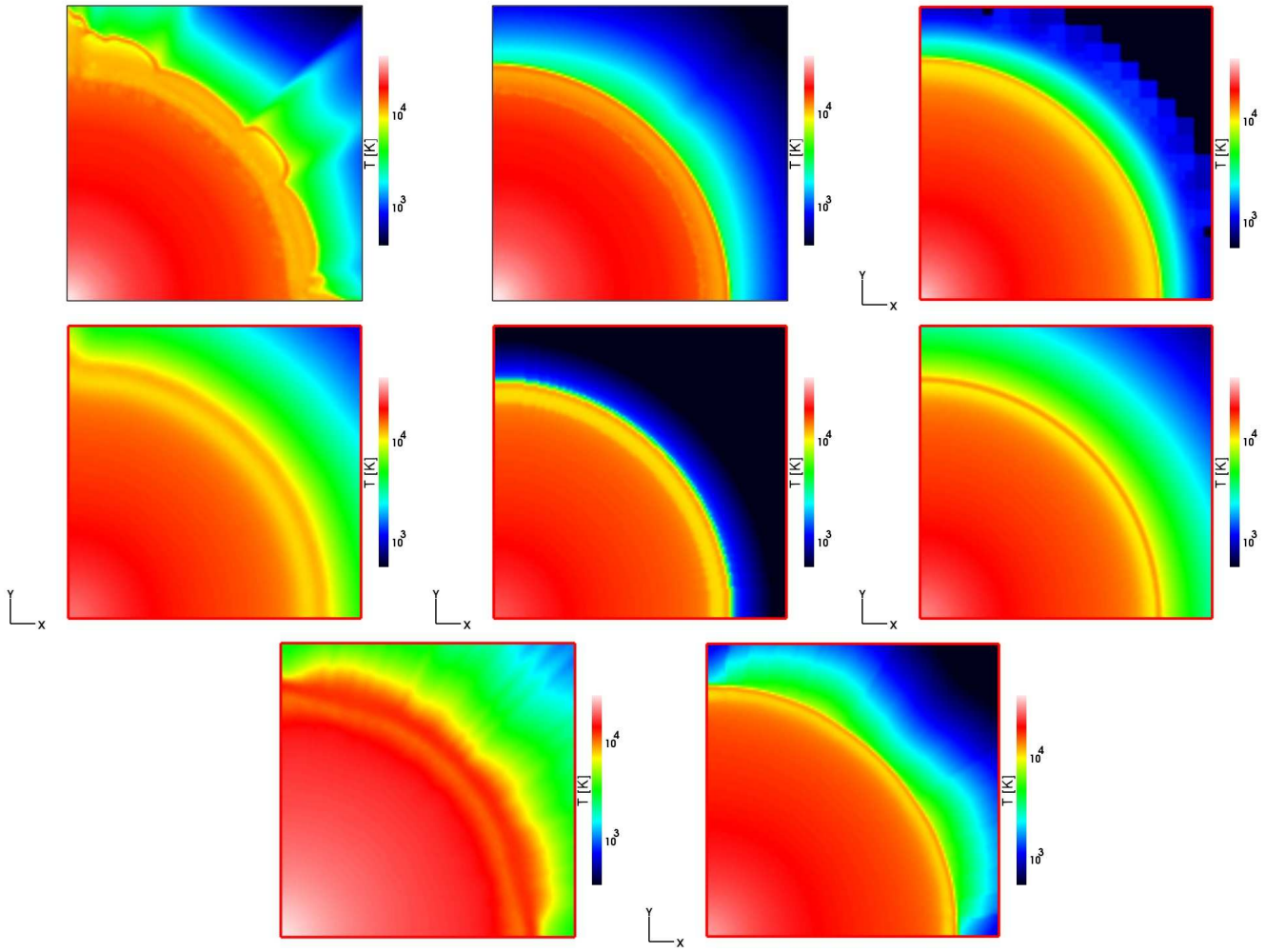

Figure 24. Test 6 (H II region gasdynamic expansion down a power-law initial density profile): Images of the temperature, cut through the simulation volume at coordinate $z = 0$ at time $t = 25$ Myr for (left to right and top to bottom) Capreole+C^2-Ray, TVD+C^2-Ray, HART, RSPH, ZEUS-MP, RH1D, LICORICE, and Flash-HC.

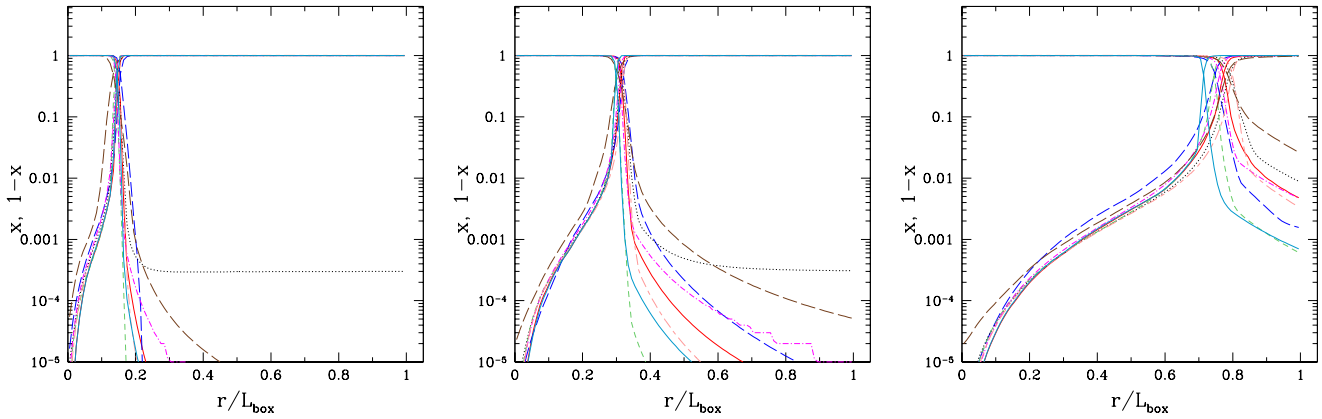

Figure 25. Test 6 (H II region gasdynamic expansion down a power-law initial density profile): Spherically-averaged profiles for ionized fractions x and neutral fractions $x_{\rm HI} = 1 - x$ at times $t = 3$ Myr, 10 Myr and 25 Myr vs. dimensionless radius (in units of the box size).

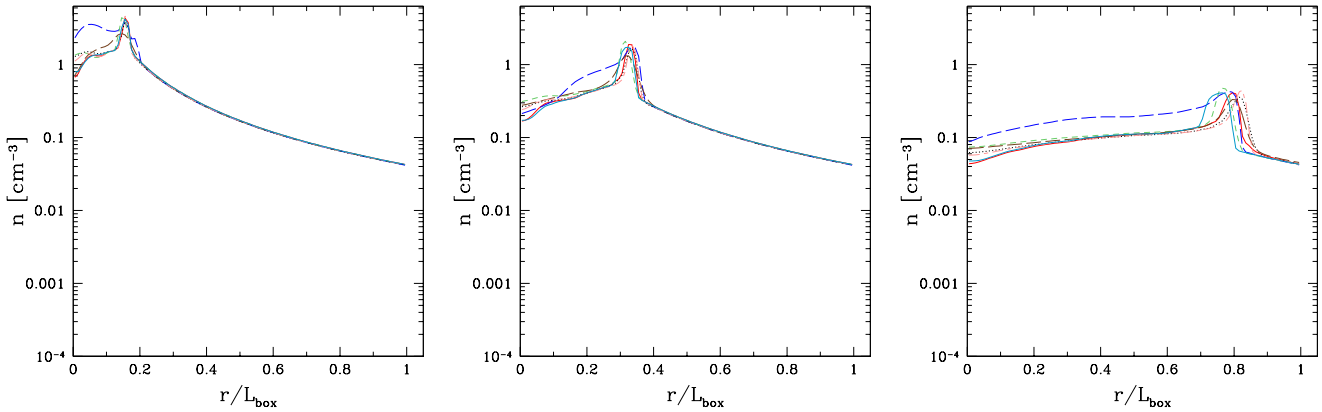

Figure 26. Test 6 (H II region gasdynamic expansion down a power-law initial density profile): Spherically-averaged profiles for the gas number density, n, at times $t = 3$ Myr, 10 Myr and 25 Myr vs. dimensionless radius (in units of the box size).

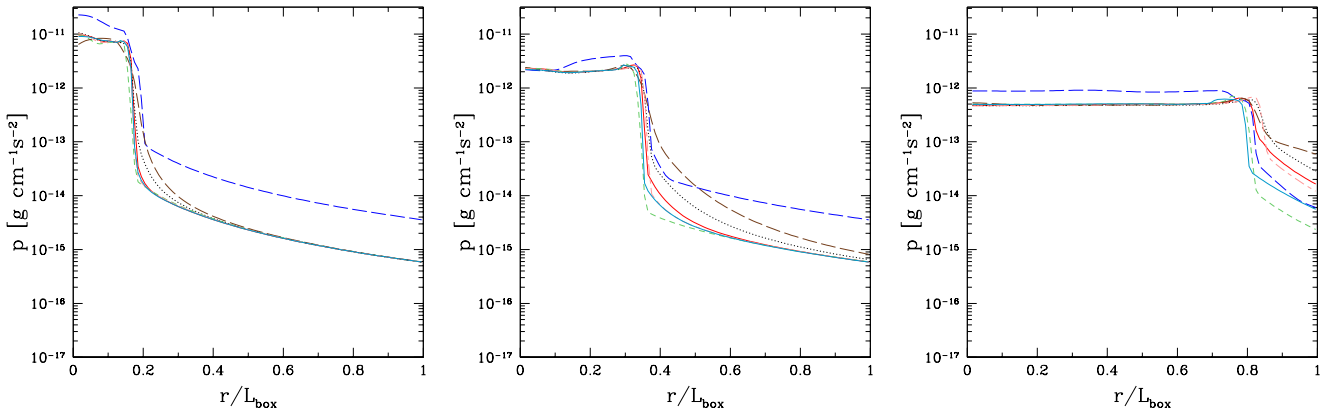

Figure 27. Test 6 (H II region gasdynamic expansion down a power-law initial density profile): Spherically-averaged profiles for pressure, p, at times $t =$ 3 Myr, 10 Myr and 25 Myr vs. dimensionless radius (in units of the box size).

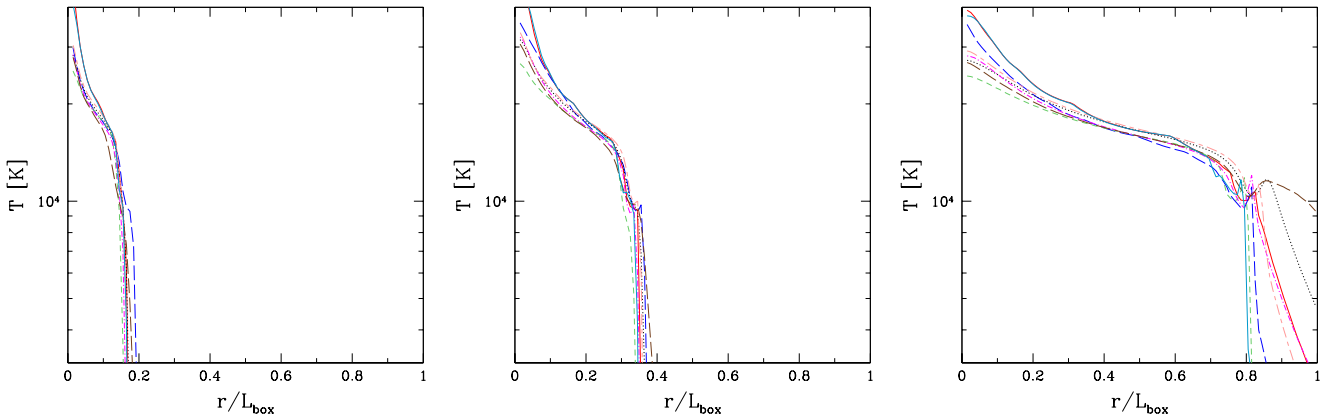

Figure 28. Test 6 (H II region gasdynamic expansion down a power-law initial density profile): Spherically-averaged profiles for temperature at times $t =$ 3 Myr, 10 Myr and 25 Myr vs. dimensionless radius (in units of the box size).

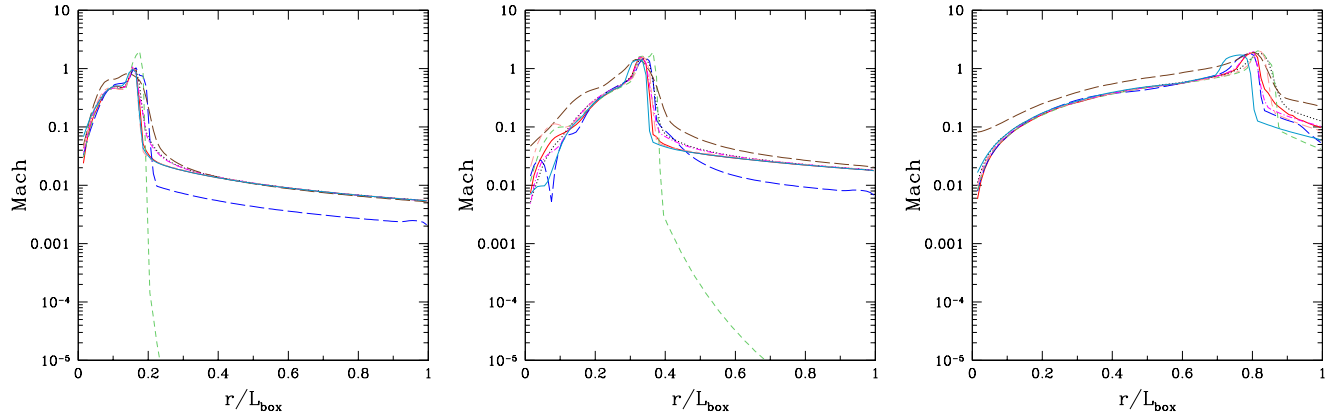

Figure 29. Test 6 (H II region gasdynamic expansion down a power-law initial density profile): Spherically-averaged profiles of the Mach number at times $t = 3$ Myr, 10 Myr and 25 Myr vs. dimensionless radius (in units of the box size).

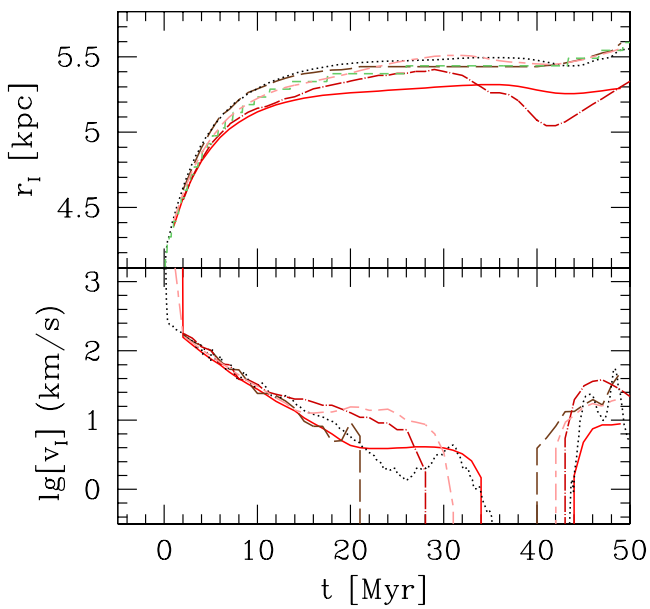

Figure 30. Test 7 (Photoevaporation of a dense clump): The evolution of the position and velocity of the I-front along the axis of symmetry through the centre of the clump.

In spite of the prominence of the numerical instabilities in some of the codes, we re-iterate that they were not catastrophic to the overall dynamics over the range of radii and interval of time which we study here, as shown by the spherically averaged hydrodynamical profiles. In Figs 25 - 29 we show ionization fractions, number densities, pressures, temperatures and Mach numbers at 3, 10, and 25 Myr. Comparison of ionization fractions and densities at 3 Myr indicates that the I-front is D-type at $r \sim 120$ pc, somewhat beyond the flat central core of the initial density profile. A thin layer of shocked neutral gas is visible at $r \sim 140$ pc in the Mach number profile. Acoustic waves are evident at $r < 100$ pc within the H II region in both the density and Mach number plots and are consistently reproduced by all the codes.

At this early stage, the I-front widths (customarily defined by the difference between the positions at which 0.1 and 0.9 ionization fractions are reached) vary from ~ 20 pc to 40 pc. At the relatively high inner-profile density of $n \sim 1$ cm^{-3}, the mean free paths (mfp) of 13.6 eV and 60 eV photons, which roughly bracket the available energies in the 10^5 K black-body spectrum used for this test, are ~ 0.05 pc and 4 pc, respectively. The intrinsic width of the I-front is approximately 20 mean-free paths, or between 1 and 80 pc. Therefore, all the codes give widths roughly consistent with the expected values, but somewhat on the wider side, primarily due to the diffusivity of some of the algorithms. In particular, LICORICE and HART have wider fronts, while ZEUS-MP has the narrowest one and the rest are spread between those two extremes. As explained above, the details of the structure of the I-front are interesting since they relate to the formation of molecular hydrogen in its outer layers (e.g. Ricotti et al. 2002) where hard, deeply penetrating photons could yield a positive feedback mechanism during early structure formation. The post-front (ionized) gas temperatures of the codes at these early times differ by at most 10%. The low Mach numbers outside the H II region at early times, ranging from 0.001 to 0.01 arise because hydrostatic equilibrium was not imposed on the original density profile in any of the codes except for ZEUS-MP. Pressure forces gently accelerate the gas outward, but this has little effect on the late-time evolution of the H II region. For the purposes of this comparison the lack of initial hydrostatic equilibrium is irrelevant, as long as all codes start from the same initial conditions.

By 10 Myr the H II region has grown to 240 pc, with all results agreeing well on the I-front position. There is very little variation in the ionization structure inside the H II region, with only LICORICE finding a slightly lower level of ionization. The differences in the pre-front ionization structures are much more pronounced, underlying again the variety in the treatments of multi-frequency photons. All the codes still find postfront gas temperatures within 10% of one another at most radii. The temperature profiles drop sharply just beyond the I-front as before, but then briefly plateau at 10^4 K for ~ 16 pc before falling further. This is the dense ambient neutral gas shell-swept up by the shock, clearly seen in the density profiles (Figure 26), which is sufficiently hot and dense to become collisionally ionized to a small degree. However, the minute residual ionized fractions (10^{-4} - 10^{-3}) in and beyond the shell in most of the plots occur because the I-front broadens over time. As more neutral gas accumulates on the shell with the expansion of the H II region, its density decreases because its area grows, and its opti-

cal depth to photons in the high-energy tail of the spectrum decreases. ZEUS-MP still finds the sharpest I-front and LICORICE the thickest, with the rest dispersed between. No single cause can be ascribed to the moderate variation in I-front structure amongst the codes; for example, both ZEUS-MP and RH1D perform multifrequency ray-tracing radiative transfer with similar integration schemes and frequency binning, but RH1D has a noticeably wider I-front. Tabulating pre-computed frequency-dependent ionization rate integrals as a function of optical depth as an alternative to full multifrequency RT in Capreole+C^2-Ray leads to a somewhat different structure for the front. There is an unmistakable trend toward greater diffusivity with the SPH-coupled radiative transfer codes RSPH and LICORICE that is likely related to the inherent difficulty in representing low-density regions with SPH particles and the tendency of SPH to broaden shocks. Nonetheless, the grid-based codes and RSPH agree to within a few percent on the density structure of the shocked shell at 10 Myr. LICORICE does not resolve the shell as well, but this would likely be remedied by using more particles to resolve the flow, or by using a more adaptive smoothing kernel. Overall, the codes agree reasonably well on the shock position and the corresponding density and pressure jumps (although, as was discussed above, HART yields higher and more uniform density and pressure distributions behind the shock than the other the methods, which agree on that quite well among themselves).

At 25 Myr the I-front is at 640 pc, approaching the boundary of our computational volume. At this stage the subsonic expansion of the front with respect to the sound speed in the ionized gas is evident: acoustic waves have erased density fluctuations up to the shocked shell in the pressure and density plots. The acceleration of the shock down the density gradient can be seen in the heating by the shock: the temperature of the dense shell is 25% greater than at 10 Myr. The velocities beyond the shock are now 20% of the sound speed of the neutral gas, and the peak density of the shell has fallen to 0.4 cm^{-3}. There is a 10% variation in the position of the I-front among the codes that is not attributable to differences in chemistry or radiative transfer because of the uniformity in ionized gas temperatures (and therefore sound speeds). More likely, it is due to the variety of hydrodynamics schemes (both grid and particle based) applied to the models. Apart from the diffusivity of some of the algorithms as manifest in I-front structure, we find good agreement on the evolution of the H II region in this stratified medium between all the codes. Direct multifrequency RT and approximations to full multifrequency transfer with precomputed ionization integrals both yield extended I-front structures, but it is difficult to assess which is more accurate since even the two direct methods disagree with each other to some degree. The disagreement between the multifrequency codes on the width of the I-front is probably due to their discretization of the blackbody curve and resultant binning of ionizing photon rates according to energy, since they otherwise employ the same ionization cross sections and photon-conserving ray tracing. The number of bins per decade in energy and their distribution in frequency can lead to different thicknesses for the front. They have a much smaller effect on the temperature of the ionized gas, and therefore the position of the front, because the temperature is more strongly governed by the cooling rates than by minor discrepancies in spectral profile.

4.3 Test 7

The evolution of the I-front along the axis of symmetry through the center of the dense clump is shown in Figure 30. The I-front starts off very fast, R-type in the low-density medium surrounding the dense clump, but slows down quickly once it enters the high-density gas, which occurs in less than a Myr. Thereafter, the front slows down more gradually as source photons encounter more and more recombining atoms in the photoevaporative flow, which attenuates the flux which reaches the I-front. This initial trapping phase is largely over by $t = 1$ Myr, yielding a thin ionized layer in the dense clump on the source side and a clear shadow behind, as illustrated in Figure 31. Due to the short evolution time, by this point the gas is still essentially static and Test 6 reproduces the analogous stage in Test 3 in Paper I. There are only a few modest differences between the neutral gas distributions. The boundary of the shadowed region ”flares” especially for the RSPH result, primarily because their particle neighbour list based ray-tracing scheme inevitably introduces some ”diffusion of optical depth”, whereby high optical depth spreads through the neighbour list. Flaring of the boundary is also in part due to the interpolation procedures to set up the initial conditions which, with their sharp boundaries, are unnatural for SPH and thus difficult to represent well. In fact, even grid-based codes exhibit similar problems, since the low resolution required in this Test imposes some grid artefacts on the spherical dense clump that are later manifest as ripples in the ablation shock of the clump unless a smoothing procedure is applied at the setup of the problem. To minimize artificial features in the photoevaporative flow from the clump, ZEUS-MP and C^2-Ray implemented the same smoothing procedure to the clump as in Test 6 in their initial density profiles. There is also some faint striping of the neutral fraction in the low-density region for the case of LICORICE, probably due to insufficient Monte-Carlo sampling, as was discussed earlier. However, this does not have any apparent effect on the photoevaporation of the clump.

Once the front speed drops below v_R a shock starts to form ahead of it, converting it to D-type front. The photoheated material on the source side starts photoevaporating, by blowing supersonic wind towards the ionizing source. The I-front slowly eats its way into the dense clump, as shell after shell of gas boils off and joins the wind. The I-front velocity gradually drops to a few km/s and its position remains roughly constant. Some differences among the derived I-front evolution in position and velocity are observed, but they remain small throughout the evolution, never exceeding 10% in terms of position. In Figure 32 we show images of the neutral hydrogen fraction at $t = 10$ Myr. Overall results agree fairly well, with the expanding wind and shadow at very similar stages of evolution. There are also a few, relatively minor, differences which should be noted. The RSPH result remains somewhat more diffuse and asymmetric then the rest, as noted above, but as the evolution proceeds the differences are somewhat less notable. However, the photoevaporation does proceed somewhat more rapidly in this case due to the inevitably more diffuse initial conditions. There is some leaking of light at the edges of the LICORICE shadow which is not seen in the other results and should therefore be related to the radiative transfer method employed, rather than to other factors, e.g. to the limb column density of the clump being small and allowing some light to go through. Finally, there are some uneven features at the edge of the shadow on the source side in the case of Flash-HC, whose origin is currently unclear.

The pressure images at $t = 10$ Myr in Figure 33 essentially agree, with only minor morphological differences between the results. The shadow is somewhat thicker and less squeezed at the edges for C^2-Ray, ZEUS-MP and Flash-HC, compared to RSPH and LICORICE, with Coral results intermediate between the two groups. The reason for this difference becomes apparent from the corresponding temperature images (Figure 34). In the cases of C^2-

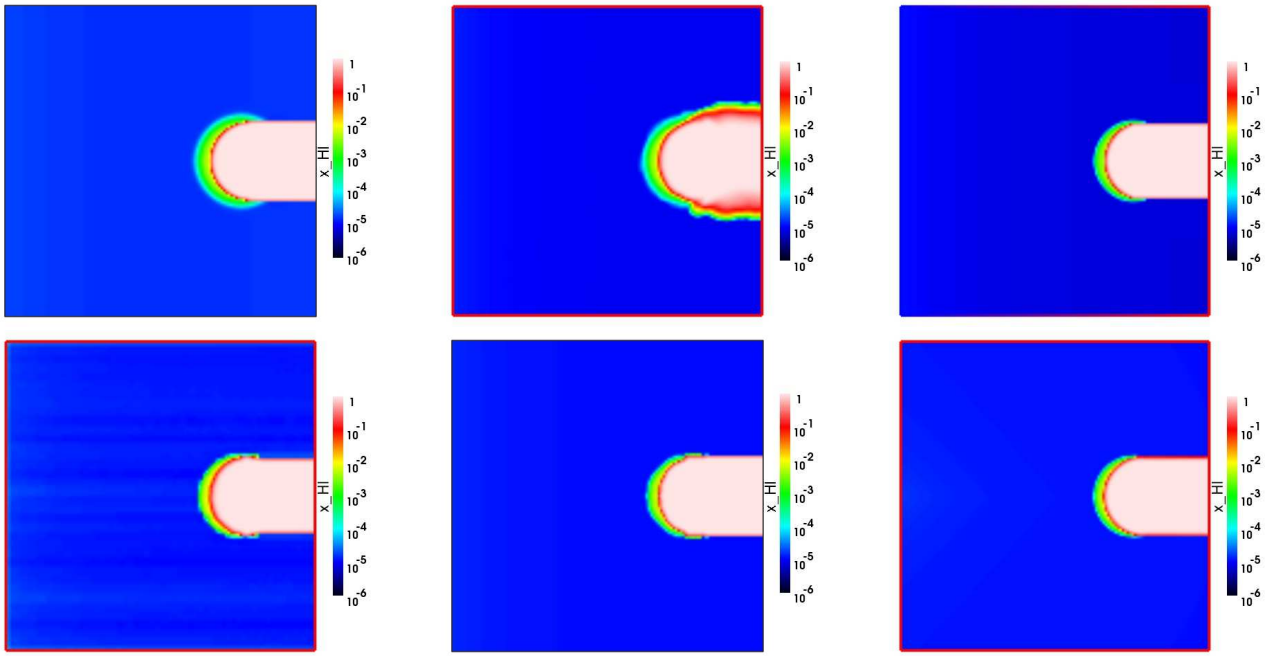

Figure 31. Test 7 (Photoevaporation of a dense clump): Images of the H I fraction, cut through the simulation volume at coordinate $z = 0$ at time $t = 1$ Myr for (left to right and top to bottom) Capreole+C^2-Ray, RSPH, ZEUS-MP, LICORICE, Flash-HC and Coral.

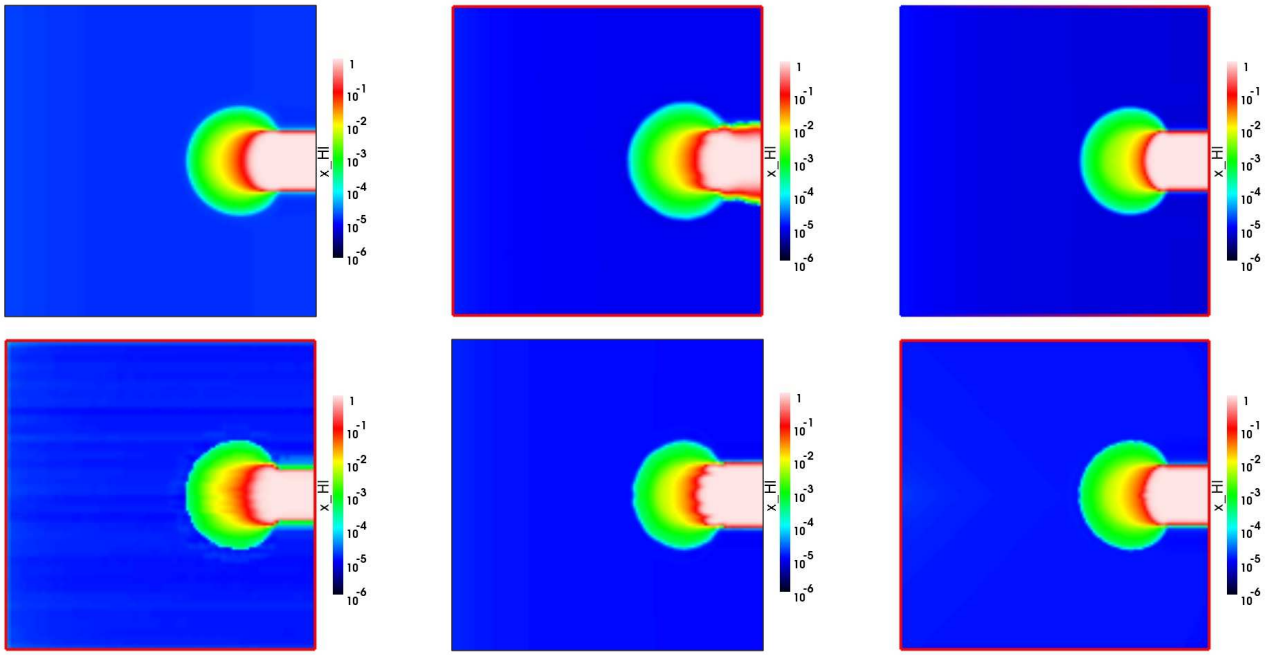

Figure 32. Test 7 (Photoevaporation of a dense clump): Images of the H I fraction, cut through the simulation volume at coordinate $z = 0$ at time $t = 10$ Myr for (left to right and top to bottom) Capreole+C^2-Ray, RSPH, ZEUS-MP, LICORICE, Flash-HC and Coral.

Ray, ZEUS-MP and Flash-HC there is clear temperature gradient from the edges of the shadow going inward, while for RSPH and LICORICE this temperature gradient is largely absent. There are also noticeable temperature variations within the clump for C^2-Ray, ZEUS-MP and Flash-HC which are less pronounced for RSPH and LICORICE. The reason for these differences appears to be the different levels of penetration by hard photons through the high column density material in the clump, and the corresponding varying levels of energy deposit by those photons. The variations in evolution this introduces seem minor in our particular test problem, but such differences might matter more in problems in which the precise level of the number of free electrons and the local temperature within dense clumps is of importance. One example may be the study of the the production of molecular hydrogen within dense

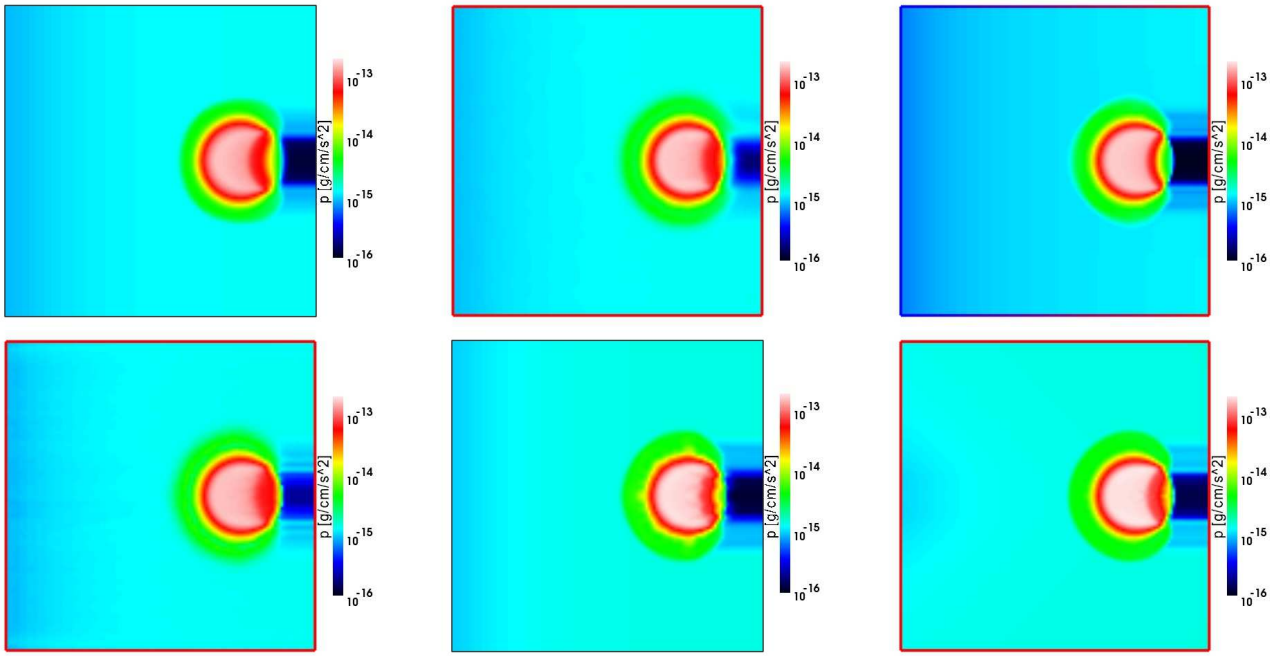

Figure 33. Test 7 (Photoevaporation of a dense clump): Images of the gas pressure, cut through the simulation volume at coordinate $z = 0$ at time $t = 10$ Myr for (left to right and top to bottom) Capreole+C^2-Ray, RSPH, ZEUS-MP, LICORICE, Flash-HC and Coral.

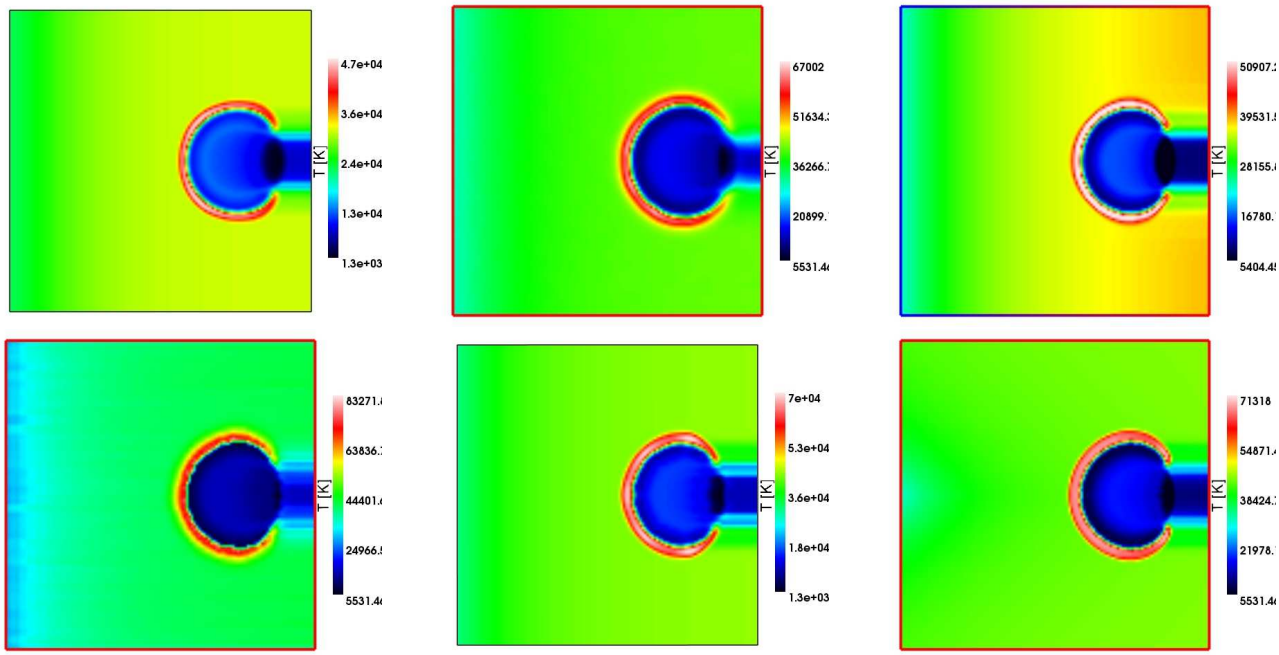

Figure 34. Test 7 (Photoevaporation of a dense clump): Images of the gas temperature, cut through the simulation volume at coordinate $z = 0$ at time $t = 10$ Myr for (left to right and top to bottom) Capreole+C^2-Ray, RSPH, ZEUS-MP, LICORICE, Flash-HC and Coral.

regions irradiated by UV radiation, which can regulate (stimulate or suppress) local star formation (Iliev et al. 2006a; Whalen et al. 2008a). Finally, the Mach number images at $t = 10$ Myr are shown in Figure 35. The supersonic wind which starts to blow towards the ionizing source is clearly visible, with only small differences in terms of the thickness of this layer and the Mach number values between the different runs. The only peculiarity visible here is that in the case of ZEUS-MP this supersonic layer is almost spherical, surrounding the clump from all sides, which is not seen in any of the other results. This appears to be a consequence of the very cold ($T < 1000$ K) region remaining at the back of the clump, which is not present in any of the other cases (see also Figure 43). The reason for this region remaining so cold in the ZEUS-MP simulation is unclear at present, considering that (as we discussed above) the

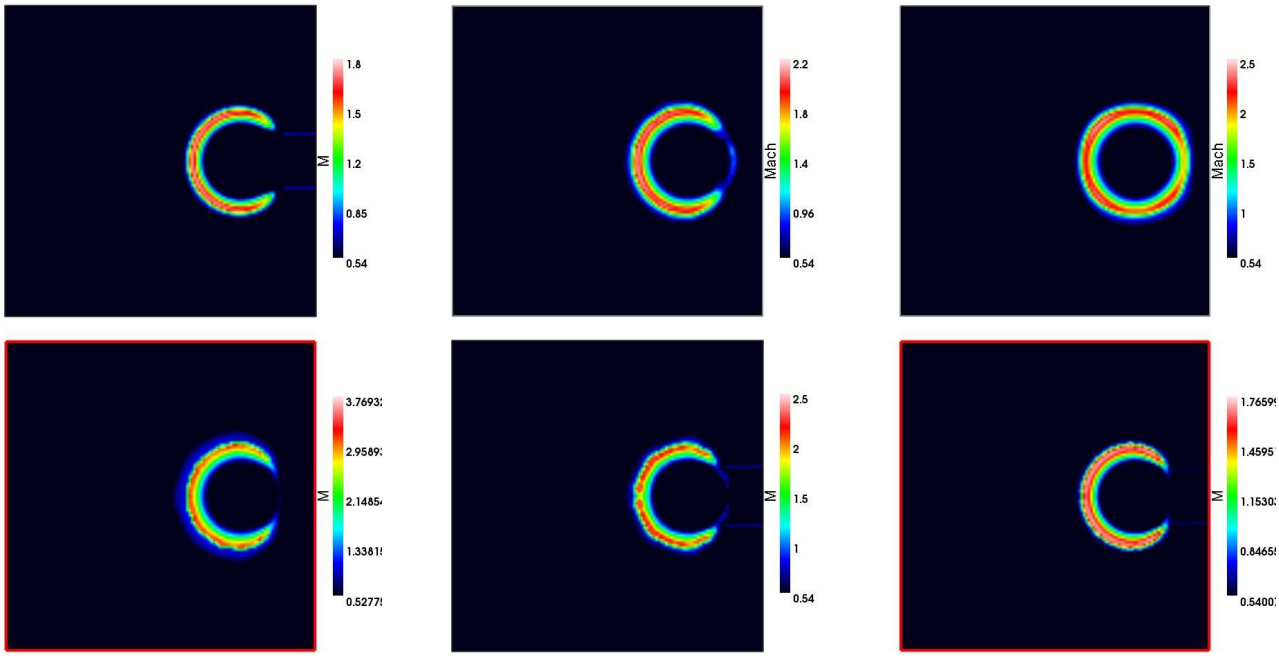

Figure 35. Test 7 (Photoevaporation of a dense clump): Images of the flow Mach number, cut through the simulation volume at coordinate $z = 0$ at time $t = 10$ Myr for (left to right and top to bottom) Capreole+C^2-Ray, RSPH, ZEUS-MP, LICORICE, Flash-HC and Coral.

spectrum hardening and penetration of hard photons through the clump and into the shadow are similar to C^2-Ray, Flash-HC and Coral and stronger than RSPH and LICORICE.

By $t = 50$ Myr (Figures 36-39) the photoevaporation process is well advanced. The region swept by the expanding supersonic wind has grown quite large and takes up a significant fraction of the simulation volume. There are only modest differences in its size between the different codes. In the case of Flash-HC and, to a lesser extent Coral, the edge of the expanding wind region is uneven, as a consequence of the grid effects in the initial conditions, as discussed above, when representing a spherical object on a relatively coarse rectangular grid with no interpolation used. These grid effects could be seen at earlier times as well, but at a lower level. The overall size of the wind region is the same, however, thus this problem does not affect the evolution significantly.

A small core region from the initial clump remains neutral and still casts a clear shadow which also remains neutral in all cases. This neutral region is moderately compressed by the higher external pressure of the ionized and heated gas surrounding it. The size of this neutral dense core and its shadow varies between the runs, being somewhat larger for Capreole+C^2-Ray, Flash-HC and Coral than for RSPH, ZEUS-MP and LICORICE. There is also some 'flaring' (i.e. widening) of the shadow for Flash-HC and Coral, probably due to the specific interpolation weighting used in the short characteristics methods they both employ (for discussion and testing of this see Mellema et al. 2006b, Appendix A).

In the pressure and temperature images shown in Figures 37 and 38 we clearly see the shocked shell of gas swept up by the supersonic wind of evaporating clump material. The inner zone on the side of the clump facing the source is being evacuated and is accordingly colder due to adiabatic cooling, while the outer shocked shell is much hotter, with temperatures reaching 40,000-70,000 K (note the different upper limits for the temperature images). Some quantitative and morphological differences are easily noticed. The evacuated region yields a shell of low pressure whose depth varies between the runs by about an order of magnitude, from the very low pressure $\sim 10^{-16}\mathrm{g/cm/s^2}$ found by Flash-HC, through the intermediate cases of RSPH and ZEUS-MP, to the relatively higher pressure $\sim 10^{-15}\mathrm{g/cm/s^2}$ found by Capreole+C^2-Ray, LICORICE and Coral. The dense, high-pressure central region which remains neutral and the shadow behind it show quite different morphologies between the runs, clearly seen in the pressure images (less so in the temperature ones, due to the lack of color dynamic range). This morphology arises as a consequence of successive reflecting oblique shocks which form behind the evaporating clump by the interaction between the evaporative wind and the partly collapsed shadow squeezed inward by the high external pressure of the ionized region. The reason for the morphological differences between the cases is most probably a slight difference in the timing of these shocks for each run, but ascertaining this will require more detailed analysis of the evolution.

Finally, the Mach number images at $t = 50$ Myr shown in Figure 39 show that while the wind is clearly supersonic, with Mach numbers of a few, the shocked swept material moves subsonically. The peak Mach numbers vary from 2 to 3.7, with typical peak values around 3. The shock is clearly somewhat weaker for Coral, a consequence of this code's more diffusive hydrodynamic solver (based on van Leer flux splitting). All other methods, both Eulerian grid-based (Capreole+C^2-Ray, ZEUS-MP and Flash-HC) or particle-based (RSPH, LICORICE) yield very similar results in terms of Mach number values. The only significant difference between the results is again the more spherical high Mach number shell found by ZEUS-MP.

Next we turn our attention to the statistical distributions of the temperature (shown in Figure 40) and the Mach number (in Figure 41). We notice that three distinct temperature phases, represented by the three peaks of the histograms, exist throughout the evolution - hot, photoionized gas with temperatures $T \sim 25,000-$

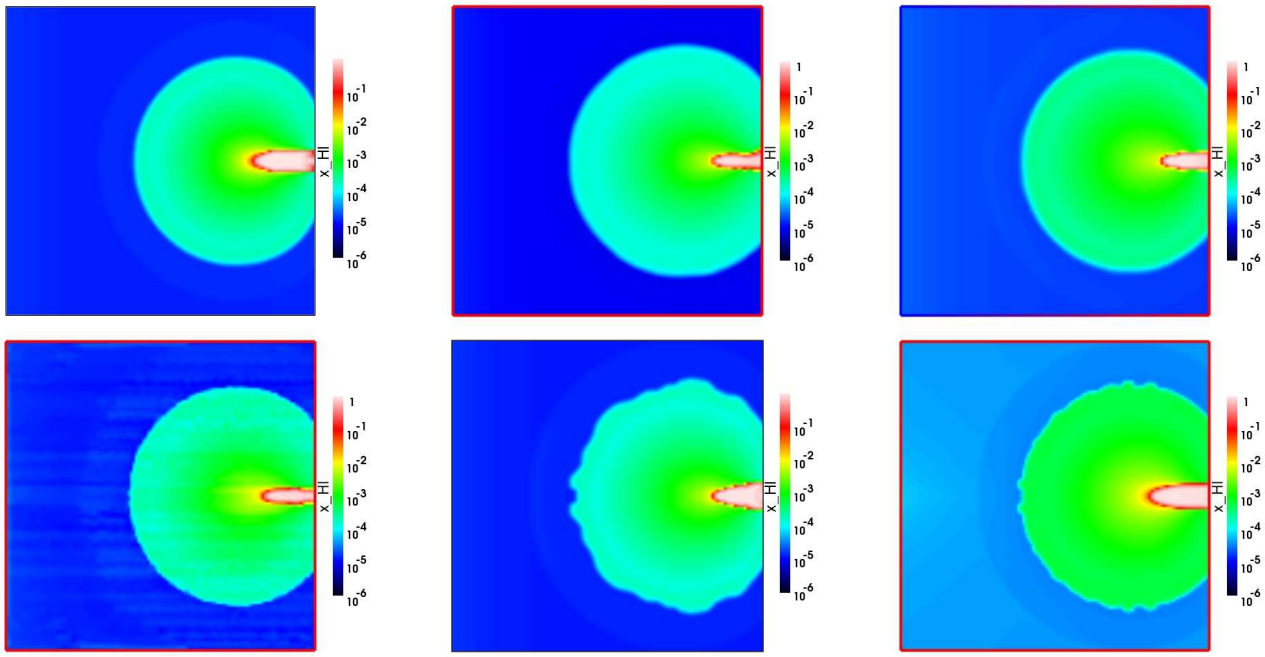

Figure 36. Test 7 (Photoevaporation of a dense clump): Images of the H I fraction, cut through the simulation volume at coordinate $z = 0$ at time $t = 50$ Myr for (left to right and top to bottom) Capreole+C^2-Ray, RSPH, ZEUS-MP, LICORICE, Flash-HC and Coral.

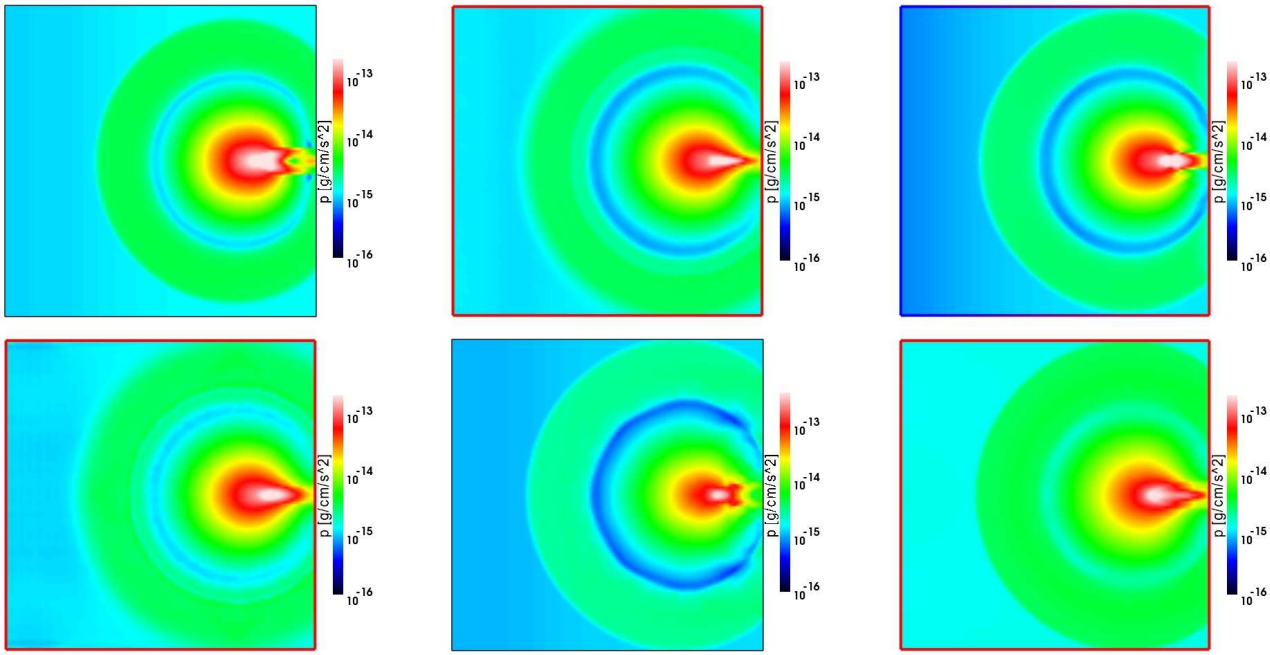

Figure 37. Test 7 (Photoevaporation of a dense clump): Images of the pressure, cut through the simulation volume at coordinate $z = 0$ at time $t = 50$ Myr for (left to right and top to bottom) Capreole+C^2-Ray, RSPH, ZEUS-MP, LICORICE, Flash-HC and Coral.

$45,000$ K, very hot, $T > 50,000$ K, shock-heated gas and a cold phase, consisting in part of self-shielded gas and in part of adiabatically cooled gas behind the expanding supersonic wind. These three phases are observed in all cases and the histograms are very similar. The Mach number histograms are in good agreement as well. For RSPH and LICORICE the hot, shocked phase is less distinct from the photoionized phase. The shocked gas temperature is a bit higher for LICORICE, due to the stronger shock (evidenced by the higher peak Mach number) observed in this case. On the other hand, the temperatures found by Capreole+C^2-Ray are somewhat lower than the rest, which is related to the more approximate treatment of the energy equation in that case.

Finally, in Figures 42-44 we present cuts along the x-axis of the neutral fraction, $x_{\rm HI}$, temperature, T, pressure, p, and Mach

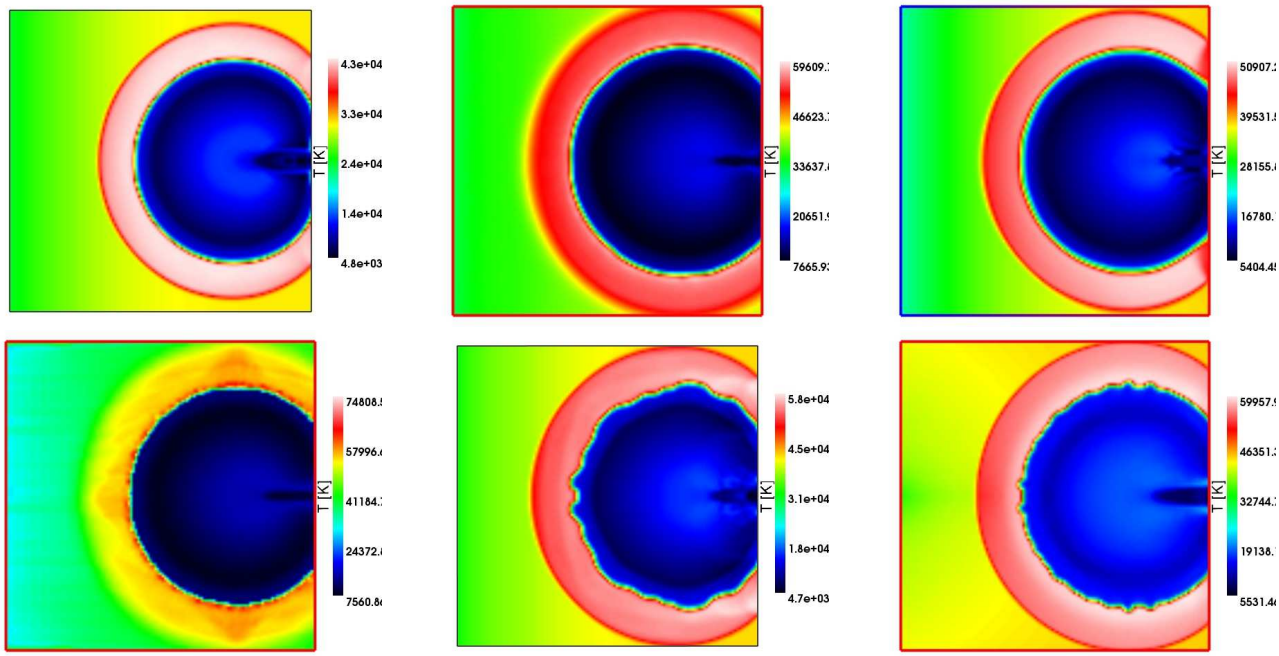

Figure 38. Test 7 (Photoevaporation of a dense clump): Images of the temperature, cut through the simulation volume at coordinate $z = 0$ at time $t = 50$ Myr for (left to right and top to bottom) Capreole+C^2-Ray, RSPH, ZEUS-MP, LICORICE, Flash-HC and Coral.

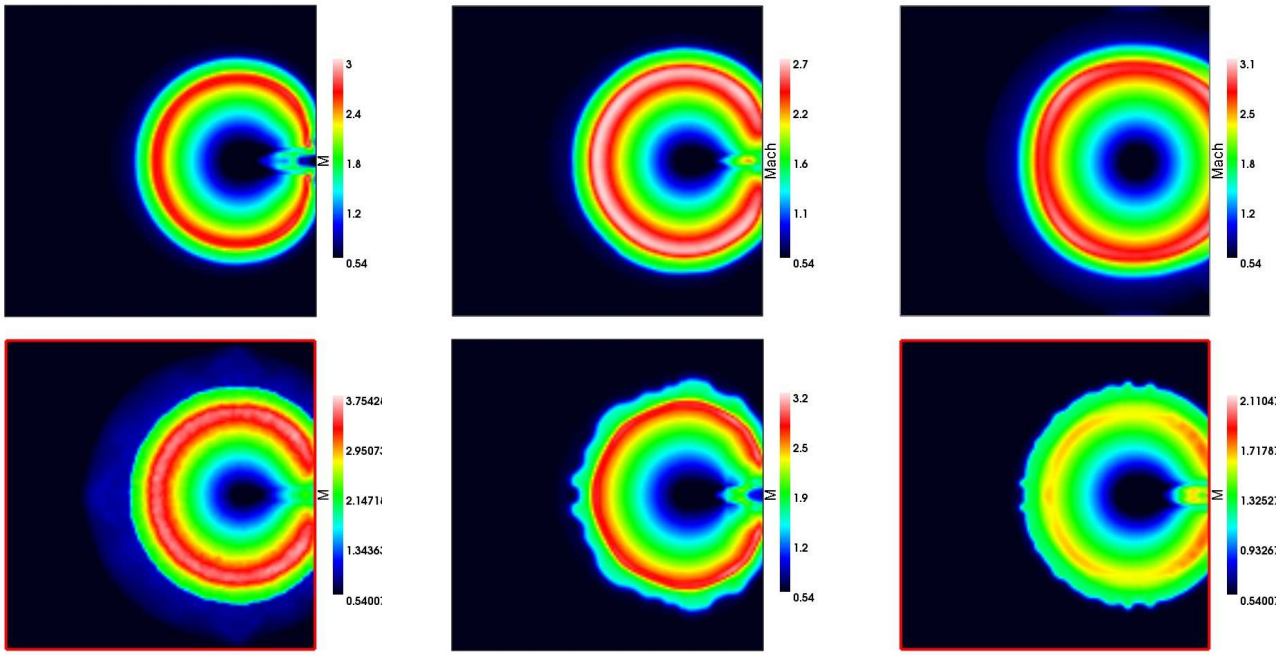

Figure 39. Test 7 (Photoevaporation of a dense clump): Images of the flow Mach number, cut through the simulation volume at coordinate $z = 0$ at time $t = 50$ Myr for (left to right and top to bottom) Capreole+C^2-Ray, RSPH, ZEUS-MP, LICORICE, Flash-HC and Coral.

number M at selected times, as indicated. At early times ($t = 1 - 10$ Myr) all codes agree very well on both the ionization front position and its profile. The only modest differences are found in the semi-shielded part of the dense gas ($x_{\rm HI} = 0.01 - 1$), due to variations of the treatment of hard photons, and in the low-density gas between the clump and the source, where the neutral fractions are affected by the slightly different temperatures found by the different methods. This is confirming the conclusions reached in Paper I that with no (or little) gas motions any differences are due to the treatment of the energy equation and the hard photons. The hydrodynamic evolution introduces some differences, particularly in the I-front position, but the scatter remains small.

The temperature profiles generally agree in shape and in the position of the flow features, the expanding wind and its leading

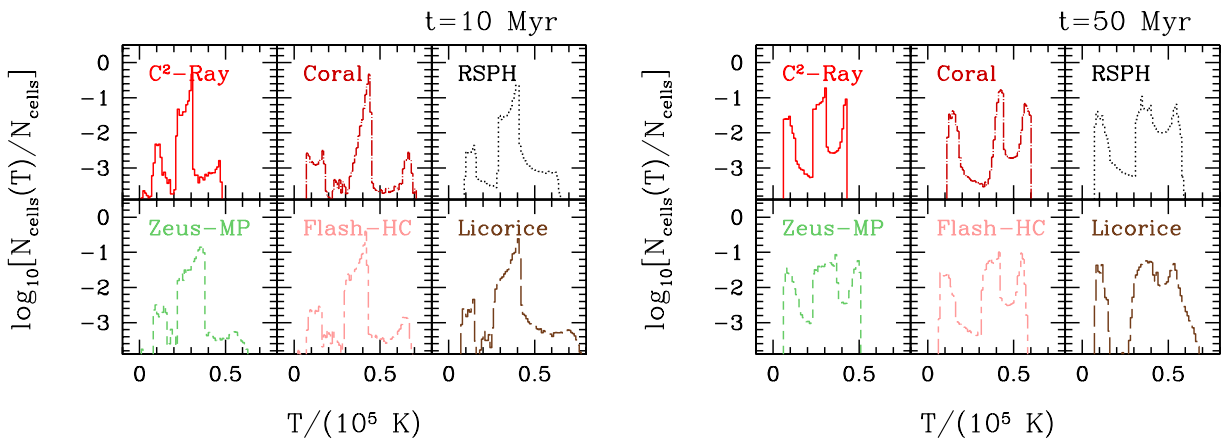

Figure 40. Test 7 (Photoevaporation of a dense clump): Histograms of the gas temperature at times $t = 10$ and 50 Myrs.

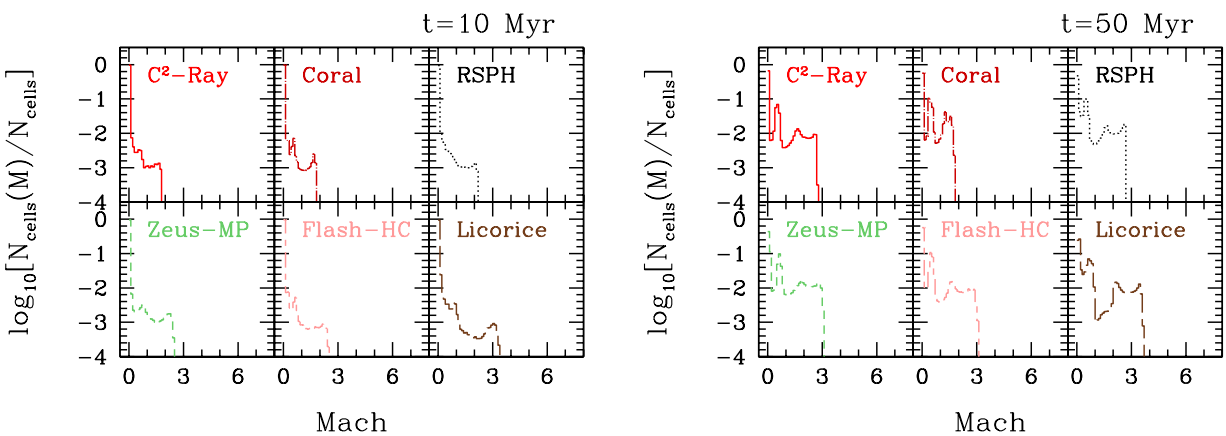

Figure 41. Test 7 (Photoevaporation of a dense clump): Histograms of the flow Mach number at times $t = 10$, and 50 Myrs.

shock. The main differences are in the amplitude, which varies by up to 50%, except for the cold, shielded gas at the back of the remaining dense clump at $t = 10$ Myr (at position $x/L_{\rm box} \sim 0.8$), where the variation between results reached an order of magnitude. This large variation does not affect the later-time evolution considerably, however. The pressure and Mach number profiles (Figure 44) show similar trends, with very small differences during the early evolution, growing to somewhat larger ones at later times, but with all prominent flow features agreeing in both nature and position.

4.4 Summary and Conclusions

In this work we compared the results from 10 directly coupled hydrodynamics and radiative transfer codes on three test problems of astrophysical interest - H II region expansion in initially uniform gas, as well as internal and external photoevaporation of dense clumps of galactic-like size and density. Our aims are to validate our codes and test their reliability. Our test problems, while chosen to be relatively simple and clean, nevertheless cover a wide range of regimes applicable to photoionization-driven astrophysical flows, including propagation of fast (R-type) and slow (D-type) I-fronts, shock creation and supersonic photoevaporative winds. All the data is available on the Radiative Transfer Comparison Project wiki-based website, so future code developers can test their codes against our results.

Overall, the agreement is quite good and all codes are generally reliable and produce reasonable results. However the results also highlighted some important differences between the methods. All participating algorithms track fast, R-type I-fronts well, in agreement with the results we obtained in Paper I. We note that this is not the trivial statement that we simply reproduce our previous static density field results, since in this second Comparison Project phase there are several codes which are newly developed (RH1D, LICORICE, Enzo-RT) and therefore did not participate in Paper I, and even the ones which were present then have been further developed over the intervening period and are thus not identical to the versions used in Paper I.

Again, as we found in Paper I, the treatment of multi-frequency radiative transfer and particularly of the hard tail of the photon spectrum varies significantly among the methods and yields correspondingly large range of temperature and ionization structure just beyond the I-front itself. We showed with a specific example that the spectral energy distribution of the ionizing source changes the I-front structure and shocked flow features considerably. Monochromatic light yields much sharper I-fronts and shocks

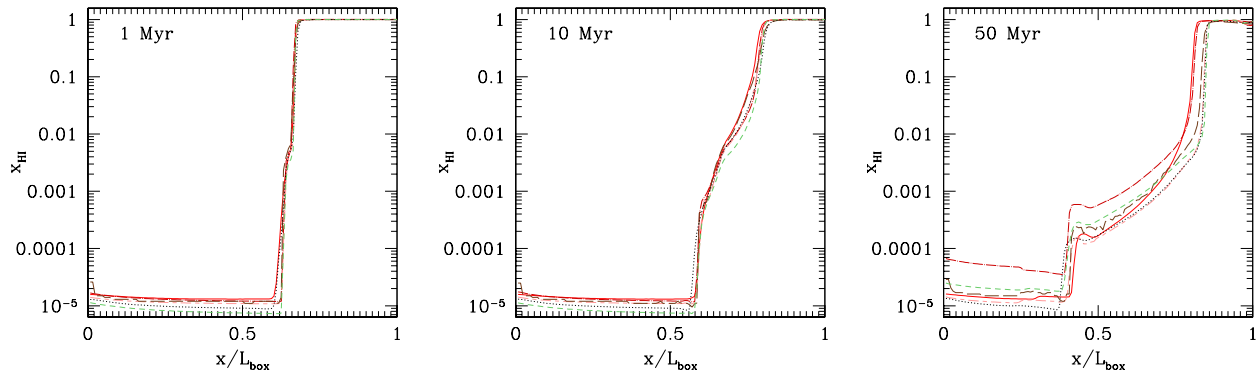

Figure 42. Test 7 (Photoevaporation of a dense clump): Line cuts of the neutral fraction along the axis of symmetry through the centre of the clump at times $t = 1$ Myr, 10 Myr and 50 Myr (left to right).

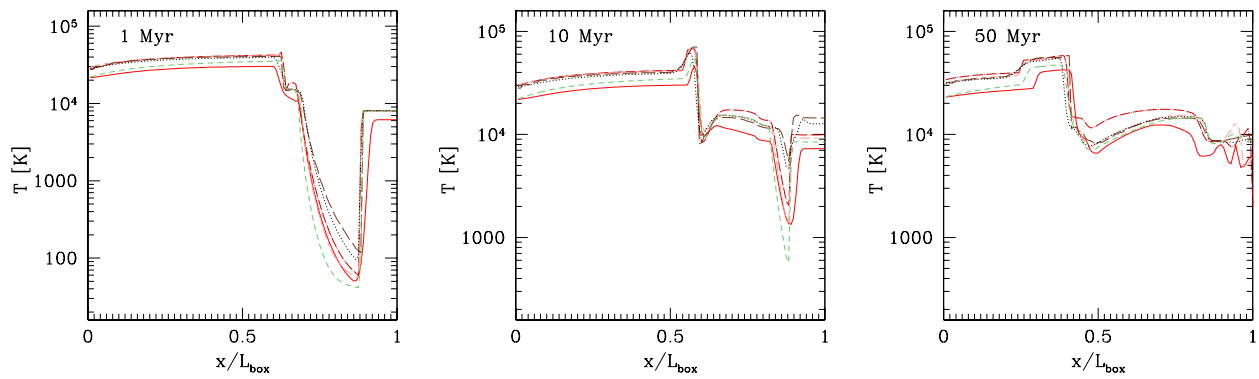

Figure 43. Test 7 (Photoevaporation of a dense clump): Line cuts of the temperature along the axis of symmetry through the centre of the clump at times $t = 1$ Myr, 10 Myr and 50 Myr (left to right).

and certain flow features like the double-peaked profile found in Test 5 disappear altogether.

For static density distributions the variations in the multi-frequency radiative transfer treatment had little effect on the I-front positions and propagation speeds since those are largely determined (apart from recombinations-related effects) by simple photon counting and balancing this number against the number of atoms entering the front. For dynamically-coupled evolution, this changes and there are significant feedback effects, with the radiative transfer effects affecting the gas dynamics and vice versa. For example, pre-heating by hard photons, or lack of it, can affect the dynamics significantly. More specifically, higher pre-heating results in shocks, e.g. ones typically leading D-type I-fronts, which are weaker and faster-propagating, and vice-versa. The internal structure of such a front and the relative spacing between the shock and the I-front can also change considerably. Shocks created by photoheating effects tend to be relatively weak, with Mach numbers of a few or less. The density compression resulting from them is strongly dependent on the pre-heating by hard photons, but generally did not exceed factors of 1.5-2. The profiles of the fluid quantities in supersonically expanding regions (e.g. the photoevaporative wind in Test 7) show good agreement among the different methods.

Significant differences were noted in the numerical diffusivity of the methods. Numerical diffusion could be due to either the radiative transfer method employed (e.g. the moment method OTVET used in HART), or the hydrodynamics (SPH in LICORICE). Higher diffusion could have notable effects on some properties of the flow (features become smoother, high contrasts are diminished), but seems to have modest effects on the overall gross features and the basic dynamics remains largely unaffected. However, care should be taken when using such methods for problems in which the sharp features might matter, e.g. enhanced molecule formation due to shocks.

The propagation of an accelerating I-front down a steep ($1/r^2$) density profile proved to be a quite difficult problem and several codes developed significant instabilities, while the rest did not. While there are a number of physical instabilities which can develop in similar situations, as we discussed in some detail, in this particular case the instabilities we observed proved to be numerical in nature. The most severe one was the carbuncle instability or odd-even decoupling, which in some cases affects low-diffusion hydrodynamic solvers (here a Roe Riemann solver). This problem can be eliminated by either adding some artificial diffusion or using a more diffusive hydrodynamic solver.

In summary, we have found a considerable level of agreement between the wide variety of radiative transfer and hydrodynamics coupled methods participating in this project. The basic flow features and their evolution are reproduced well by all the meth-

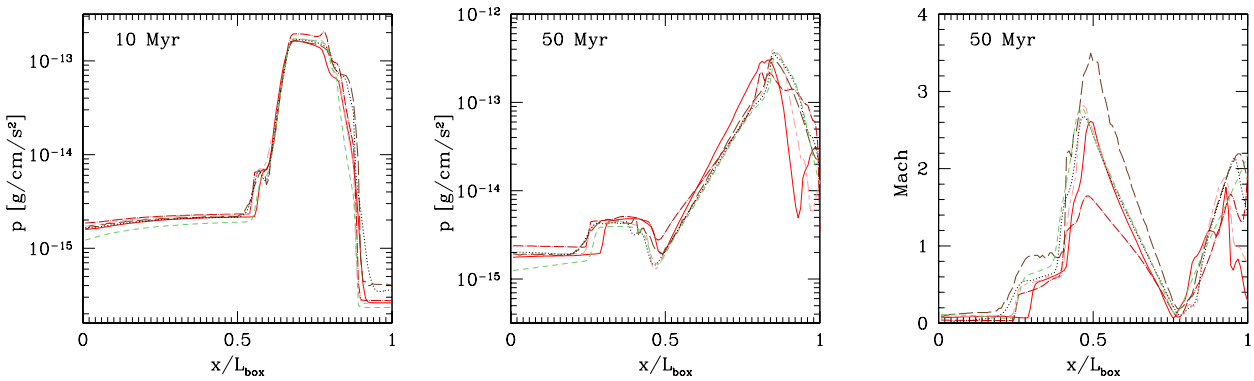

Figure 44. Test 7 (Photoevaporation of a dense clump): Line cuts of the pressure at times $t = 10$ Myr (left), and 50 Myr (centre) and of the Mach number at time $t = 50$ Myr (right) along the axis of symmetry through the centre of the clump.

ods. There are some variations whose origins we did our best to understand. The recurring differences were mostly due to the different treatment of the energy equation and the transfer of multi-frequency radiation. There were also some problems specific to certain methods which we discussed in detail. While none of the codes gave any obviously unphysical or incorrect results and all largely agreed with each other, some of the methods were clearly less suited for certain problems. No method is universally applicable to all astrophysical situations and every one of the participating codes showed some behaviour discrepant with the majority in one respect or another. Care should therefore be taken in applying any given algorithm to a new type of problem and detailed testing is always advised.

ACKNOWLEDGMENTS

This study was supported in part by Swiss National Science Foundation grant 200021-116696/1, the U.S. Department of Energy at Los Alamos National Laboratory under Contract No. DE-AC52-06NA25396, research funds from Chosun University, NSF grant AST 0708176, NASA grants NNX07AH09G and NNG04G177G, Chandra grant SAO TM8-9009X, and Swedish Research Council grant 60336701. The work with RSPH was supported in part by the *FIRST* project based on Grants-in-Aid for Specially Promoted Research by MEXT (16002003), JSPS Grant-in-Aid for Scientific Research (S) (20224002) and Inamori foundation. The Flash code was developed by the DOE-supported ASC / Alliance Center for Astrophysical Thermonuclear Flashes at the University of Chicago. MLN and DRR acknowledge partial support from NSF Grant AST-0808184.

REFERENCES

Abel T., Norman M. L., Madau P., 1999a, ApJ, 523, 66
—, 1999b, ApJ, 523, 66
Ahn K., Shapiro P. R., 2005, MNRAS, 363, 1092
—, 2007, MNRAS, 375, 881
Anninos P., Zhang Y., Abel T., Norman M. L., 1997, New Astronomy, 2, 209
Baek S., di Matteo P., Semelin B., Combes F., Revaz Y., 2009, *A.&A*, 495, 389
Bertoldi F., 1989, ApJ, 346, 735
Ciardi B., Stoehr F., White S. D. M., 2003, MNRAS, 343, 1101
Colella P., Woodward P. R., 1984, Journal of Computational Physics, 54, 174
Dale J. E., Bonnell I. A., Whitworth A. P., 2007a, MNRAS, 375, 1291
Dale J. E., Clark P. C., Bonnell I. A., 2007b, MNRAS, 377, 535
Doré O., Holder G., Alvarez M. A., Iliev I. T., Mellema G., Pen U.-L., Shapiro P. R., 2007, Phys Rev D, 76, 043002
Draine B. T., Bertoldi F., 1996, ApJ, 468, 269
Franco J., Tenorio-Tagle G., Bodenheimer P., 1990, ApJ, 349, 126
Frank A., Mellema G., 1994, *A.&A*, 289, 937
Fryxell B., Olson K., Ricker P., Timmes F. X., Zingale M., Lamb D. Q., MacNeice P., Rosner R., Truran J. W., Tufo H., 2000, ApJS, 131, 273
Galli D., Palla F., 1998a, *A.&A*, 335, 403
—, 1998b, *A.&A*, 335, 403
Garcia-Segura G., Franco J., 1996, ApJ, 469, 171
Giuliani Jr. J. L., 1979, ApJ, 233, 280
Glover S. C. O., Abel T., 2008, MNRAS, 388, 1627
Gnedin N. Y., 2000, ApJ, 535, 530
Gnedin N. Y., Tassis K., Kravtsov A. V., 2008, ArXiv e-prints
Gritschneder M., Naab T., Burkert A., Walch S., Heitsch F., Wetzstein M., 2009, MNRAS, 393, 21
Hasegawa K., Umemura M., Susa H., 2009, MNRAS, 445
Heinemann T., Dobler W., Nordlund Å., Brandenburg A., 2006, *A.&A*, 448, 731
Hindmarsh A. C., 1980, SIGNUM Newsl., 15, 10
Holder G. P., Iliev I. T., Mellema G., 2007, ApJL, 663, L1
Hosokawa T., Inutsuka S., 2005, ApJ, 623, 917
Hummer D. G., 1994, MNRAS, 268, 109
Hummer D. G., Storey P. J., 1998, MNRAS, 297, 1073
Iliev I. T., et al., 2006, MNRAS, 371, 1057
Iliev I. T., Hirashita H., Ferrara A., 2006a, MNRAS, 368, 1885
Iliev I. T., Mellema G., Pen U.-L., Bond J. R., Shapiro P. R., 2008a, MNRAS, 77
Iliev I. T., Mellema G., Pen U.-L., Merz H., Shapiro P. R., Alvarez M. A., 2006b, MNRAS, 369, 1625
Iliev I. T., Mellema G., Shapiro P. R., Pen U.-L., 2007a, MNRAS, 376, 534
Iliev I. T., Pen U.-L., Bond J. R., Mellema G., Shapiro P. R., 2007b, ApJ, 660, 933
Iliev I. T., Shapiro P. R., Mellema G., Merz H., Pen U.-L.,

2008b, in refereed proceedings of TeraGrid08, ArXiv e-prints (0806.2887)
Iliev I. T., Shapiro P. R., Raga A. C., 2005, MNRAS, 361, 405
Kahn F. D., Dyson J. E., 1965, *Ann. Rev. Astron.& Astrophys.* , 3, 47
Khokhlov A. M., 1998, JCPh, 143, 519
Knoll D. A., Keyes D. E., 2004, Journal of Computational Physics, 193, 357
Kohler K., Gnedin N. Y., Hamilton A. J. S., 2007, ApJ, 657, 15
Kravtsov A. V., 1999, PhD thesis, New Mexico State University
Kravtsov A. V., Klypin A., Hoffman Y., 2002, ApJ, 571, 563
Kravtsov A. V., Klypin A. A., Khokhlov A. M., 1997, ApJS, 111, 73
Krumholz M. R., Stone J. M., Gardiner T. A., 2007, ApJ, 671, 518
Lepp S., Shull J. M., 1983, ApJ, 270, 578
Lim A. J., Mellema G., 2003, *A.&A*, 405, 189
Mac Low M.-M., Toraskar J., Oishi J. S., Abel T., 2007, ApJ, 668, 980
Maselli A., Ciardi B., Kanekar A., 2009, MNRAS, 393, 171
Maselli A., Ferrara A., Ciardi B., 2003, MNRAS, 345, 379
Mellema G., Arthur S. J., Henney W. J., Iliev I. T., Shapiro P. R., 2006a, ApJ, 647, 397
Mellema G., Iliev I. T., Alvarez M. A., Shapiro P. R., 2006b, New Astronomy, 11, 374
Mellema G., Iliev I. T., Pen U.-L., Shapiro P. R., 2006c, MNRAS, 372, 679
Mellema G., Raga A. C., Canto J., Lundqvist P., Balick B., Steffen W., Noriega-Crespo A., 1998, *A.&A*, 331, 335
Monaghan J. J., 1992, *Ann. Rev. Astron.& Astrophys.* , 30, 543
Nakamoto T., Umemura M., Susa H., 2001, MNRAS, 321, 593
Norman M. L., Bryan G. L., Harkness R., Bordner J., Reynolds D., O'Shea B., Wagner R., 2007, ArXiv e-prints, (0705.1556)
Quirk J. J., 1994, International Journal for Numerical Methods in Fluids, 18, 555
Raga A. C., Mellema G., Arthur S. J., Binette L., Ferruit P., Steffen W., 1999, Revista Mexicana de Astronomia y Astrofisica, 35, 123
Raga A. C., Mellema G., Lundqvist P., 1997, ApJS, 109, 517
Razoumov A. O., Norman M. L., Abel T., Scott D., 2002, ApJ, 572, 695
Razoumov A. O., Norman M. L., Prochaska J. X., Wolfe A. M., 2006, ApJ, 645, 55
Razoumov A. O., Scott D., 1999, MNRAS, 309, 287
Reynolds D. R., Hayes J. C., Paschos P., Norman M. L., 2009, ArXiv e-prints (0901.1110)
Ricotti M., Gnedin N. Y., Shull J. M., 2002, ApJ, 575, 49
Rijkhorst E.-J., 2005, PhD thesis, Leiden Observatory, Leiden University, P.O. Box 9513, 2300 RA Leiden, The Netherlands
Rijkhorst E.-J., Plewa T., Dubey A., Mellema G., 2006, *A.&A*, 452, 907
Semelin B., Combes F., 2002, *A.&A*, 388, 826
—, 2005, *A.&A*, 441, 55
Shapiro P. R., Iliev I. T., Alvarez M. A., Scannapieco E., 2006, ApJ, 648, 922
Shapiro P. R., Iliev I. T., Raga A. C., 2004, MNRAS, 348, 753
Sokasian A., Abel T., Hernquist L., Springel V., 2003, MNRAS, 344, 607
Spitzer L., 1978, Physical processes in the interstellar medium. New York Wiley-Interscience, 1978
Springel V., Hernquist L., 2002, MNRAS, 333, 649
Steinmetz M., Mueller E., 1993, *A.&A*, 268, 391
Susa H., 2006, PASJ, 58, 445
—, 2007, ApJ, 659, 908
—, 2008, ApJ, 684, 226
Susa H., Kitayama T., 2000, MNRAS, 317, 175
Susa H., Umemura M., 2004, ApJ, 600, 1
—, 2006, ApJL, 645, L93
Tenorio-Tagle G., Bodenheimer P., Lin D. N. C., Noriega-Crespo A., 1986, MNRAS, 221, 635
Thacker R. J., Tittley E. R., Pearce F. R., Couchman H. M. P., Thomas P. A., 2000, MNRAS, 319, 619
Trac H., Pen U.-L., 2004, New Astronomy, 9, 443
Umemura M., 1993, ApJ, 406, 361
Vishniac E. T., 1983, ApJ, 274, 152
Whalen D., Abel T., Norman M. L., 2004, ApJ, 610, 14
Whalen D., Norman M. L., 2006, ApJS, 162, 281
—, 2008a, ApJ, 673, 664
—, 2008b, ApJ, 672, 287
Whalen D., O'Shea B. W., Smidt J., Norman M. L., 2008a, ApJ, 679, 925
Whalen D., Prochaska J. X., Heger A., Tumlinson J., 2008b, ApJ, 682, 1114
Whalen D., van Veelen B., O'Shea B. W., Norman M. L., 2008c, ApJ, 682, 49
Williams R. J. R., 1999, MNRAS, 310, 789
—, 2002, MNRAS, 331, 693